ABSTRACT

Title of Dissertation: FIELD-EFFECT FLOW CONTROL IN MICROFLUIDICS

Nathan John Sniadecki, Doctor of Philosophy, 2003

Dissertation directed by: Associate Professor Don DeVoe
Department of Mechanical Engineering

Lab-on-chip (LOC) devices have miniaturized routine laboratory processes for automated, high-throughput chemical analysis. Separations of biomolecules, including protein and DNA, have been performed with high efficiencies in LOC devices, but the need for improved fluid flow control, i.e. pumping and valves, remains a significant challenge for next-generation systems. This dissertation explores the development of novel flow-control technology in polymer microfluidic networks for the realization of inexpensive, next-generation LOC devices. In the microchannels, electroosmotic flow (EOF) is used to electro-kinetically move the fluid with a longitudinal electric field. To modulate the EOF velocity, the technique of field-effect flow control (FEFC) is employed. In FEFC, a second electric field is applied through the microchannel wall to influence the surface charge at the fluid-microchannel interface for independent control of the EOF.

Presented in this work is the first demonstration of FEFC in a polymer network. The microchannel walls were composed of Parylene C (1 - 2 μm thick), which is an inexpensive, chemical vapor deposited polymer.

In this work, FEFC modulated the EOF velocity from 240% to 60% of its original value in a microchannel that was 40 μm in height, 100 μm in width, and 2 cm long. The next research phase integrated FEFC technology into microfluidic networks with microchannels in the second and third dimensions. At the T-intersection of three microchannels, FEFC established different EOF pumping rates in the two main microchannels. The different flow rates induced pressure pumping in the third, field-free microchannel with ultra-low flow rate control (-2.0 nL/min to 2.0 nL/min). Moreover, adjusting the secondary electric fields enabled bi-directional flow control for the induced pumping in the 2D and 3D field-free microchannels. To improve the microfluidic networks, an electro-fluid flow model was developed to describe the induced pressure and FEFC phenomenon. The model closely predicted the experimentally obtained flow rates in the field-free microchannel. Additionally, the study of multiple gate electrodes along the same microchannel showed that FEFC has only a local effect over the EOF, but revealed that position and size of the electrodes influence the EOF control in the microfluidic network.

FIELD-EFFECT FLOW CONTROL IN MICROFLUIDICS

by

Nathan John Sniadecki

Dissertation submitted to the Faculty of the Graduate School of the
University of Maryland, College Park in partial fulfillment
of the requirements for the degree of
Doctor of Philosophy
2003

Advisory Committee:

Associate Professor Don DeVoe, Chair
Assistant Professor Christopher Cadou
Associate Professor Cheng S. Lee (Dean's Representative)
Professor Ugo Piomelli
Assistant Professor Elisabeth Smela

FORWARD

The dissertation work submitted to the Faculty of the Graduate School of the University of Maryland, College Park, entitled "Field-Effect Flow Control in Microfluidics" contains the following previously published work.

Chapter 3 contains the work published in the proceedings of the *Micro Total Anaylsis Systems 2001*, entitled "A Silicon Microfluidic Multiplexer Using Field Effect Flow Control." The authors of this publication are N. J. Sniadecki, P. C. Wang, C. S. Lee, and D. L. DeVoe. Mr. Sniadecki has made substantial contributions to this work:

- Post-fabrication of the microfluidic multiplexer after receiving the devices from the foundry at the University of Michigan.
- Experimentation and device characterization of flow control in the microfluidic multiplexer.

Chapter 4 and 5 contain the work published in the proceedings of the *IEEE conference on Solid-State Sensors and Actuators (Transducers '03)*, entitled "Field

Effect Flow Control in a Polymer Microchannel Network." The authors of this publication are N. J. Sniadecki, C. S. Lee, M. Beamesderfer, and D. L. DeVoe. Mr. Sniadecki has made substantial contributions to this work:

- Development of microfluidic system using polymer materials suitable for field-effect flow control.
- Design, fabrication, and testing of the all-polymer single microchannel and microfluidic network devices.
- Development of a flow visualization technique for microfluidic networks.

Chapter 7 contains the work published in the proceedings of the *Micro Total Anaylsis Systems 2003*, entitled "Field Effect Flow Control in a Polymer T-Intersection Microchannel Network." The authors of this publication are N. J. Sniadecki, R. Chang, C. S. Lee, M. Beamesderfer, and D. L. DeVoe. Mr. Sniadecki has made substantial contributions to this work:

- Design, fabrication, and experimentation of the all-polymer multigate microfluidic network.
- Development of analytical matrix-form model of field-effect flow control.

The inclusion of this work has been approved by the Dissertation Chair, Prof. Don DeVoe, and by the Direction of Graduate Studies in Mechanical Engineering, Prof. Ugo Piomelli. The work is submitted in partial fulfillment of the requirements for the degree of Doctor of Philosophy.

DEDICATION

To Carolina Lucia Elmufdi, the one who inspired me in this scholarly pursuit.

ACKNOWLEDGEMENTS

The author would like to thank Professor Don L. DeVoe, his doctoral committee chair, for his technical insights and expertise throughout this disseration work. Thanks are also extended to Professor Cheng S. Lee for his assistance and input throughout this project.

The author would like to express his appreciation to Carolina Elmufdi, who has provided the greatest support and encouragement possible throughout this time. Gratitude is given to his parents, Paul and Joan Sniadecki, who instilled in the author dedication, quality, and perseverance.

TABLE OF CONTENTS

LIST OF TABLES

LIST OF FIGURES

Chapter 1

Introduction

Lab-on-chip (LOC) devices combine bioseparation and chemical synthesis technology with secondary functional components for speed, efficiency, reduced sample consumption, and detection multiplexing for the realization of miniaturized total analysis systems [1]. Scaling laws enable chemistry performed in microdevices, which possess length scales in the range of micrometers or nanometers, to have shorter fluid transport times and lower sample diffusion than their conventional, macroscale counterparts [2, 3, 4]. For example, liquid chromatography is a method in which a liquid mobile phase mixture is separated through a column that contains a stationary phase [5]. The degree of retention of each analyte in the mobile phase with the stationary phase determines the separation time of the mixture. Thus, the speed of the system is dependent on the surface area of the stationary phase. In down-sizing to 1/10 of the original column width in a LOC device, the increased surface to volume ratios reduces all time-dependent factors to 1/100 of the original values, yielding higher efficiency [1]. In addition, improved speed and sensitivity has been demonstrated in LOC devices performing capillary electrophoresis, due to the reduced axial diffusion and Joule heating [4]. The first is a time-dependent factor and the later scales with the cross-sectional area of the microchannel. Moreover, miniaturized total analysis systems reduce

sample or reagent consumption through smaller sample volumes and connected processing steps for low sample loss [2, 3]. High-throughput performance of routine chemistry processes has been demonstrated with the integration of sample preparation and analysis on the same LOC device [6] and with high multiplicity of the same detection process [7]. Lastly, LOC device technology has been shown to have the same potential for automating sample transfers between analysis steps as high precision robotics, but without enormous amounts of equipment space, energy and cost expenses, and labor [8]. For applications in the fields of medicine, chemistry, and environmental science, LOC devices need to be "cheap, durable, and compact" [9] - the three tenets for the success of this technology.

1.1 Dissertation Objective

The main objective of this dissertation work is the design and development of an all-polymer microfluidic network with flow control components. One of the biggest challenges to the widespread development of LOC devices is controlling fluid flow on a micrometer scale [9]. The range of reported micro-pumps falls into two categories - mechanical and non-mechanical [10]. Briefly, the mechanical micro-pumps are microscale versions of the traditional macroscale pumps, which employ mechanical valves connected to a chamber where an oscillating volume flow is generated. The complications in the employment of piezoelectric [11] or peristaltic [12, 13] components for mechanical micro-pumps include limited material choices, assembly or integration restrictions, and reliability issues [14]. Non-mechanical micro-pumping techniques include, but are not limited to, magneto hydrodynamic (MHD) [15], thermal bubble generation [16], transpiration [17], surface tension [18], centrifugal systems [19], and electroosmotic flow

(EOF) [20, 21, 22, 23, 24, 25]. External pumping methods [13, 26, 27] have been reported, but the additional external equipment limits the portability of the LOC device. Several of the micro-pumping methods lend themselves readily to plastic microfluidic technology.

In LOC applications, the development of plastic materials for the realization of disposable, bioanalytical platforms is a strong research focus in both academia and the industry [28]. Popular plastics for use in microfluidics include polycarbonate [29, 30, 31], polydimethylsiloxane (PDMS) [4, 8, 32, 12, 33, 34, 35], poly(ethylene terephthalate) [29, 36], poly(methyl methacrylate) (PMMA) [37, 26], polystyrene [38], and SU-8 photoresist [39]. However, one promising plastic is Parylene C, which is a chemical vapor deposited polymer that can be used as a thin-film conformal coating. It has been used in numerous microfluidic applications for microchannel structures [40], electro-spray tips [41], micro-check valves [42], and integrated on-chip detectors [43].

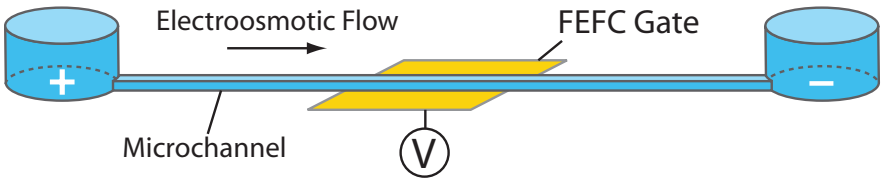

Figure 1.1: Diagram of the implementation of field-effect flow control in a microchannel with electroosmotic flow.

Electroosmotic flow is a well-suited pumping method for use in the network due to its simple implementation and non-mechanical, non-peristaltic pumping mechanism of a bulk fluid with ions. Comparing with pressure pumping, for a 1/10 reduction in microchannel width, the applied voltage requirements remain constant for EOF, while the pressure for an equivalent flow rate increases by a

factor of 100 [1, 10]. However, for complex microfluidic networks, the control of the EOF is input-limited (Section 1.3). To address this, field-effect flow control (FEFC) is proposed as an adjustable, integrated technique to locally control the EOF within a microchannel. Figure 1.1 describes the application of FEFC in a single microchannel. EOF moves the fluid by means of a longitudinal electric field from the anodic reservoir (+) to the cathodic reservoir (-). In FEFC, a second electric field is applied through the microchannel wall at the FEFC gate to modulate the surface charge at the fluid-wall interface for control over the EOF. A voltage, V, applied at the FEFC gate generates the transverse electric field so that adjustable flow control is possible. In order to achieve the goal of an all-polymer microfluidic network with FEFC gates, research contributions in the design of polymer and silicon microfluidic networks, the investigation of polymer materials suitable for FEFC, microflow characterization techniques, novel flow control of a bi-directional pressure pump in a network, and the development of an electro-fluid flow model for the microfluidic networks are presented in this dissertation.

1.2 Flow Control for High Parallel Analysis

A motivation for FEFC in a single microchannel is the realization of highly parallel systems for high-throughput analysis in drug screening. Capillary zone electrophoresis (CZE) is the most simple and widely used separation mechanism in capillary electrophoresis (Figure 1.2) [5]. The sample, containing charged species in a mixture, is introduced into the end of a capillary or microchannel

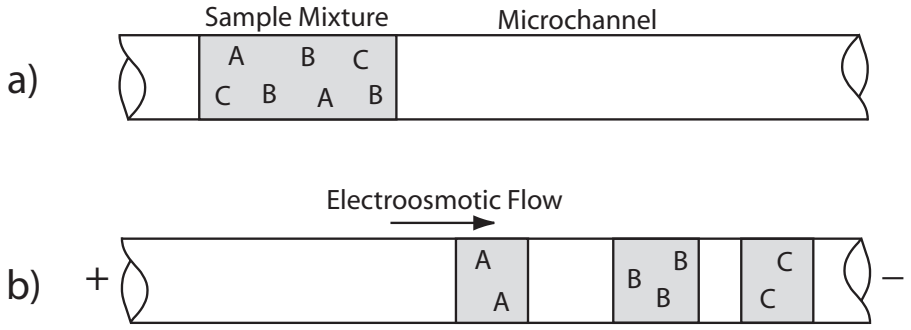

Figure 1.2: Diagram of separation mechanism in capillary zone electrophoresis. a) The sample mixture is introduced into the microchannel. b) Under an electric field, the analytes separate into distinct zones due to their mobilities.

that has been filled with conductive buffer solution[1]. Under the influence of the longitudinal electric field, the analytes migrate away from the injection end of the capillary or microchannel to the detector end, due to electrophoresis. The difference in analyte mobilities in CZE depends on the charge-to-mass ratio of the analyte ion. Electroosmotic flow is often used in this method to induce a unfavorable (reverse) flow field, resulting in longer effective column length for improved retention and resolution between the various analytes. Additionally, depending on the ion charge, EOF can act as a favorable (forward) flow field for rapid elution of the analyte zones for increased speed. Methods to optimize the mobilities and EOF include adjusting the pH, viscosity, or concentration of the buffer solution, adding surface coatings to the capillary or microchannel, or changing the longitudinal electric field (Section 2.2). Development of CZE in microfluidic platforms allows for high-throughput analysis [4]. Instead of running separations in series for each chemical interaction study, a microchannel array can

[1]A buffer solution is an electrolyte solution that resists changes in pH in the presence of acidic or alkaline analytes, which would otherwise cause drastic changes in pH [44]

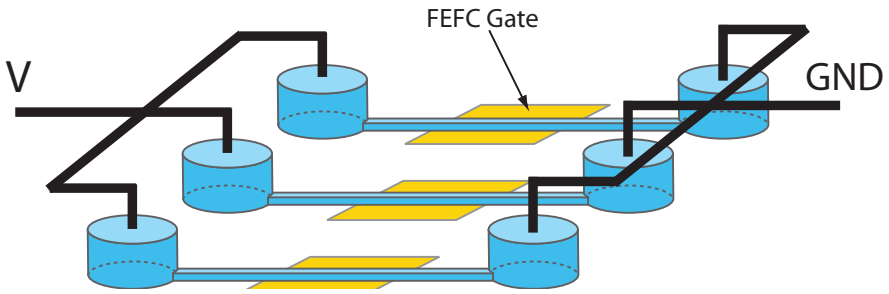

Figure 1.3: Proposed schematic of integrating FEFC into microfluidic devices for highly parallel analysis.

be ran in parallel.

For high-throughput analysis of multiple sample mixtures, each microchannel needs to be conditioned to specifically balance the mobilities of the different analytes [5]. Conditioning the microchannel array for each separation requires adjusting the buffer solution and/or longitudinal electric field in each individual microchannel. Thus, optimization required laborious device preparation or precision control of the high voltage power supply [45]. Consequently, these steps are often performed *ex post facto* and so a dynamical EOF control method is also desirable for real-time adjustments.

Instead of pre-conditioning each microchannel or employing multi-channel high voltage power supplies, FEFC is proposed as an optimization method that simplifies the analysis process and allows for dynamic adjustment of EOF (Figure 1.3). The gate electrodes underneath each microchannel allow for independent control over EOF in each microchannel. Optimization can be performed "on-the-fly" with adjustable gate voltages to improve separation resolution or shorten analysis time. Moreover, high-parallel analysis with FEFC eliminates the need for multiple/multi-channel high voltage power supplies connected to each mi-

crochannel, for one power supply can be employed and the EOF adjusted with FEFC gates. Leveraging the FEFC technique to polymer microfluidic devices allows for inexpensive, disposable microfluidic platforms for CZE.

1.3 Flow Control in Microfluidic Networks

Microfluidic networks, containing numerous interconnected microchannels, have the potential to solve the integration issues that arise in many chemistry applications, ranging from combinatorial chemistry to high-throughput screening [2, 8, 46]. The need to synthesize many chemical compounds rapidly and inexpensively in the pharmaceutical industry has spawned a new branch of chemistry known as "combinatorial chemistry." To rule out an otherwise promising drug candidate, large numbers of compounds are screened to measure if they produce a desirable or undesirable biochemical or cellular effect. The current industrial approach to these time-consuming applications is fluidic workstations that automate the handling of simple but repetitious laboratory techniques. An alternative to the space, labor, and expense demands of these high-throughput fluidic workstations is LOC devices. Through large scale integration of routine process steps on a microfluidic device, the analysis can be performed with reduced sample and reagent volumes and faster processing times [1]. The ability to automate fluid transport in a microfluidic network is one of the most promising features for LOC devices. Within a microfluidic network, the sample separations can be performed in parallel and then routed to multiple detection sites in the network. For this reason, microfluidic systems enable the integration of multiple analysis sub-components for combined separation and detection steps. Since the subcomponents are interconnected, low sample loss occurs when transferred from

one location to another on the LOC device, yielding improved chemical detection and analysis.

EOF pumping can meet the demands of controlling the flow in microfluidic networks better than pressure-driven flow [46]. The advantage of EOF is direct control, fast response, and simple implementation. Pressure-driven flow requires large pressure gradients between the fluid reservoirs in order to pump fluid through narrow microchannels [47]. However, a problematic area for EOF pumping is the interaction of multiple longitudinal electric fields in microfluidic networks. An example of a M×N microfluidic network is shown in Figure 1.4. Toggling individual microchannel flow velocities is critical for the mixing of two or more flows, for spliting flows, and for synchronizing separation times. In microfluidic networks, the EOF electric fields interact with each other at the intersections of the microchannels because the conductive buffer fluid connects them electrically. In Figure 1.4, controlling the EOF in one microchannel requires adjusting the M∗N voltages at each reservoir[2], which can lead to undesirable flow velocities in the other microchannels. For complex microfluidic networks, the control becomes input-limited as shown in Figure 1.4. The ten voltage inputs at the fluid reservoirs are insufficient to independently control the flow in all seventeen microchannels.

A static method to circumvent the problem and achieve quasi-independent flow control has been demonstrated with surface coatings on glass [21, 22] and plastic substrates [23, 48, 49]. The surface coatings change the local EOF in each microchannel. However, for adaptable microfluidic networks, which can

[2]Granted, all but two voltages could be set to a floating potential, for EOF in a single microchannel, but this method does not allow for multiplexing of the flow.

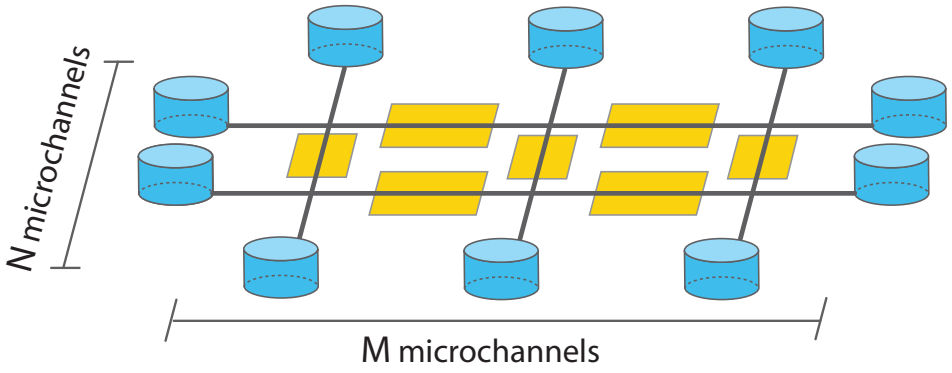

Figure 1.4: Proposed implimentation of FEFC in an M×N microfluidic network.

adjust during the run to different analyte mobilities, dynamic changes to the EOF are necessary. Dynamic flow control has been demonstrated with synchronized reservoir pressure and voltage potentials [46], but external pressure control at the reservoirs limits the portability of the microdevice and increases the equipment costs and energy requirements. In contrast, the use of FEFC in microfluidic networks enables adjustable changes to the local EOF, without the permanent changes of surface coatings. As shown in Figure 1.4, FEFC gates are placed in each microchannel to locally control the EOF. The implementation of FEFC has the ability to compensate for electric field interactions at the intersection of the microchannels.

1.4 Dissertation Organization and Contributions

In this dissertation, microfluidic networks using FEFC are presented. The all-polymer networks are fabricated using chemical vapor deposition of Parylene C and micromolding of PDMS for the microchannel wall. The fabrication technology is compatible with plastic substrates for cost reduction. Use of FEFC in microfluidic networks exhibited dynamic control of the EOF and induced pres-

sure pumping for 2D and 3D microfluidic networks. The development of an electro-fluid model that closely predicts the interaction of multiple FEFC gates in a network is also presented. The model and microfluidic network were used in tandem to investigate various gate conditions, gate designs, and microchannel dimensions for future FEFC microfluidic networks.

This dissertation consists of eight chapters. Chapter 1 contains a brief introduction to the field of high-throughput LOC devices, microfluidic networks, and an introduction to this dissertation work. The second chapter develops the physics of the electric double layer, electroosmosis, and field-effect flow control with a review of previous FEFC work in capillary and microfluidic systems. Chapter 3 presents a novel silicon microfluidic multiplexer that leveraged off of previous FEFC demonstration in silicon-based materials. In Chapter 4, the investigation of suitable polymer materials for FEFC and the development of a single polymer microchannel with FEFC is presented. In Chapter 5, the polymer FEFC technology is "scaled-up" to microfluidic networks that use differential EOF pumping to induce pressure pumping in the second or third dimension microchannels. The innovations in fabrication and flow characterization, which were required for the development of the microfluidic networks, are also discussed. Chapter 6 introduces the electro-fluid models that predict the operation of the flow control in the microfluidic networks. The model is further developed in Chapter 7, where the investigation into the interaction of multiple gates in a microfluidic network is presented. Finally, concluding remarks and suggestions for future work are presented in Chapter 8.

Chapter 2

Background

When two phases are placed in contact, in general, a potential difference develops between them. In the case of microfluidics, often one of the phases is a polar liquid, such as water, and the other phase is the solid microchannel wall that bounds the liquid. If there are ions or excess electrons in one or both phases, then the electric charges will tend to distribute themselves in a non-uniform way at the liquid-wall interface. Accordingly, a separation of electric charge marks the interface between the two adjoining phases and is referred to as the *electric double layer*.

Fluid pumping is achieved when the non-conductive solid phase remains stationary and the liquid phase moves in response to an applied electric field. This phenomenon is referred to as *electroosmotic flow*. The counter-ions in the liquid phase, which balance the surface charge at the microchannel wall, move under the force of the applied field dragging the bulk liquid molecules with them. The *zeta potential* is a measure of the ion concentration at the fluid-wall interface and determines the electroosmotic pumping rate of the bulk fluid.

Field-effect flow control is the modulation of the electroosmotic flow by means of a transverse electric field through the microchannel wall. At the fluid-wall interface, the balancing charges in the fluid phase redistribute themselves in accor-

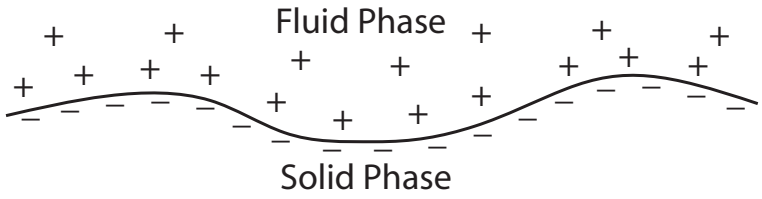

Figure 2.1: Diagram of charge distribution between solid and liquid phases in contact.

dance to the transverse field to increase or decrease the zeta potential. Thus, the transverse electric field determines the magnitude and sign of the zeta potential due to the change in the ion concentration at the fluid-wall interface. Therefore, the flow rate and direction of electroosmosis changes due to the transverse electric field, independently of the longitudinal electric field that generates the electroosmotic flow.

2.1 Separation of Charge

At the surface of any single phase, there is a separation distance on the order of one or more molecular diameters of positive and negative charge carriers, either electrons or ions. When two phases are placed in contact, the charged carriers in each phase are attracted to the opposite charge carriers in the other phase. Except under special conditions, a separation of electrical charges marks the contact region between two phases. As shown in Figure 2.1, near to or on the surface of the microchannel wall, there is an excess of charge of one sign and the balancing charge is distributed in some way throughout the adjoining surface of the fluid. Moreover, the resulting electric field from the separation of charge may also cause polarization effects in neighboring molecules.

All of these effects tend to produce a difference in the electrical potential

between the interior of the two phases, called the "inner" or Galvanic potential difference, $\Delta\phi$ [50]. The potential difference is fundamentally impossible to measure explicitly, except when the two phases are chemically identical. The inner potential difference measures the total work done from moving a hypothetical test charge from the interior of one phase into the interior of the second phase. To measure the inner potential experimentally, the smallest and least disruptive test charge would be an electron, but this particle has a significant effect on the electrical structure of its surroundings. The inner potential is impossible to measure, but its effect on the surrounding phase can be observed, for example in the case of the electric double layer.

The separation of charge that occurs at the fluid-wall interface between two phases is called an electrical double layer because it consists of two regions of opposite charge. The simplest model of such a system is where both layers of charge are fixed in parallel planes to form a molecular condenser or parallel plate capacitor. For a metal surface and most solid insulators, the charges are assumed to be located in a plane. In a liquid phase, a plane of charge is unlikely to exist because the electrical forces on the counter-ions compete with the thermal diffusive forces. Thus, one layer of charge is spread out uniformly over a plane surface of the wall while the charges in the electrolyte solution will be distributed with non-uniformity. The wall surface will have an inherent surface potential, ψ_0, while the balancing ions are regarded as point charges immersed in a continuous dielectric medium.

The electric double layer is developed in Appendix A. The thickness of the electrical double layer is customarily defined as the distance $1/\kappa$ from the fluid-wall interface, which is typically on the order of nanometers in thickness. As

discussed for the Debye-Hückle parameter, κ, (equation A.11 on page 161), the distance $1/\kappa$ depends on the ion concentration of the buffer solution[1]. Within the electric double layer, the counter-ion charge distribution decays exponentially (equation A.17) from the wall potential, ψ_0, to the potenial in the bulk fluid, which is defined to be zero due to the equal concentration of co-ions and counter-ions ($\psi(x \to \infty) = 0$). Since the potential in the electric double layer reaches a value of 2% of ψ_0 at a distance of $3/\kappa$, the local concentrations of co-ion and counter-ions are unequal in a region closely confined to the fluid-wall interface.

2.2 Electroosmotic Flow (EOF)

Electroosmosis is the motion of bulk fluid with respect to a stationary, charged solid surface. The application of an electric field, E_z, parallel to the microchannel wall produces electroosmotic flow in an electrolyte solution. The direction of the electroosmotic velocity, u_{eo}, is parallel to the wall and the magnitude, which von Smoluchowski first expressed in its present form [51], is:

$$u_{eo} = -\frac{\epsilon\zeta}{\eta} E_z \tag{2.1}$$

where ϵ is the fluid permittivity and η is the viscosity. The zeta potential, ζ, is the average potential at the plane of shear, which is the no-slip boundary at the microchannel wall, due to strongly adsorbed counter-ions. The zeta potential is determined from the wall surface potential, ψ_0 (an exponential relationship in the Debye-Hückle approximation, section A.17). Under the influence of E_z, the counter-ions not adsorbed to the fluid-wall interface, but of high concentration

[1] κ depends on the ionic concentration so for 1 mM solution at 25 °C, the double layer thickness is 9.65 nm.

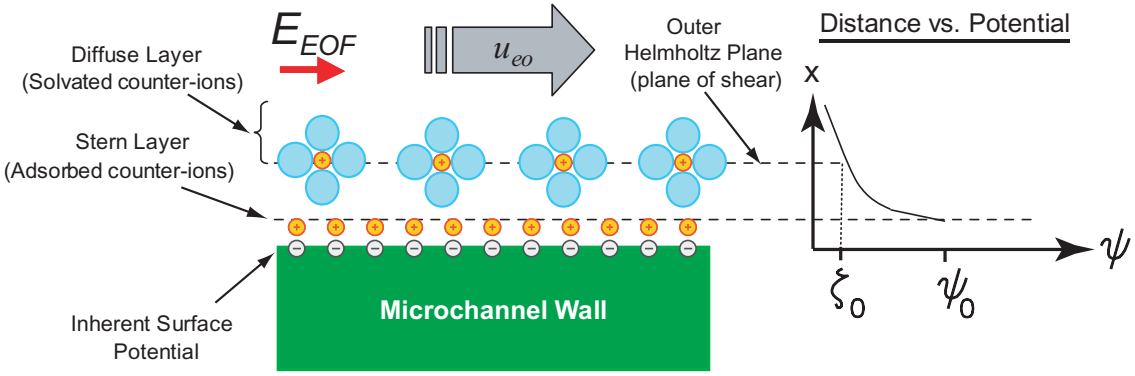

Figure 2.2: Schematic of the electric double layer. The co-ions in the diffuse layer are not shown.

in the electric double layer, generate a body force on the liquid phase due to ion drag. The resulting sheath flow pumps the bulk fluid in the direction of E_z, depending on the valency and concentration of the ions, which the zeta potential embodies.

A schematic representation of the ion distribution at the wall surface is shown in Figure 2.2. The surface functional groups of the wall material determine the inherent surface potential, ψ_0. It is the electrochemical reaction at the fluid-solid interface, due to the difference in Galvanic potentials between the phase, that generates these excess ions. The surface functional groups define the negative surface charge, ψ_0, at the microchannel wall. For fused silica capillaries, the surface charge is due to the dissociation of the free hydroxyl groups of the silica surface from the silanol groups (SiO^-) [52]:

$$SiOH \longleftrightarrow SiO^- + H^+$$

The silica-solution interface can be treated as a single-site model. As a result, the dissociation of the silanol groups is the sole ionization reaction of the surface silanol groups, for a resulting negative surface charge (Figure 2.2). Since ψ_0

determines the magnitude of the zeta potential, modification of the wall chemistry controls the electroosmotic flow. Common modification to the surface charge include buffer additives [53], ionic strength [54], buffer pH [55], organic solvents [56], or wall coatings [57, 58]. To compensate for the negative wall charge, positive counter-ions are adsorbed to the wall interface forming the immobilized Stern layer or inner Helmholtz plane. The potential decays exponentially between the Stern layer (Section A.2), where the ions are tightly bound due to electrical forces, and the diffuse layer, where the electrical forces compete with diffusive forces. The outer Helmholtz plane marks the plane of solvated counter-ions, which are loosely bound. The zeta potential lies at the outer Helmholtz plane, or plane of shear, where the counter-ions are free to move under the force of E_z. The zeta potential is shown in Figure 2.2 as ζ_0 (c.f. Figure A.1 on page 162). The neutral molecules of the liquid phase, for example water molecules in an aqueous buffer solution, solvate the counter-ions at the diffuse layer by van der Waal forces. The solute counter-ions drag the neutral molecules in the direction of the electric field to achieve bulk flow. On the contrary, the flow is in the opposite direction if the counter-ions are opposite in charge due to a positive wall potential.

From a fluid mechanics standpoint, the outer Helmholtz plane marks the plane of shear. The adsorbed counter-ions are strongly bound to the surface of the microchannel due to the high electrical forces. The nature of the adsorbed counter-ions is of ongoing research debate, but suffice to say, they mark the no-slip boundary condition. The flow in the diffuse layer is mainly due to the electrokinetic forces from the longitudinal electric field, E_z, and viscous forces on the counter-ions. The resultant velocity field exhibits a gradient over a distance of tens of nanometers from the microchannel wall until it reaches the plane of

slip with a maximum velocity given by the Smoluchowski equation (equation 2.1). The flow outside the electric double layer exhibits a plug-like flow for uniform zeta potentials and the absence of pressure gradients.

The basic equation describing the EOF outside of the electrical double layer of an incompressible Newtonian fluid is derived from the classic Navier-Stokes equation [59, 60]:

$$\rho \frac{D\vec{u}}{Dt} = F - \nabla p + \eta \nabla^2 \vec{u} \tag{2.2}$$

where ρ is fluid density, $\vec{u}$ is the velocity field, p is the pressure, ρ is the fluid density, F is the body force, and η is the viscosity. Assuming that gravity forces are negligible, the body force in EOF is purely an electrokinetic body force due to the electrical force exerted on the ions [50, 61]:

$$F = \rho_e \vec{E} \tag{2.3}$$

where ρ_e is the spatial charge density of the co-ions and counter-ions (Equation A.1) and $\vec{E}$ is the electric field in the microchannel.

Since typical EOF in microfluidic applications have Reynolds number[2] (Re) smaller than unity, the flow is a balance of the electrokinetic body force, pressure gradients, and viscous forces. To illustrate the balance of forces at low Re, equation 2.2 can be non-dimensionalized with substitution of the following dimensionless parameters:

$$x_i^* = \frac{x_i}{H}$$

$$\vec{u^*} = \frac{\vec{u}}{u_{eo}}$$

$$t^* = \frac{t u_{eo}}{H}$$

[2]Non-dimensional ratio of fluid inertial forces to viscous forces: $Re = \rho u_{eo} H / \eta$

$$p^* = \frac{p}{\eta u_{eo}/H}$$
$$\nabla^* = H\nabla$$
$$\vec{E^*} = \frac{\vec{E}}{E_z}$$
$$\rho_e^* = \frac{\rho_e H}{E_z \epsilon}$$

where H is the characteristic height of the microchannel. Substituting the dimensionless parameters in equation 2.2 produces:

$$\left(\frac{\rho u_{eo}^2}{H}\right)\frac{D\vec{u^*}}{Dt^*} = \frac{E_z^2\epsilon}{H}\rho_e^*\vec{E^*} - \frac{\eta u_{eo}}{H^2}\nabla^* p^* + \frac{\eta u_{eo}}{H^2}\left(\nabla^*\right)^2\vec{u^*}$$

$$\left(\frac{\rho u_{eo} H}{\eta}\right)\frac{D\vec{u^*}}{Dt^*} = \frac{E_z^2\epsilon H}{\eta u_{eo}}\rho_e^*\vec{E^*} - \nabla^* p^* + \left(\nabla^*\right)^2\vec{u^*}$$

For low Reynolds numbers (Re $\ll 1$), the left hand side is zero

$$\mathrm{Re}\frac{D\vec{u^*}}{Dt^*} = \frac{E_z^2\epsilon H}{\eta u_{eo}}\rho_e^*\vec{E^*} - \nabla^* p^* + \left(\nabla^*\right)^2\vec{u^*}$$

$$0 = \frac{E_z^2\epsilon}{\eta u_{eo}/H}\rho_e^*\vec{E^*} - \nabla^* p^* + \left(\nabla^*\right)^2\vec{u^*} \tag{2.4}$$

Thus, for electrosmosis, the flow is a balance of the electrokinetic forces, pressure gradients, and viscous forces. The coefficient of the electrokinetic force is the ratio of electrical energy density to viscous energy density (J/m^3).

In typical electroosmotic pumping applications, the pressure gradients are eliminated ($\nabla p = 0$) and the applied electric field is parallel to the microchannel wall ($\vec{E} = E_z$), so that equation 2.4, in dimensional form, is

$$0 = \rho_e E_z + \eta\nabla^2\vec{u} \tag{2.5}$$

The charge distribution, ρ_e, at the electric double layer is governed by the Poisson's equation (equation A.1):

$$\nabla^2\psi = -\frac{\rho_e}{\epsilon}$$

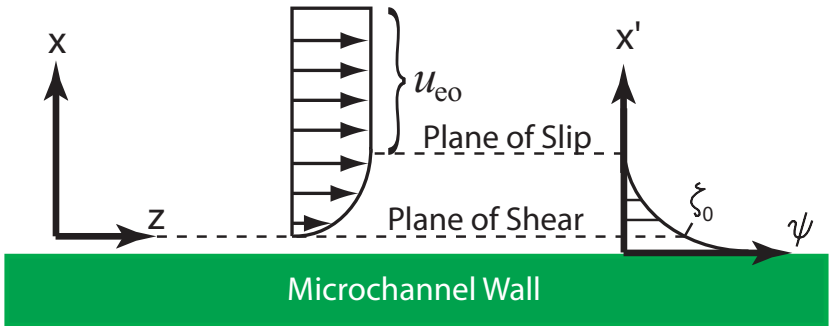

Figure 2.3: Schematic of electroosmotic flow. The origin (z vs. x) for the Navier-Stokes equation lies at the plane of shear, at a distance one or a few molecular diameters from the microchannel wall, where the no-slip condition applies. The origin (ψ vs. x') for the potential distribution lies at the microchannel wall.

where ψ is the inherent potential distribution from the electric double layer and assumed to be without tangential gradients. Typically, the longitudinal electric field is on the order of hundreds of volts per centimeter and the inherent potential field at the microchannel wall is on the order of tens of thousands of volts per centimeter ($\zeta_0/(3/\kappa)$). Since the effect of the inherent potential field is negligible outside the electric double layer ($\psi(x \rightarrow \infty) = 0$ shown in Figure A.1 on page 162), the longitudinal electric field is without gradients normal to the microchannel wall (x-direction). Likewise, the effect of the longitudinal electric field on the inherent potential distribution is typically negligible due to its low field strength and the high diffusivities of the counter-ions.

Substituting for ρ_e into equation 2.5 yields

$$\eta \nabla^2 \vec{u} = \epsilon \nabla^2 \psi E_z \tag{2.6}$$

As seen in equation 2.6 for electroosmosis, the flow results from the competition of electrokinetic and viscous forces. A schematic of the flow in the electric double

layer is shown in Figure 2.3. For flow parallel to the microchannel wall in the z-direction, denoted as w, equation 2.6 becomes

$$\eta\left(\frac{\partial^2 w}{\partial x^2}+\frac{\partial^2 w}{\partial z^2}\right)=\epsilon\left(\frac{\partial^2 \psi}{\partial x^2}+\frac{\partial^2 \psi}{\partial z^2}\right)E_z$$

The first condition is that the flow is divergence-free ($\nabla\cdot\vec{u}=0$). Since there is no flow in the normal direction ($u=0$), the flow along the microchannel is without a tangential gradient ($\partial w/\partial z=0$). Second, due to the negligible interaction of the longitudinal electric field, the inherent potential distribution, ψ, is assumed to be without a tangential gradient ($\partial\psi/\partial z=0$). With these two conditions, the Navier-Stokes equation reduces to

$$\eta\frac{\partial^2 w}{\partial x^2}=\epsilon\frac{\partial^2 \psi}{\partial x^2}E_z \tag{2.7}$$

To find the expression for the flow, equation 2.7 can be integrated twice in x:

$$w=A+Bx+\frac{\eta\psi}{\eta}E_z$$

where A and B are the constants of integration. Applying the boundary conditions at the Stern layer ($w=0$ and $\psi=\zeta_0$ at x $=0$) and in the bulk fluid ($\partial w/\partial x=0$ and $\partial\psi/\partial x=0$ at $x=\infty$) yields

$$w=-\frac{\epsilon}{\eta}E_z\left(\zeta_0-\psi\right) \tag{2.8}$$

Assuming that both η and ϵ keep their bulk values everywhere in the microchannel, then equation 2.8 states that the velocity is proportional to both the zeta potential, the applied EOF electric field, and the inherent potential distribution in the microchannel. The adopted sign convention is that when ζ_0 is negative, the flow is towards the cathode.

Applying the Debye-Hückle approximation (Section A.2 on page 163), the inherent potential distribution is (equation A.17):

$$\psi = \psi_0 \exp(-\kappa x')$$

The origin for the Navier-Stokes equation is at the plane of shear ($x = 0$), but the origin for the inherent potential distribution is at the microchannel wall ($x' = 0$). Without loss to the description of the potential distribution, equation A.17 can be rewritten in terms of the Navier-Stokes coordinates as

$$\psi = \zeta_0 \exp(-\kappa x) \tag{2.9}$$

Substituting equation 2.9 into equation 2.8 produces

$$w = -\frac{\epsilon \zeta_0}{\eta} E_z \left(1 - \exp(-\kappa x)\right) \tag{2.10}$$

The velocity profiles from equation 2.10 are shown in Figure 2.4 for varying electric double layer thicknesses and zeta potentials. In both plots, the viscosity and permittivity are the values of water[3] and the longitudinal electric field is 100 V/cm. For plot (a), the velocity is uniform at a distance far outside the electric double layer that is proportional to the value of $1/\kappa$. The values for $1/\kappa$ correspond to the lowest buffer solution concentrations (1 mM, 0.15 mM, 30 μM, and 10 μM respectively) that are typical in microfluidics. For plot (b), the velocity profile is uniform at the same distance for each value of ζ_0, but the maximum velocity varies according to the zeta potential.

For large κ values in Figure 2.4, the exponential term in equation 2.10 is negligible at values of $x \geq 5/\kappa$. For the distance at which the velocity profile becomes

[3]At 25°C, $\eta = 0.891 \times 10^{-3}$ kg/m·s and $\epsilon = 79 * 8.854 \times 10^{-12}$ F/m

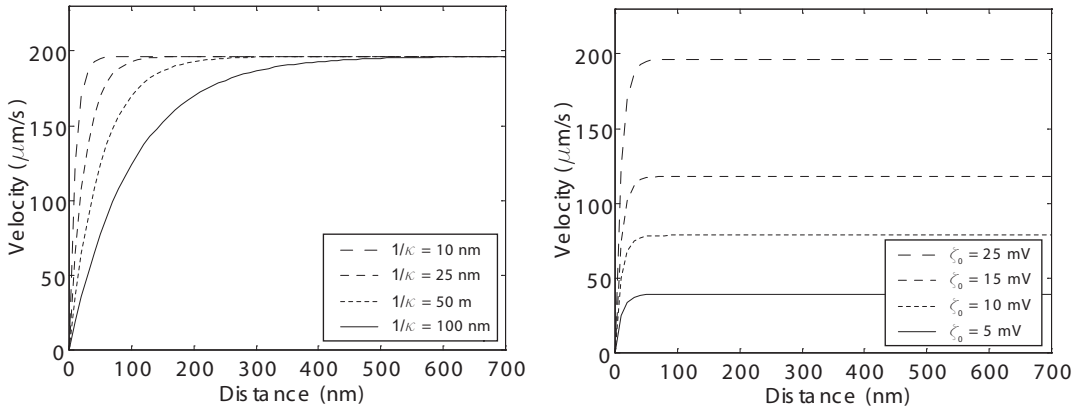

(a) (b)

Figure 2.4: Velocity profiles from equation 2.10 for varying (a) electric double layer thicknesses ($1/\kappa$) and (b) zeta potentials (ζ_0).

uniform, equation 2.10 is equivalent to the Smoluchowski equation (equation 2.1):

$$w = -\frac{\epsilon\zeta_0}{\eta}E_z$$

Specifically, the distance at which the velocity is equal to that from the Smoluchowski equation is denoted as the plane of slip. The plane of slip is equivalent to the boundary layer in fluid dynamics, because the effect of viscosity is important inside the plane. Outside the boundary layer, the flow can be considered as the flow of an inviscid fluid. Hence, the flow is irrotational and without vorticity. From the results shown in Figure 2.4, the boundary layer thickness, δ_0, depends primarily on the electric double layer thickness. To express the boundary layer thickenss in terms of $1/\kappa$, the plane of slip is defined as the distance at which the velocity reaches 99% of the maxium velocity:

$$\frac{w}{u_{eo}} = \left.\frac{\frac{\epsilon\zeta_0}{\eta}E_z(1-\exp(-\kappa x))}{\frac{\epsilon\zeta_0}{\eta}E_z}\right|_{x=\delta_0}$$

$$\frac{w}{u_{eo}} = 1-\exp(-\kappa\delta_0)$$

$$0.99 = 1 - \exp(-\kappa\delta_0)$$

$$0.01 = \exp(-\kappa\delta_0)$$

$$-4.6 \approx -\kappa\delta_0$$

$$\delta_0 \approx 4.6/\kappa \tag{2.11}$$

For the range of electric double layer thicknesses in Figure 2.4, the calculated value of the boundary layer thickness in equation 2.11 is equivalent to the distance at which the velocity becomes uniform. Thus, the plane of slip marks the distance from the plane of shear where the flow velocity, w, rises from a value of zero at the wall to a maximum value, u_{eo}.

2.3 Field-Effect Flow Control

A method for dynamic flow control of electroosmosis is the modulation of the zeta potential by means of a transverse electric field, E_{FEFC}, through the microchannel wall. In its first incarnation, electrodes or conductive sheaths surrounded fused silica capillaries to generate the transverse electric field through the capillary wall [52, 62, 63, 64, 65, 66, 67, 68, 69, 70, 71, 72]. The technique of field-effect flow control (FEFC) solved a major problem for capillary zone electrophoresis (CZE) with direct control over electroosmosis. With FEFC, researchers were able to control the concentration or elution time for improved efficiency and resolution of peptide and protein separations. With the advent of microfabrication techniques for microfluidics, several researchers employed FEFC in microfluidic devices for chemical separations. Similar to FEFC in capillaries, gate electrodes are embedded under the walls of microchannels to generate the transverse electric field [24, 25, 73, 74, 75].

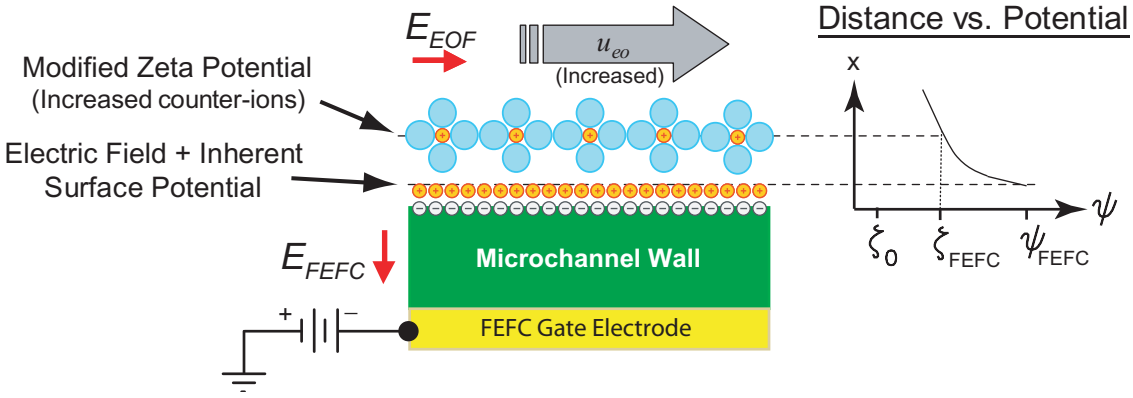

Figure 2.5: Field-effect flow control in the electric double layer.

In capillary and microfluidic devices, the transverse electric field from the gate electrode directly affects the zeta potential. Figure 2.5 shows the change in the surface charge, ψ_{FEFC}, due to the negative electric field. The induced surface charges are due to the capacitive effect of the gate electrode. Compared to the unmodified EOF in Figure 2.2 ($\psi_{FEFC} > \psi_0$), a larger concentration of counter-ions reside in both the Stern layer and the diffuse layer because of ψ_{FEFC}. Increased counter-ion concentration affects the zeta potential magnitude, ζ_{FEFC}, for increased EOF pumping from the Smoluchowski equation (equation 2.1). In the case of a positive transverse electric field, the induced surface charge is lower than the inherent surface charge ($\psi_{FEFC} < \psi_0$) and fewer counter-ions reside in the electric double layer for reduced EOF. If the electric field is sufficiently large to drive away the counter-ions, then it can establish negligible electroosmosis due to a extremely small zeta potential. Furthermore, a large positive electric field can dominate the electric double layer concentration more than the surface charge to yield reverse EOF.

To understand the effect of FEFC on EOF, previous researchers have proposed a double capacitor model that considers the change in the zeta potential to be

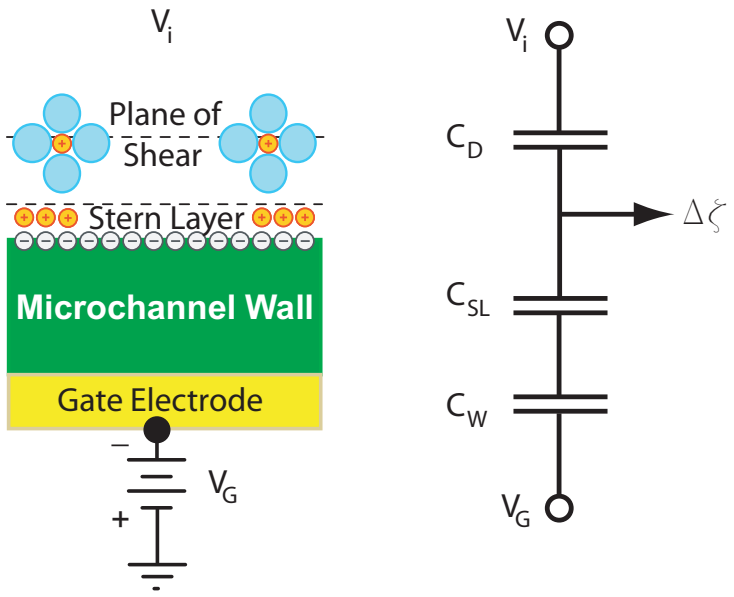

Figure 2.6: Equivalent capacitor circuit for double capacitor model.

electrostatic in nature [64, 65, 66, 69]. As seen in Figure 2.6, the capacitance of the diffuse layer, C_D, the capacitance of the Stern Layer, C_{SL}, and the capacitance of the microchannel wall, C_W are in series. The change in the zeta potential, $\Delta\zeta$, can be determined from the equivalent capacitor circuit where

$$\zeta_{FEFC} = \zeta_0 + \Delta\zeta \tag{2.12}$$

As in a voltage divider, $\Delta\zeta$ measures from the voltage drop across the diffuse layer capacitor due to an applied gate voltage, V_G:

$$\Delta\zeta = I/C_D \tag{2.13}$$

The theoretical current, I, through the circuit is

$$I = (V_G - V_i)/Z_T \tag{2.14}$$

where V_i is the voltage potential above the gate region due to the longitudinal electric field for EOF and Z_T is the total impedance of the three capacitors. Since

the thickness of the Stern layer and diffuse layer are on the order of nanometers and the microchannel wall thickness is on the order of micrometers, the total impedance can be approximated as

$$Z_T = (C_D)^{-1} + (C_{SL})^{-1} + (C_W)^{-1}$$

$$Z_T \approx (C_W)^{-1} \tag{2.15}$$

Substituting equations 2.12 to 2.14 into 2.15, the change in the zeta potential for a given gate voltage is

$$\zeta_{FEFC} = \zeta_0 + \frac{C_W}{C_D}(V_G - V_i) \tag{2.16}$$

From an engineering perspective, the degree of control over the zeta potential stems from the ratio of the wall and diffuse layer capacitance and the magnitude and direction of the transverse electric field.

2.3.1 Design Factors for FEFC

Increasing the double capacitor ratio (C_W/C_D) is the goal for high zeta potential control at low transverse electric fields. As developed in Appendix A, the capacitance of the diffuse layer is (equation A.21)

$$C_d = 2.285 z c^{1/2} \cosh(19.4 z \psi_0)$$

Changes to the buffer solution or wall surface chemistry can decrease the diffuse layer capacitance for improved FEFC performance. Reducing the buffer ion concentration, c, shrinks the double layer thickness for increased C_D [64, 66]. Lowering the buffer pH drives the dissociation reaction of surface functional groups toward fewer single sites and decreased ψ_0 [52]. Similarly, surface coatings can be employed to deactivate the surface functional groups [69].

From a microfabrication perspective, the thickness of the microchannel wall above the gate electrode, d, can be reduced to increase the wall capacitance:

$$C_W = \frac{\epsilon}{d} \tag{2.17}$$

in F/m^2 [62]. Furthermore, the wall material with a high dielectric constant yields an increased wall capacitance for improved FEFC. In the literature, controlling these factors has enabled improved FEFC and validated the double capacitor model. However, recent criticism of the double capacitor model is its inadequate encompassing of all experimental results reported in the literature [72, 76]. Given the wide variety of FEFC implementations (concentric capillaries, conductive sheathed capillaries, gate electrodes in microchannels, etc.) the double capacitor model expresses the key factors in FEFC.

2.3.2 Capillary FEFC

The first application of FEFC was in capillaries, before widespread use of LOC devices. The pioneers in the FEFC capillary research were Lee *et al.* and Hayes *et al.*

Lee *et al.*

The first demonstration of FEFC used concentric capillaries, where a high electric field was generated through the wall of the inner capillary from the unequal EOF electric fields between the two capillaries [62]. The diagram of the capillary set-up in Figure 2.7 shows that the outer capillary generates the gate voltage, V_G, with reference to the EOF voltage, V_i, in the inner capillary to produce the transverse electric field. The EOF was measured by current monitoring [77] as a low concentration buffer solution replaced a higher concentration

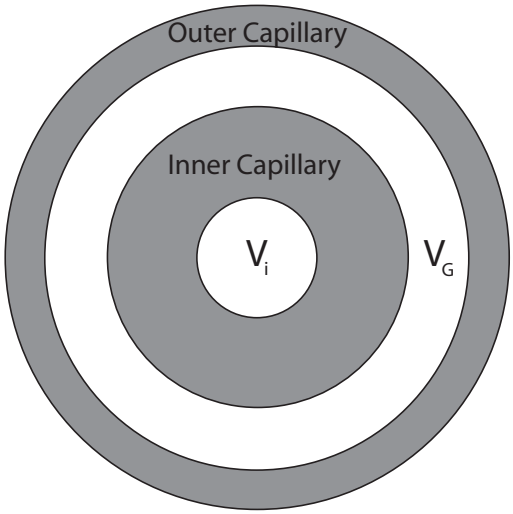

Figure 2.7: Schematic of the concentric capillaries in the first demonstration of FEFC.

buffer solution. With this set-up, direct EOF control was reported with the first demonstration of reversed EOF.

Lee *et al.* first proposed the double capacitor model and explored the factors that contribute to FEFC. Studying the effect of changes in ion concentration, buffer pH, and capillary wall thickness validated the double capacitor model [64, 65]. The separation of peptide and proteins with FEFC displayed the utililty of direct EOF control in capillary zone electrophoresis [67]. Lastly, they explored the effect of adsorbed ions and organic coatings on the shielding of the inherent surface charge in FEFC [69].

Hayes *et al.*

Instead of concentric capillaries, Hayes *el al.* demonstrated FEFC within a single capillary and a conductive sheath coating [66]. This method led to the dis-

covery that large coverage areas over the length of the capillary are not required for adequate FEFC [68]. The apparatus used for these experiments had similar EOF control for 4% and 60% coverage of the capillary length. The authors attributed the control to the "spreading" of the zeta potential. They assumed that outside the covered capillary region, the zeta potential followed a linear gradient from the ζ_{FEFC} to ζ_0, due to surface conductance in the diffuse layer. The proposed flow equation matches the experimental results closer than the weighted average relationship [54, 78] that was previously proposed for dissimilar zeta potentials in a capillary. Additionally, they demonstrated that FEFC could be extended to higher pH buffer solution (pH $\geq$ 5) through the use of a surface coating for reduced inherent zeta potentials, ζ_0, and lower diffuse layer capacitance, C_D [71].

2.3.3 Microchannel FEFC

For LOC devices, FEFC offers several advantages: ease of implementation, optimization for separation efficiency and resolution, and high degree of automation. These devices have been fabricated on silicon and glass substrates with conventional microfabrication methods. In all designs, the use of inorganic materials with high dielectric strengths prevented the onset of electrical breakdown due to the high transverse electric fields.

Polson *et al.*

The first demonstration of FEFC was performed in a microfabricated glass substrate [25]. The FEFC gate electrodes were located parallel to the main microchannel and separated by 50 μm of glass. The applied gate voltage of 120 V

from the connected power supply was smaller than the kilovolts typically applied in capillary FEFC work. Instead of current monitoring, the speed of fluorescein dye as it flowed past a UV detector was used to measure the electroosmotic velocity. The glass microdevice yielded 40 times more control over EOF than previously reported capillary FEFC results. The improved control is attributed to the thin microchannel wall thickness that is possible with microfabrication.

Schasfoort *et al.*

The second FEFC LOC device reported was a silicon-glass microdevice that used silicon nitride as the microchannel wall [24]. A silicon wafer was bulk etched in KOH to form cavities that served as a mold for the microchannel walls. Chemical vapor deposition was employed to grow silicon nitride to a 390 nm thickness on the walls of the mold. This deposition step formed the three walls of the microchannel. Anodic bonding of a glass substrate to the silicon nitride formed the bottom wall of the microchannel, where its transparency allowed for flow visualization. The backside of the silicon wafer was patterned and etched all the way down to the silicon nitride layer. The un-etched silicon structures served as the gate electrodes and as the fluid reservoirs. The device had high control over the EOF due to the ultra-thin silicon nitride microchannel wall. Moreover, using only $\pm$ 50 V gate voltages, the microdevice demonstrated reverse EOF.

Buch *et al.*

A hybrid silicon-plastic FEFC device was reported where the FEFC microchannel wall was composed of 2.4 μm thick silicon dioxide [75]. The microchannels were fabricated using micromolding [32]. A silicon wafer was etched

in KOH to form 45 μm tall, 100 μm wide, and 2 cm long structures. Then, PDMS was poured on to the mold and cured to replicate the silicon wafer master to create the microchannel structure. The PDMS was placed on a silicon wafer with a silicon dioxide coating. The microchannel had three walls that were PDMS and the bottom wall that was silicon dioxide. The gate electrode was the entire silicon wafer and the transverse electric field was transmitted through the silicon dioxide layer. The FEFC results for the hybrid silicon-plastic FEFC device were comparable to the previous LOC designs. However, the hybrid design of PDMS-silicon allowed for ease of fabrication.

2.4 Conclusion

The features of the electric double layer and electroosmosis, as they pertain to FEFC, are presented in this chapter. The electric double layer results from the charge separation at the fluid-wall interface. As a result of the non-uniform distribution of counter-ions near the interface, there exists a plane of shear, which has a potential known as the zeta potential. Under EOF, the counter-ions in the fluid move under the influence of the longitudinal electrical field and drag the neutral molecules with them. FEFC is a technique to adjust the counter-ion concentration at the plane of shear with a transverse electric field. Modulating the zeta potential with FEFC allows for dynamic control over the EOF without adjusting the longitudinal electric field. Lastly, the performance of FEFC has been modeled with the double capacitor theory.

The extension of FEFC from capillary electrophoresis into the area of microfluidics has been innovative, yet preliminary. The demonstrated materials used as the microchannel wall above the gate electrode have been confined to

inorganic materials. These materials do not lend themselves readily to inexpensive, disposable LOC devices [28]. To address this issue, the experimental research consisted of three key steps toward the realization of polymer FEFC microfluidic device technology: demonstration of FEFC in a single polymer microchannel, development of a polymer FEFC microfluidic network, and investigation into the system-level considerations for complex FEFC with analytical model validation.

Chapter 3

Silicon Microfluidic Multiplexer

The first research phase consisted of experimentation on a silicon-based FEFC device [79]. The focus of the initial work was to develop the research strategies necessary for the demonstration of an all-polymer FEFC device. The design, fabrication, and characterization of a silicon-based microfluidic multiplexer employing FEFC is described. Due to over-doping of the p-n junctions, the device lacked total gate independence, and only the characterization of a single microchannel was achieved.

The device was designed with a cross-shaped microchannel layout for four microchannels with independent FEFC gates (Figure 3.1). The multiplexer fabrication involved several traditional microfabrication steps to form the device. Selective p-type doping of an n-type silicon substrate created p-n junctions to provide electrical isolation for the FEFC gates. Deep reactive ion etching formed the microchannel network. Thermal oxidation growth of silicon dioxide coated the microchannel walls to serve as the dielectric layer covering the FEFC gates. Finally, a PDMS layer sealed the microchannels and formed the fluid reservoirs at each end of the four microchannels (Figure 3.2). The local zeta potential in each microchannel was modulated to control the EOF within each branch of the network. Experimentally, the control slope of EOF versus applied gate voltage

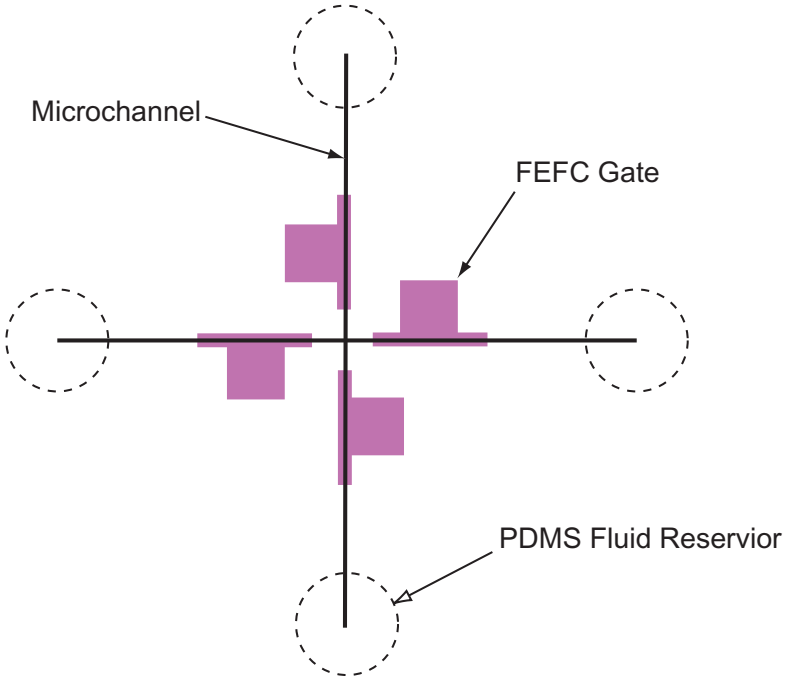

Figure 3.1: Microfluidic multiplexer layout.

was found to be within agreement with the theoretical prediction given by the double capacitor model from equation 2.16.

3.1 Fabrication

The device fabrication was out-sourced to the University of Michigan's Solid State Electronics Laboratory and the steps of the process are detailed in Figure 3.3. The microfluidic multiplexers were started on a 100mm n-type silicon wafer (4×10^{14} - 4×10^{15} cm^{-3}). The flow control gates were defined by selectively doping the wafer with boron to form p-type wells. The boron pre-deposition step was conducted at 1175°C for 8 hours. To diffuse the boron deeper into the substrate, the drive-in step was also at 1175°C for 8 hours. The boron diffusion steps resulted in a $7{\times}10^{19}$ cm^{-3} concentration at 15 μm deep from depth profiling.

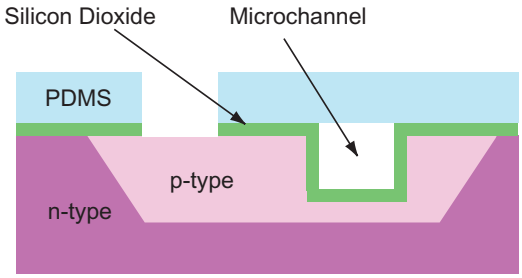

Figure 3.2: Cross-section of the microchannel with the PDMS sealing layer.

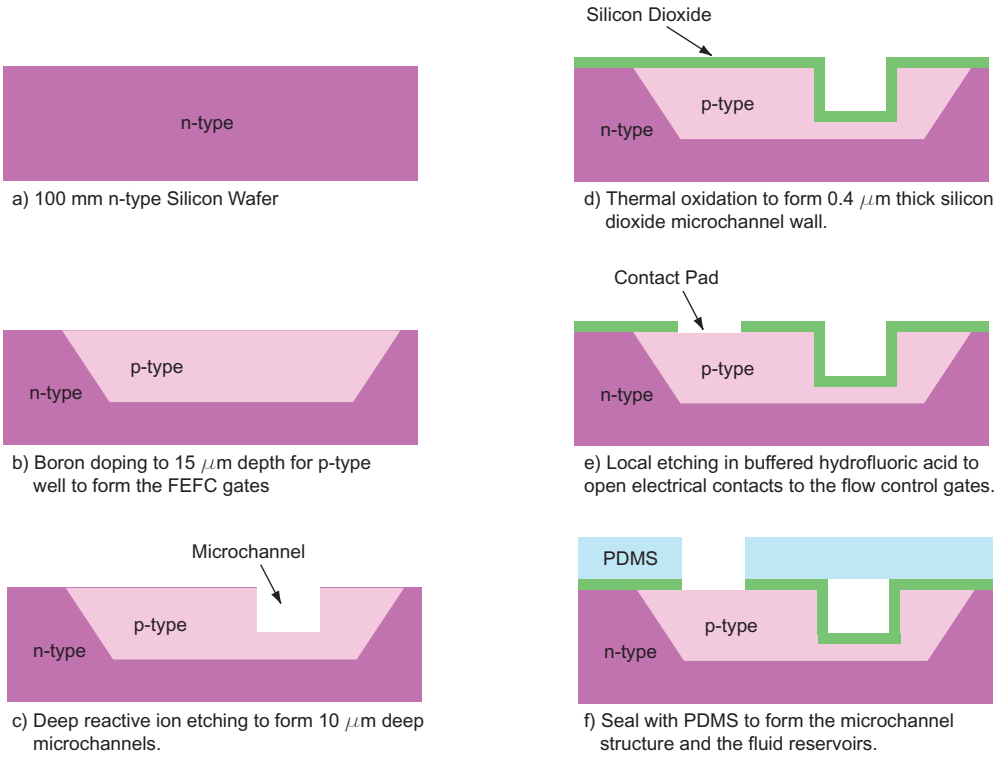

Figure 3.3: Fabrication steps for the microfluidic multiplexer.

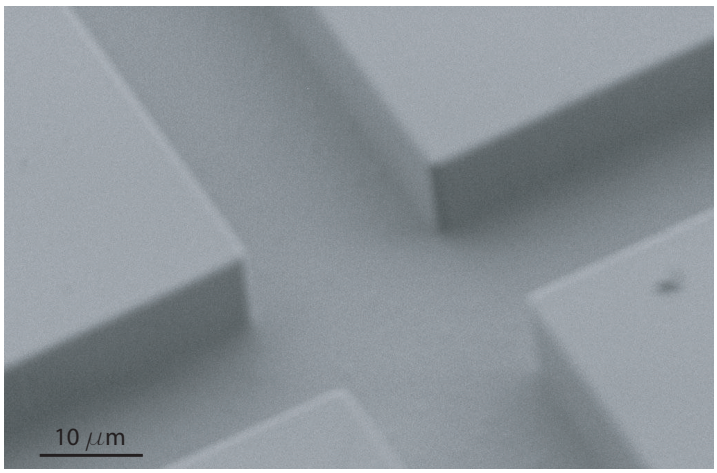

Figure 3.4: SEM image of the intersection of the microfluidic multiplexer.

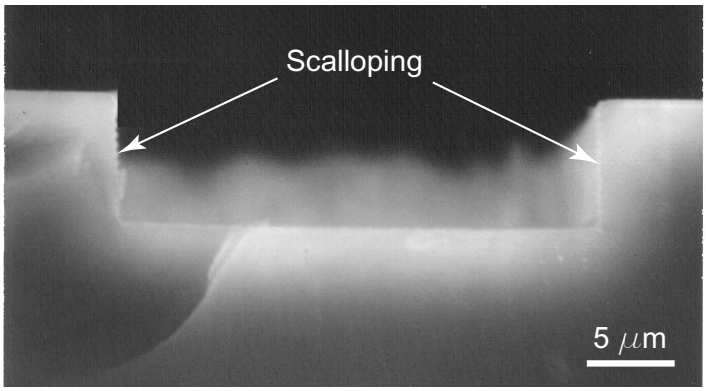

Figure 3.5: SEM image of the microchannel cross-section.

Deep reactive ion etching was used to form 10 μm deep microchannels. The layout of the multiplexer devices on the silicon wafer had microchannel widths of 10, 20, 30, 40, and 50 μm. Figure 3.4 is an SEM image of the intersection of the four microchannels of the microfluidic multiplexer. As seen in the SEM image, the DRIE process created microchannels with vertical sidewalls for microchannels with rectangular cross-sections. The scalloping at the vertical sidewalls is observable in the SEM image of 20 μm wide and 10 μm deep microchannel in Figure 3.5.

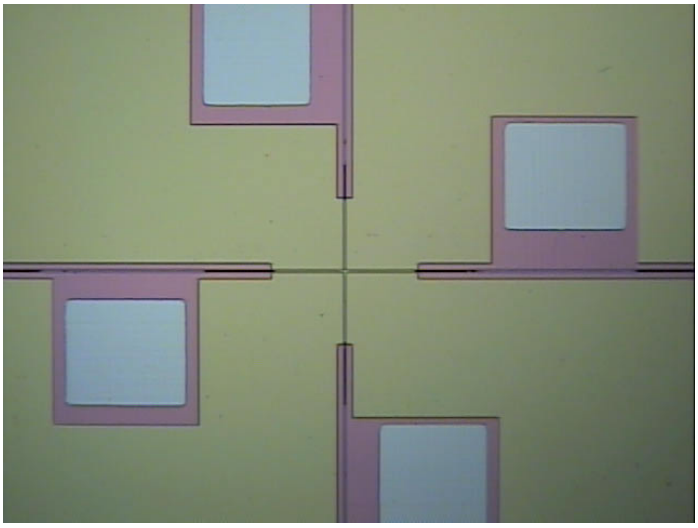

Figure 3.6: The silicon dioxide layer at the FEFC gates were etched for electrical contacts to the gates.

After forming the microchannels, the silicon dioxide was thermally grown on the substrate. The thin film formed three of the microchannel walls, through which the transverse electric field was applied. The silicon dioxide was grown with dry oxidation to a thickness of 0.4 μm to form the insulating layer.

After receiving the fabricated wafers, the SiO_2 layer at the p-type regions needed to be locally etched for electrical contacts to the gates (Figure 3.6). Masking of the device during the etching step was possible with a 1 mm thick slab of PDMS with patterned holes for the electrical contacts. The PDMS slab was aligned to the device and the adhesion sealing of the PDMS provided adequate protection of the unexposed SiO_2. The etching was performed in 7:1 buffered HF for 10 minutes to remove the insulating layer above the electrical contact areas. For testing, the microchannels were then sealed with another PDMS slab that contained the fluid reservoirs. The PDMS slab was aligned so that the fluid reservoirs were placed at the ends of the four microchannels.

3.2 Physics and Function of the Microfluidic Multiplexer

The independent operation of each flow gate in the microfluidic multiplexer depends on the ability of the p-n junction to allow current to flow easily in one direction only. An undoped silicon wafer has an intrinsic concentration of electrical charge carriers equal to the concentration of holes or vacant sites. Doping the silicon substrate with phosphorous introduces other atoms into the silicon lattice that have a higher number of valence electrons. The doping results in an n-type substrate that has an excess of electric charge carriers over the intrinsic concentration. During the FEFC gate fabrication, the boron doping introduces other atoms with a lower number of valence electrons at selective regions. This results in patterned FEFC gates with a high concentration of holes. The interface between the n-type substrate and the p-type FEFC gates is a p-n junction, a fundamental solid-state semiconductor structure. At the p-n junction, the two regions creates a charge depletion region (Figure 3.7). The excess electrons in the n-type region diffuse to the holes in the p-type region. As they combine with the holes, it creates a negative ion in the p-type region and leave behind a positive ion in the n-type region. The space charge build-up from the resulting negative and positive ions creates a depletion region the prevents further electron and hole migration.

Electrical isolation of the FEFC gates is achieved when the p-n junctions are under reverse bias, where the p-type region is negatively biased and the n-type region is positively biased [80]. The applied electric field increases both the width of the charge depletion region and the potential barrier. Under reverse bias, the excess electrons in the n-type region are drawn away from the p-n interface due to the positive bias. Likewise, the holes in the p-type wells are

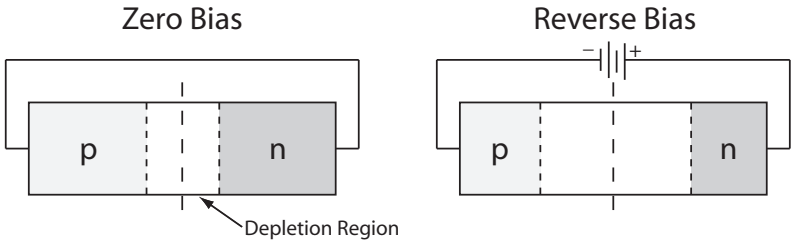

Figure 3.7: Biasing the p-n junction.

drawn away from the interface region due to the negative bias. The charge carrier depletion region allows each gate to be biased independently at a potential that ensures a reverse biasing across the p-n junction. Under this scheme, virtually no current flows between the gates so that each is electrically isolated from the other. However, the electrical field from reverse biasing, if sufficiently high, can result in breakdown of the depletion region, known as avalanche breakdown (Figure 3.8) [80]. Additionally, electron tunnelling or Zener breakdown could eliminate electrical isolation with current leakage. Therefore, the bias applied to the FEFC gates cannot exceed the voltage threshold barrier, V_B, which is determined from the doping levels of the silicon substrate.

The principles of FEFC are detailed in section 2.5 and so a description of FEFC operation in the microfluidic multiplexer is provided. The bias applied to the gate voltages directly controls the zeta-potential in each arm of the microchannel. The transverse electric field through the silicon dioxide layer changes the ion concentration in the diffuse layer. The degree of change in the zeta potential for the microfluidic multiplexer is proportional to the ratio of the capacitance of the silicon dioxide layer over the diffuse layer capacitance (C_W/C_D in equation 2.16). For example, the theoretical electroosmotic velocity, u_{eo}^{theory}, versus gate

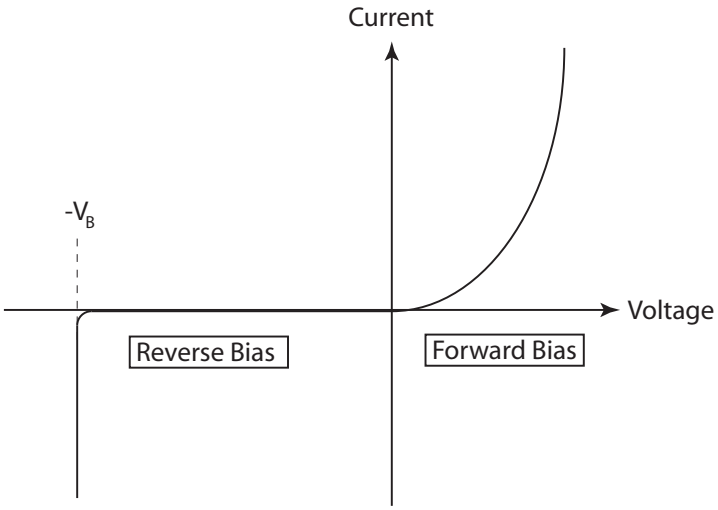

Figure 3.8: I-V curve for p-n junction.

voltage for the microfluidic multiplexer is

$$u_{eo}^{theory} = \frac{\epsilon\,(\zeta_0 - 2.5 \times 10^{-4}\ \ V_G)}{\eta} E \tag{3.1}$$

where V_G is in volts for a buffer solution at pH 3.

3.3 Characterization of the Microfluidic Multiplexer

An example of the gate testing on a MC Systems 8806 probe station is illustrated in Figure 3.9. The flow control for a range of applied gate voltages was characterized by current monitoring, a method previous researchers have employed to measure EOF [77]. Contact was made to the gate electrodes with tungsten probe tips (Cascade Microtech, Beaverton, OR). The gates were biased with power supplies (E-3612A, Agilent, Palo Alto, CA) from -100 V to 100 V. The voltage change over a 1 MΩ resistor was recorded with a data acquisition unit (34970A, Agilent, Palo Alto, CA) to measure the current change in the microchannel.

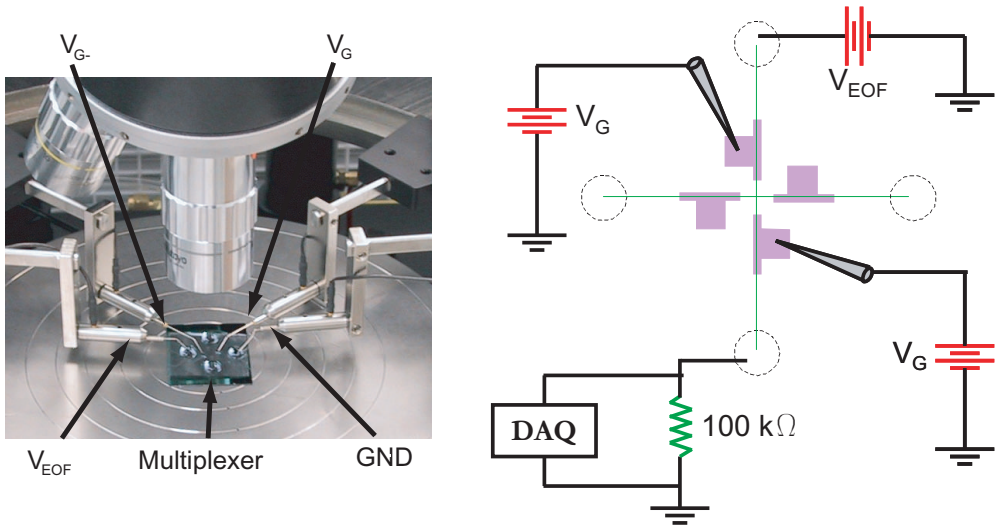

Figure 3.9: Testing of the microfluidic multiplexer.

3.3.1 Current Monitoring

The microchannel and reservoirs were filled with 20 mM phosphate buffer solution at pH 4 and the EOF voltages were applied at two reservoirs. The pH of all buffer solutions were measured with a pH meter (accumet* AB10, Fisher Scientific, Pittsburgh, PA). The anodic reservoir buffer solution was replaced with 19 mM solution and the data acquisition unit began recording the current through the microchannel. As EOF pumped the lower concentration buffer through the microchannel, the current dropped due to the change in conductivity of the buffer solutions. The EOF velocity was calculated from the measured microchannel length and the time for the current to drop to a new steady-state value, corresponding to when the 20 mM solution had been completely pumped out of the microchannel and replaced by 19 mM solution.

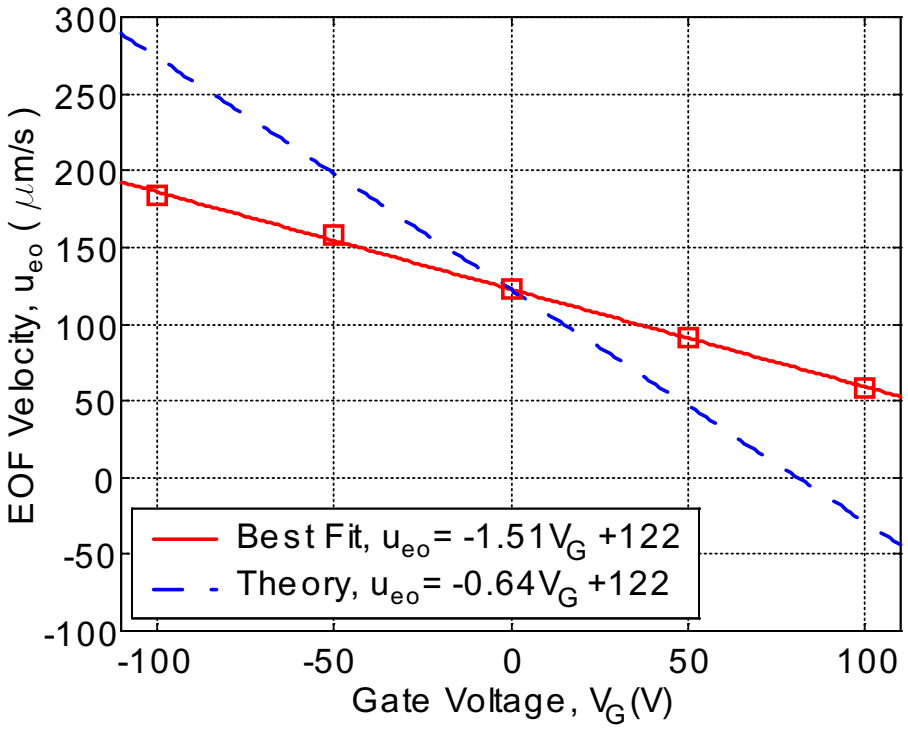

Figure 3.10: Comparison between experimental EOF velocity and the double capacitor model.

3.3.2 Comparison with Double Capacitor Model

An example of the flow control measurements is shown in Figure 3.10 and compared with the theoretical velocity given by the double capacitor model. The measurements were performed in a single microchannel with epsilon-amino-n-caproic acid (ϵ-ACA) buffer solution at pH 4 under an electric field of 93 V/cm. The flow control under these conditions exhibits linearity between applied gate voltage and the resulting flow velocity. The theoretical EOF velocity from equation 2.16 is also plotted with the experimental slope. Despite the difference in slopes, the experimental results demonstrate that FEFC was able to change the velocity of the EOF pumping from 150% to 50% of the original.

The current monitoring results presented here and throughout this dissertation work exhibited large variance, primarily due to different surface tensions at the reservoirs and surface contamination between tests. In changing the buffer solution at one reservoir for current monitoring, which typically had a volume of 400μL, the surface curvature of the new buffer solution was different from curvature of the old buffer solution. The difference in surface curvature between injections is an artifact of the manual filling process and surface roughness of the reservoir walls. The wetting of the buffer solution along the reservoir walls varied because of the manual injection of the solution from an automatic pipetter. For this reason, human error was a significant factor in running the experiment, since the same surface curvature could not be repeated between injections. As a result of the different fluid curvatures, the surface tension forces were different between the reservoirs, yielding net pressure forces at the reservoirs. The different pressure forces pumped the buffer solution through the microchannel, even without the application of the longitudinal electric field. With EOF, the pressure flow

impeded or sped up the bulk flow rate during current monitoring so that the measured velocity was not purely EOF. Characterizing the pressure flow component would be require characterizing the fluid curvature at both reservoirs, a difficult undertaking and outside the scope of this work.

Additionally, the fluid was removed from the microchannel between tests with vacuum force from a pipet-aid so that the microchannel could be filled with fresh buffer solution. It is likely to assume that contamination of the microchannel wall occurred during this removal process because of the air flow through the microchannel. The surface chemistry that generates the zeta potential is sensitive to adsorption chemistry at the microchannel wall and was likely to have changed between tests, yielding varience in the zeta potential and diffuse layer capacitances. Even though the data presented exhibits significant scatter, the phenomenon of field-effect flow control on the velocity of the electroosmotic flow is apparent throughout the data.

3.3.3 FEFC versus buffer pH

As described in section 2.2, the pH of the buffer solution determines the value of the surface charge, σ_0, at the microchannel wall. Decreasing the pH of the buffer solution reduces the inherent zeta potential and the capacitance of the diffuse layer. These changes result in increased control over the EOF. For comparison at three pH levels, the EOF mobility, which is the EOF velocity scaled by the EOF electric field, versus applied gate voltage is plotted in Figures 3.11 - 3.13. In a single microchannel of the microfluidic multiplexer, the slope of the EOF mobility versus the applied gate voltage was found to be -44 μm cm/(V^2 s) for phosphate buffer solution at pH 5 (Figure 3.13). In order to minimize the

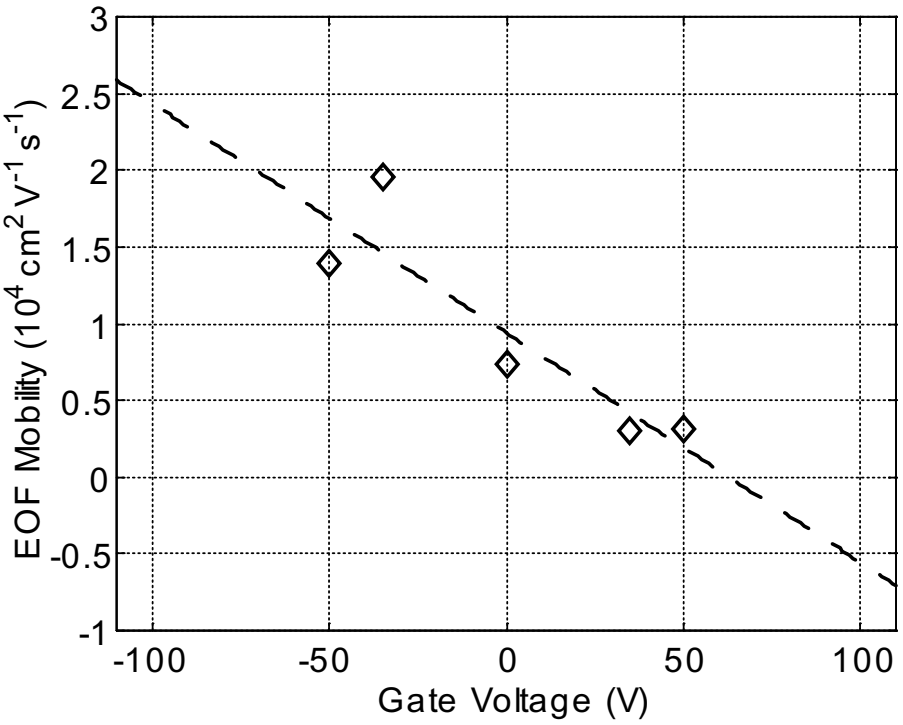

Figure 3.11: EOF mobility measurements, which is the EOF velocity scaled by the EOF electric field, versus gate voltage for ϵ-ACA buffer at pH 3.

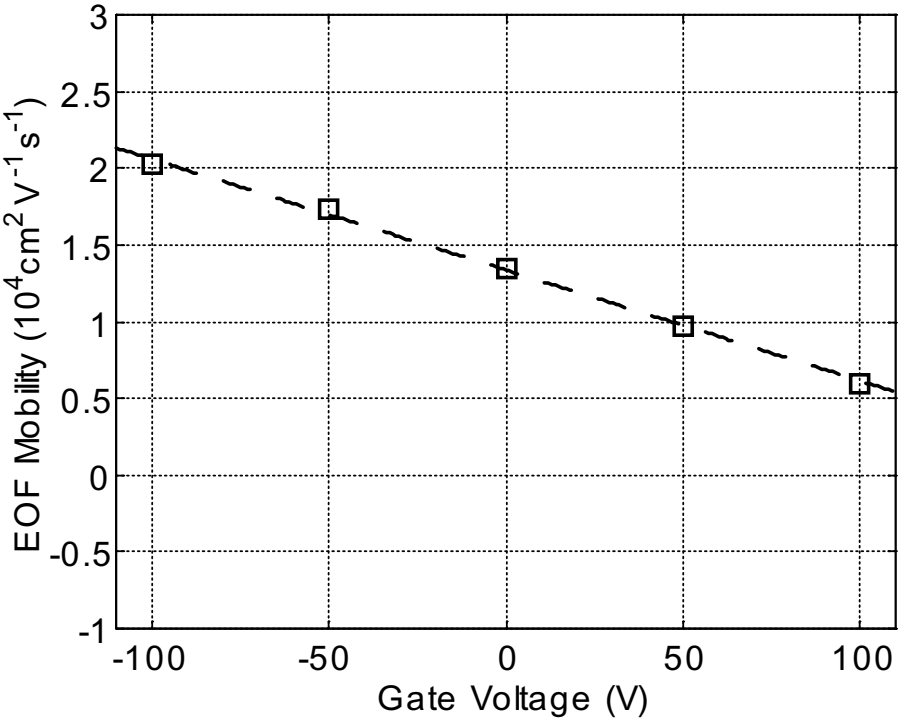

Figure 3.12: EOF mobility measurements versus gate voltage for ϵ-ACA buffer at pH 4.

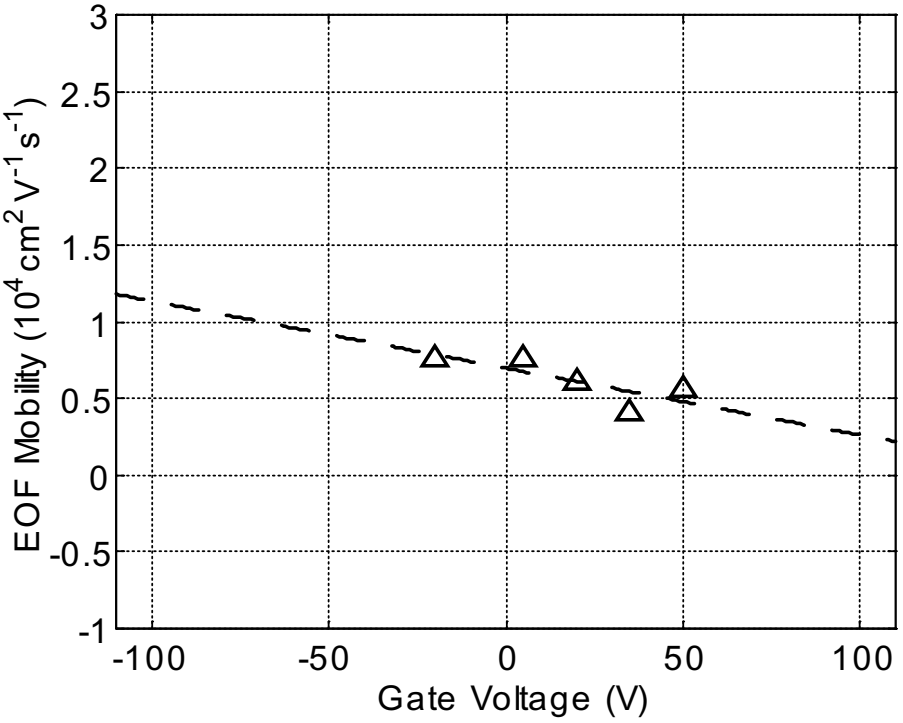

Figure 3.13: EOF mobility measurements versus gate voltage for PBS buffer at pH 5.

absorption of the buffer ions into the SiO_2, epsilon-amino-n-caproic acid (ϵ-ACA) buffer solution was used for further experiments. Thermally grown silicon dioxide has been reported to allow the diffusion of to positive ions through the film after an induction time with a negative biased on the underlying silicon, due to flaws in the film [81]. The ϵ-ACA molecule has a larger ionic radius than the phosphate molecule and so diffusion through the silicon dioxide layer, under the assistance of the FEFC electric field, would be lower. For the ϵ-ACA buffer, the control slope is -72 μm cm/(V^2 s) and -155 μm cm/(V^2 s) for pH 4 and pH 3, respectively. The FEFC slope values are shown in Table 3.1. These flow control experiments under various buffer conditions were found to exhibit similar linearity as predicted by the double capacitor model, however with significant scatter in the pH 3 results. The best-fit lines for all the results confirm that an inverse relationship exists between the FEFC slope and the buffer pH, which has been reported previously [64, 52].

Buffer	pH	FEFC Slope (μm cm/(V^2 s)
Phosphate	5	-44
ϵ-ACA	4	-72
ϵ-ACA	3	-155

Table 3.1: FEFC slopes for the microfluidic multiplexer.

3.3.4 Flow Visualization with Rhodamine B Dye

Current monitoring is only able to measure the velocity in a single microchannel. The microchannel or capillary acts as a variable resistor as the buffer solutions with different concentrations flow through and replace each other. Current

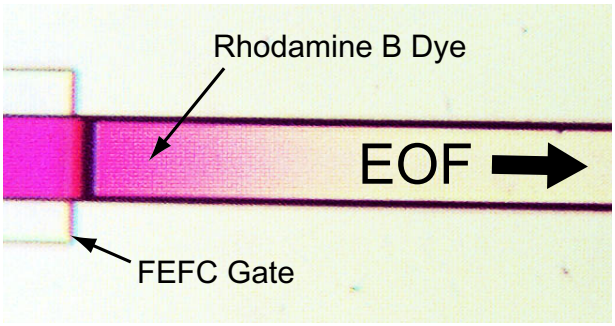

Figure 3.14: Visualization of Rhodamine B dye.

monitoring cannot be used to simultaneously measure the flow in two or more interconnected microchannels in a network design because the current splits or sums at the intersection. Flow visualization is required to measure the flow in interconnected microchannels.

In order to study the flow in multiple microchannels simultaneously, Rhodamine B dye (Fisher Scientific, Pittsburgh, PA) was added to the ϵ-ACA buffer solution at pH 4.9 and recorded under a CCD camera attached to the probe station. A sample of the image recording is shown in Figure 3.14 where the flow is from left to right. The edge of the flow control gate can be seen in the left side of the image. In order to use Rhodamine B as a velocity marker of the EOF, the dye molecule must not exhibit a charge in the buffer solution. If the molecule is charged, then it will move under the force of both electrophoresis and electroosmosis. Unfortunately, the measured dye velocities were greater than the velocities obtained by current monitoring. A literature search confirmed Rhodamine B could not be used as an EOF flow marker for FEFC. At low pH, where FEFC control is greatest, the dye is reported to be electrophoretically positive and only neutral at pH levels between 6.0 and 10.8 [82].

Even though Rhodamine dye was not adequate to quantify the EOF in the

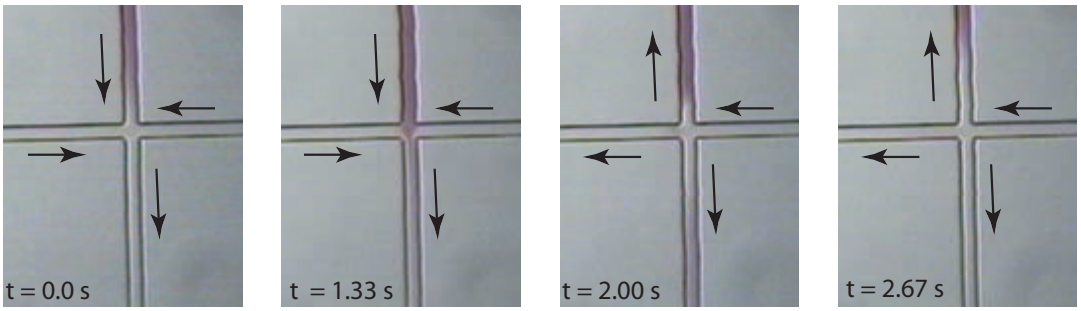

(a) (b) (c) (d)

Figure 3.15: (a) Dye flows down top microchannel. (b) Dye crosses the intersection and combines with flow from left and right. (c) Dielectric breakdown occurs and dye flows in two directions. The left microchannel flow reverses direction. (d) Dye flows faster in the bottom microchannel than the top.

microfluidic network, video obtained during the testing revealed the effect of electrical breakdown of the microchannel wall. The video in Figure 3.15 shows Rhodamine B dye flowing from top to bottom from $V_{EOF} = 60$ V. At the same time, the pressure driven flow from the left and right microchannels flowed to the intersection and down the bottom microchannel. When the dye front crossed the intersection (frame b), the dye in the intersection shows a wedge shape, due to hydrodynamic focusing. The wedge shape arises from the constriction coming from the pressure flow from the left and right microchannels. When the bottom FEFC gate is set to +120 V between frames b and c, electrical breakdown occurs in the microfluidic multiplexer.

At some point in the microchannel, a defect occurs in the insulating silicon dioxide. The defect acts as a third EOF electrode in the system, causing a split flow from two EOF electric fields. The gate voltage causes the flow in the upper and the left microchannels to reverse direction. The applied gate voltage was

below the dielectric breakdown for silicon dioxide (1000 V/μm). Therefore, the source of the breakdown may have been due to the scalloped sidewalls of the microchannel from the DRIE etching or from buffer ion diffusion through the silicon dioxide microchannel wall.

3.3.5 Overdoped p-n Junction

Beyond the breakdown of the silicon dioxide wall, further testing on the multiplexer was limited because of the high doping levels of the p-n junctions. The high boron doping levels causes the depletion region thickness to be dependent on only the excess electron concentration (N_D):

$$W = \frac{1}{N_D}\sqrt{\frac{2\epsilon_{Si}V_{bi}N_AN_D}{q(N_A+N_D)}}$$

Due to high boron doping, the concentration of holes is much greater than the concentration of excess electrons ($N_A \gg N_D$).

$$W = \frac{1}{N_D}\sqrt{\frac{2\epsilon_{Si}V_{bi}N_D}{q}} = 1.67 \ \ \mu\text{m} \tag{3.2}$$

where ϵ_{Si} is the dielectric constant of silicon, V_{bi} is the built-in voltage of the p-n junction, and q is the elementary charge [80]. The small depletion region causes the maximum electric field across the p-n junction without the onset of avalanche breakdown to be

$$E_m = \frac{qN_DW}{\epsilon_{Si}} = 1.03 \times 10^6 \ \ \text{V/m} \tag{3.3}$$

Thus, the maximum reverse bias possible without avalanche breakdown is

$$V_B = \frac{E_m^2\epsilon_{Si}}{qN_D} = -1.73 \ \ \text{V} \tag{3.4}$$

On account of this, the high boron doping levels limit the reverse bias voltage across the p-n junction to a significantly small voltage. Reverse biasing is critical

for the independent control of the FEFC gate. Without it, the current flows between the gates and the entire wafer becomes biased.

To compensate for the overdoping, the multiplexer device was thermally annealed at 900°C for 20 minutes in a nitrogen environment. The thermal energy from the annealing diffuses the boron atoms. The intent was to lower the dopant concentration and drive the dopant atoms deeper into the substrate. Before and after annealing, the reverse bias voltage threshold was measured experimentally on the probe-station (Figure 3.16). The current was measured through the p-n junction of the FEFC gate for a range of bias voltages. The I vs. V curve follows the theoretical trend illustrated in Figure 3.8 of forward and reverse biasing with avalanche breakdown. Before annealing, the overdoping of the p-n junction restricted the gate voltage bias to an experimentally measured range of 0 and -1.5 V without avalanche breakdown. After anealing, the range was slightly improved to 0 to -2.5 V. Further annealing at a higher temperature and for longer furnace time may improve the boron doping. However, for future fabrication runs of the silicon microfluidic multiplexer, the doping levels of the p-n junction must be sufficient for large reverse bias voltages.

The small voltage range for reverse bias made the gate regions not independent. With the silicon substrate biased at ground, the maximum gate voltages possible at two of the gates is -2.5 V. If the gate voltages were more negative than the reverse bias for improved flow control($V_G \leq -2.5$), avalanche breakdown would occur at the p-n junction and destroy the electrical isolation. As a result, only characterization the flow control in a single microchannel was possible and not the testing of microfluidic multiplexer of flow in multiple microchannels. Theoretically, if the doping levels were sufficient for a large depletion region,

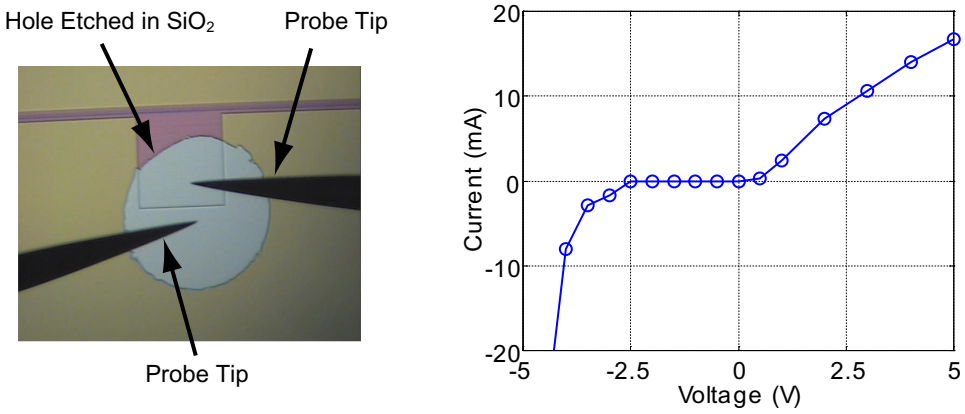

(a) (b)

Figure 3.16: (a) Measurement on the probe-station of the (b) I vs. V curve for the p-n junction of the FEFC gate.

then the reverse bias would be large. For example, the reverse bias is -75 V for a general-purpose diode like the 1N914 [83], which is satisfactory for FEFC voltages. Larger reverse bias voltages are possible with lower substrate doping

3.4 Conclusion

The primary purpose of working on the silicon-based microfluidic multiplexer was to develop research strategies for the development of a polymer-based FEFC device. The difference in control slopes between the three buffer solutions with different pH levels is expected due to the lower native zeta potential at low pH. The error between the experimental and theoretical control slopes in Figure 3.10 is reasonable, but the difference may be due to different zeta potentials between the PDMS and SiO_2 microchannel walls. Current monitoring was only adequate in characterizing the EOF control in a single microchannel and therefore flow visualization was attempted in the interconnected channels. However, prelimi-

nary experiments revealed that Rhodamine B was not adequate due to its electrophoretic mobility at low pH. Another visualization technique is necessary to accurately measure EOF. Additionally, overdoping the p-n junctions restricted the reverse voltage threshold to an experimentally tested range between 0 and -2.5 V. The small voltage range made the gate regions not independent so that multiplexing with FEFC was not possible. In transitioning to an all-polymer FEFC device, the experiments conducted on the microfluidic multiplexer shifted the focus to the selection of polymers with high dielectric strength, high dielectric constants, and ease of fabrication

Chapter 4

Field-Effect Flow Control in Polymer Microchannels

The motivation for FEFC in a single microchannel is for the realization of highly parallel systems for high-throughput analysis in drug screening as discussed in Section 1.2. In order to demonstrate FEFC on an all-polymer microchannel, it was necessary to investigate a range of polymer candidates for their suitability for FEFC implementation. With the lead polymer candidate, Parylene C, a single microchannel device was fabricated to characterize the degree of EOF control over a range of gate voltages.

4.1 Polymer Investigation

The range of polymers suitable for FEFC is limited because the transverse electric field across the polymer microchannel wall can lead to dielectric breakdown. The maximum electric field that a dielectric material can withstand without breakdown is called its dielectric strength, (E_B). If the FEFC electric field is made very intense ($E_{FEFC} \geq E_B$), it will begin to pull electrons completely out of the polymer molecules and the polymer thin-film will become conductive [84]. The avalanche of free electrons acts as a short between the gate electrode and the buffer solution in the microchannel. The FEFC electric field is critically limited by E_B of the thin-film polymer.

Additionally, as discussed in Section 2.3, the capacitance of the wall material determines the degree of EOF control in the double capacitor model. Recall equation 2.16:

$$\zeta_{FEFC} = \zeta_0 + \frac{C_W}{C_D}(V_G - V_i)$$

For effective control over the EOF with a polymer wall material, the wall capacitance must be increased. Selecting a polymer material with a high dielectric constant (ϵ) will increase the wall capacitance. Recall the relation for capacitance (equation 2.17):

$$C_W = \frac{\epsilon}{d}$$

Additionally, the thickness of the polymer wall, d, is inversely proportional to the wall capacitance. The wall thickness and applied gate voltage are factors that counterbalance each other. Reducing the wall thickness will increase the wall capacitance for improved FEFC, but the applied gate voltage must also be reduced in order to avoid dielectric breakdown.

Thin-film polymers developed for the integrated circuit industry typically have a low dielectric constant to improve signal transmission. With a low dielectric constant, the applied gate voltage must be increased in order to change the EOF. However, operation under high gate voltages will lead to electrical breakdown of the polymer material. Therefore, the dielectric constant and dielectric strength are the two key factors in the polymer material selection for FEFC. Table 4.1 lists the polymer candidates for FEFC and their corresponding electrical properties, which need to be maximized for operating under FEFC. The fourth column contains the FEFC quality factor used to evaluate the polymer materials, which is the product of the dielectric constant and the dielectric strength. Previous

FEFC materials have much higher quality factors: 10,000 for silicon nitride[1] and 4000 for silicon dioxide[2]. The high quality factors are predominately due to the excellent dielectric strength of these inorganic materials.

Polymer	Dielectric Constant	E_B (V/μm)	Quality Factor	Ref.
Parylene C	3.15	220-270	693-851	[86]
Cyclotene 4000	2.65	300	795	[87]
Pyralin PI2808	3.5	200	700	[88]
PVD PTFE	2.1	200	420	[89]
PDMS	2.65	21.2	56	[90]
Teflon AF 1600	1.93	21	40	[91]

Table 4.1: Electrical properties for FEFC polymer candidates.

4.1.1 Poly(dimethylsiloxane)

The first material investigated was PDMS, which was spun onto a silicon wafer to a 10 μm thickness and cured. Due to the low E_B listed in Table 4.1, PDMS exhibited catastrophic breakdown - arcing between the electrode and silicon wafer when under low electric fields. Some FEFC testing data were collected, but gate voltages sufficient to modify the EOF were not possible due to dielectric breakdown.

[1]Silicon nitride: $\epsilon = 10$, $E_B = 1000$ V/μm [85]

[2]Silicon dioxide: $\epsilon = 4$, $E_B = 1000$ V/μm [85]

4.1.2 Poly(tetrafluorethylene)

PTFE is an excellent moisture barrier polymer but has not been used extensively as a microfluidic polymer material [92]. One form of PTFE is Teflon AF, which is a spin-on polymer. Since Teflon AF has a quality factor similar to PDMS, it was not tested. Another method for deposition of PTFE, is physical vapor deposition (PVD). This polymer material was deposited to a 1 μm thickness on a 2" by 2" stainless steel square (Advanced Surface Engineering, Elderburg, MD). When a drop of 20 mM acetic buffer pH 4.0 solution was applied to the PVD PTFE, the buffer solution locally dissolved the polymer material. The acid susceptibility of PVD PTFE restricted the use of this polymer material in the FEFC device, since low pH buffers are used for increased FEFC performance.

4.1.3 Benzocyclobutene-based Polymers

Cyclotene BCB 4000 is a thermoset polymer with a high curing temperature of 265°C that can be spin-coated. The resins are derived from B-staged bisbenzocyclobutene (BCB) monomers and are formulated as high-solids, low-viscosity solutions. The polymer was spun onto a silicon wafer with an aluminum metal layer and cured. Although it has a high FEFC quality factor, electrical breakdown of the polymer occurred frequently while testing. Visual inspection of the Cyclotene BCB showed pinholes in the polymer coating after the curing process. The pinholes caused this polymer to be rejected as a candidate material for polymer FEFC. Also, the high curing temperature of Cyclotene BCB severely limited its compatibility to other polymer substrates with low melting temperatures such as polycarbonate. An all-polymer FEFC device using Cyclotene BCB would have to be built on high temperature polymers such as poly(ethylethylketone) (PEEK)

and fiberglass.

4.1.4 Polyimide

Pyralin PI2808 is a polyimide polymer that can be spun-on. Polyimide is permeable to moisture and has been used as a humidity sensor in MEMS applications [93]. Molecules diffuse very rapidly through it [85]. The absorption of moisture and ions can degrade the performance and reliability of the film. The curing temperature for the spin-on polyimide is 350°C, which restricts its use to only high temperature polymers.

4.1.5 Poly(para-xylylene)

Parylene is a common name for a class of polymers called poly(para-xylylene). Six forms of parylene are currently available. Each form represents the basic polymer backbone of xylylene with a replacement of 1-4 atoms in the ring. The basic structure of the parylene polymers are shown in Figure 4.1. Due to its ease of fabrication and compatibility with polymer substrates, parylene has made its way into micromachining in the last few years. It has been used in numerous microfluidic applications for microchannel structures [40], electro-spray tips [41], micro-needles [94], micro-check valves [42], diaphragms [95], and integrated on-chip detectors [43]. The parylene surface groups can be made functionalized for protein binding [96, 97, 98, 99].

Parylene polymers are deposited by vapor deposition at room temperature in a vacuum. Figure 4.2 shows a diagram of the deposition process, known as the Gorham process [86]. The parylene dimer (solid) is first sublimated at 120-170°C. The vapor is then drawn into the pyrolysis chamber where the dimer molecule is

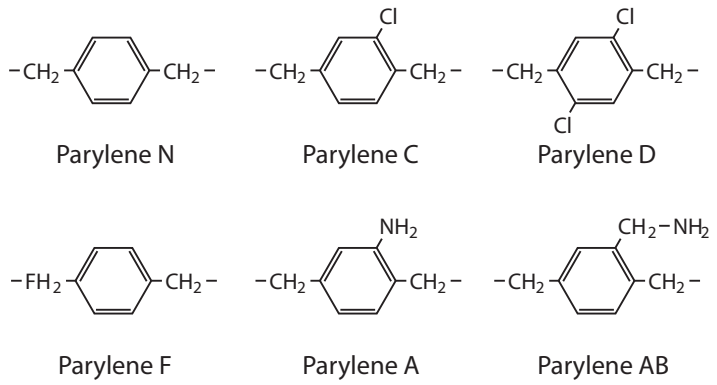

Figure 4.1: Molecular structure of Parylene monomers.

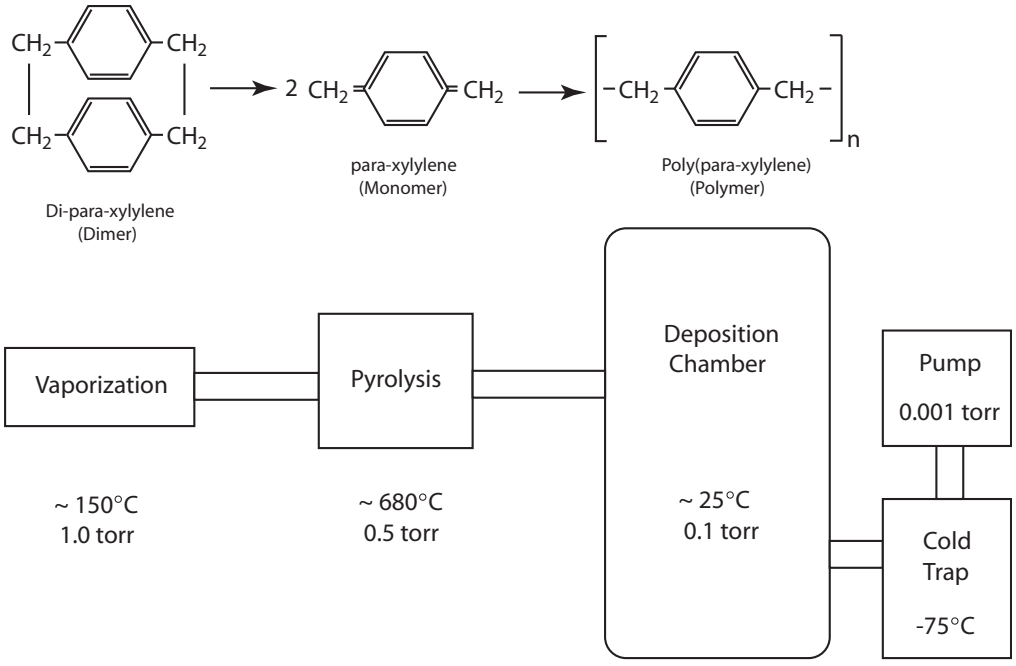

Figure 4.2: Chemical vapor deposition of Parylene.

then split into two monomers at 680-720°C. The monomers will then polymerize on surfaces below 100°C, although the deposition chamber is typically at room temperature. The low temperature of the deposition chamber is compatible with a wide range of plastic substrates with low melting temperature, e.g. polycarbonate or PMMA. Since the deposition is done at 0.1 torr, the mean free path of the monomer is on the order of centimeters (0.1 cm), which creates pinhole-free conformal coatings. Unlike vacuum metallizing that has a high mean free path, the deposition of the Parylene monomer is not line of sight due and all sides of the object are uniformly impinged. The deposition process has excellent thickness control down to the sub-micron range.

Once deposited, the parylene film is among the most robust organic polymeric coatings [86]. Of the parylene forms, Parylene C has the highest dielectric constant. The melting temperature of Parylene C is 290°C. When the film is at a temperature below the melting temperature, it is resistant to all solvents. When exposed to a solvent, the film may experience swelling up to 3% in volume. Additionally, the film is optically transparent down to 290 nm with low background fluorescence. The FEFC experiments with Parylene C exhibited electrical breakdown of Parylene C at gate electric fields greater than 100 V/μm with acetic acid buffer solution at pH 4. The combination of fabrication quality and excellent electrical properties make Parylene C an ideal polymer candidate for FEFC.

4.2 Single Channel Polymer FEFC Device

FEFC was demonstrated for the first time in a polymer microfluidic device where the applied electric field is transmitted through the polymer microchannel wall. Previous researchers have used polymers for FEFC device, but it was used

to form the passive microchannel walls while the FEFC electric field was applied through the silicon dioxide microchannel wall[75]. The use of an all-polymer FEFC device allows for the realization of an inexpensive, disposable microfluidic device. In this dissertation work, the first polymer FEFC device used a silicon wafer as the gate electrode but later devices were fabricated with metal layers on polycarbonate or glass substrates to demonstrate the cost effectiveness. The second study examined the FEFC control for gate electrodes that partially span the full length of the microchannel.

4.2.1 Full Length Gate Electrode

The first generation on the way towards an all-polymer FEFC device was built on silicon wafers for the fabrication convenience of a planar, polished substrate. Later generations were fabricated on glass and polycarbonate substrates. The bottom microchannel wall was Parylene C through which the FEFC electric field was transmitted. Micromolded PDMS formed the remaining three walls of the single microchannel. The PDMS seal to the Parylene C layer was reversible so that the devices were easily cleaned between tests. The reversible seal of PDMS is due to its elasticity which allows for a high degree of contact to the Parylene C film with van der Waals bonding. The seal is fast, watertight, and occurs at room temperature. The gate voltage was applied to the silicon wafer, which acted as the electrode underneath the polymer microchannel wall.

Fabrication

Parylene C was chemically vapor deposited onto a 100 mm silicon wafer (Silicon Quest Intl., Santa Clara, CA) to a 1.2 μm thickness (Specialty Coating

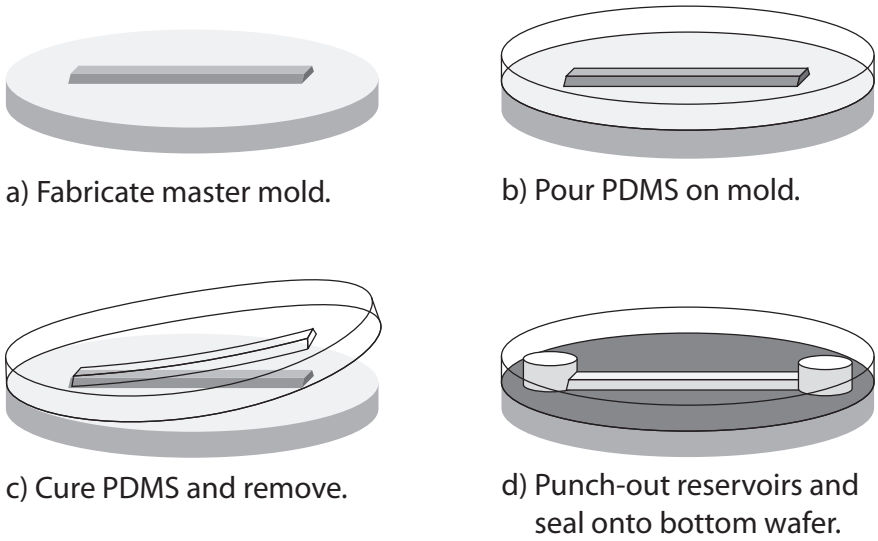

Figure 4.3: PDMS micromolding process.

Systems, Indianapolis, IN). The top and sides of the microchannel were micromolded polydimethylsiloxane (PDMS) [32]. The master mold for the PDMS was a second 100 mm silicon wafer (Silicon Quest Intl., Santa Clara, CA) with 2.0 μm of silicon dioxide. The silicon dioxide was patterned with AZ5214 (Clariant, Somerville, NJ) and etched in 5:1 buffered HF acid (J.T Baker, Phillipsburg, NJ). The silicon dioxide layer masked the underlying silicon during the next etch step. The wafer was placed in a bath of preferential silicon etchant (Transene, Danvers, MA) at 60°C to etch the microchannel features of the master mold. The microchannel were molded from PDMS (Sylgard 184, Dow Corning, Midland, MI) that was poured onto the silicon wafer master (Figure 4.3). The PDMS was cured for 2 hours at 60°C in a convection oven. Holes that were 5 mm in diameter, were punched into the ends of the microchannels to serve as the fluid reservoirs. The PDMS microchannel was 17 mm in length, 40 μm in depth, 100 μm in top width, and 150 μm in bottom width due to the etched crystal planes

of the silicon template. The PDMS layer was reversibly sealed to the Parylene C layer to fully assemble the FEFC device.

Experimental Procedure

The FEFC testing set-up was similar to the silicon-PDMS FEFC device reported by Buch *et al.* [75]. However, the silicon wafer was biased with a gate voltage instead of connecting it to ground. The entire silicon wafer underneath the Parylene C film acted as the gate electrode to transmit the FEFC electric field through the microchannel wall. The device was tested on an REL-4800 probe station (Cascade Microtech, Beaverton, OR). Contact was made to the silicon wafer with a tungsten probe tip (Cascade Microtech, Beaverton, OR) through the Parylene C film. The electrode was biased with a power supply (E-3612A, Agilent, Palo Alto, CA). The applied gate voltages to the silicon wafer ranged between $\pm$120 V, $\pm$60 V, and 0 V, which were below the voltage breakdown threshold for the deposited polymer thickness.

Current monitoring was used to measure the change in EOF velocity versus applied gate voltage. The voltage change over a 100 kΩ resistor was recorded with a data acquisition unit (34970A, Agilent, Palo Alto, CA). This testing method is described in section 3.3.1. To improve the FEFC performance, a buffer solution with a lower pH was used. The velocity was measured as 10 mM acetic buffer solution pH 3.1 replaced 20 mM acetic buffer solution in the microchannel. A diagram of the testing layout is shown in Figure 4.4.

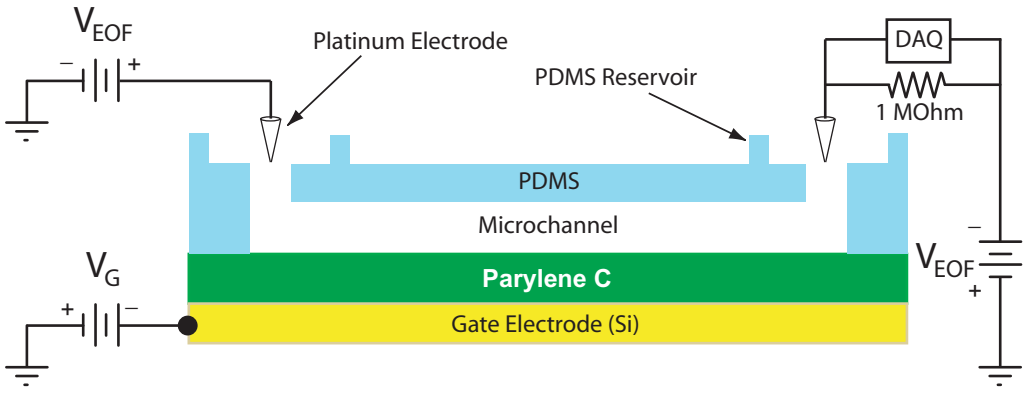

Figure 4.4: Diagram of testing circuit for the polymer-based FEFC microchannel.

4.2.2 Full Length Results

Five tests were conducted for each of the five applied gate voltages on one device. The EOF velocity measurements for the experiments are plotted with error bars, representing standard deviation, in Figure 4.5. The variation in the data is attributed primarily to pressure-driven flow in the microchannel due to a pressure gradient from unequal dispensed volumes in the fluid reservoirs between tests. For comparison, the double capacitor model is plotted alongside the data. For the model, the calculated Parylene C wall capacitance was 2.29 $\times 10^{-3}$ F/m^2 and diffuse layer capacitance was 0.236 F/m^2. The average buffer concentration of 15 mM was used to determine the diffuse layer capacitance.

The theoretical control slope, which is the slope of the line for the EOF velocity versus applied gate voltages, is equal to -5.3 μm cm/(V^2 s). The FEFC slope for Parylene C is lower than the control slopes obtained for the silicon microfluidic multiplexer. The difference is due to the increase wall thickness of the Parylene C (2.4 μm versus 0.4 μm) and lower dielectric constant (3.15 versus 3.9). From the double capacitor theory, the modified zeta potential was

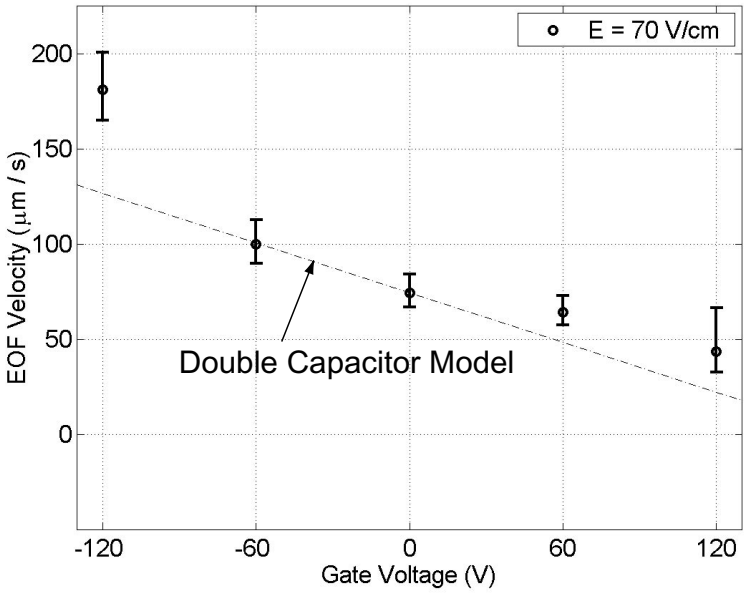

Figure 4.5: EOF velocity versus gate voltage in a single Parylene C microchannel. Error bars represent the standard deviation for five tests at each gate voltage.

predicted to vary from -23 to -4 mV. Solving for the zeta potential from the Smoluchowski equation, the experimental zeta potential varied from -33 to -8 mV over the applied gate voltage range. Given the measurement variations that are common to current monitoring, the experimental zeta potentials are close to the theoretical zeta potentials.

The experimental results do not agree with the linear relationship predicted in the double capacitor model due to nonlinear behavior at high negative gate voltages. The applied gate voltages changed the EOF by 240% to 60% of the original. Reverse EOF was not attainable because dielectric breakdown of the Parylene C was frequently observed at high positive gate voltages ($V_G > 120$ V).

4.2.3 Partial Length Gate Electrode

The second FEFC study examined whether EOF control is possible for gate electrodes that partially span the length of the microchannel. The study has implications for applications where a high density of independent gates is needed, such as microfluidic networks. Previous FEFC studies in fused silica capillaries showed that a small gate electrode area exhibited relatively the same EOF control as large gate area [68]. The gate electrodes were formed from gold layers that were deposited on polycarbonate substrates and patterned with lithography.

Fabrication

The substrate for the devices were polycarbonate wafers with 3" diameters (Makrolon, Sheffield Plastics Inc., Sheffield, MA). The wafers were placed in an e-beam evaporator for metal deposition. The chromium layer was first evaporated onto the polycarbonate substrate to a 200 Å thickness to serve as the adhesion layer for the next metal layer. The second layer was gold deposited to a 3500 Å thickness. The metal layers were patterned with AZ5214 (Clariant, Somerville, NJ) and the exposed metal areas were removed with Au and Cr etchant (Transene, Danvers, MA). The thickness of the metal layers is sufficient to protect the underlying polycarbonate from the solvents in the photoresist [100]. After the metal patterning, the resulting gate electrodes varied in length, L_G, between 1.0 cm to 0.1 cm.

With the metal electrodes patterned, the polycarbonate was coated with Parylene C to a 1.2 μm thickness (Specialty Coating Systems, Indianapolis, IN). The Parylene C film was the bottom wall of the microchannel that coated the metal electrodes. The top and side walls of the microchannel were PDMS made from

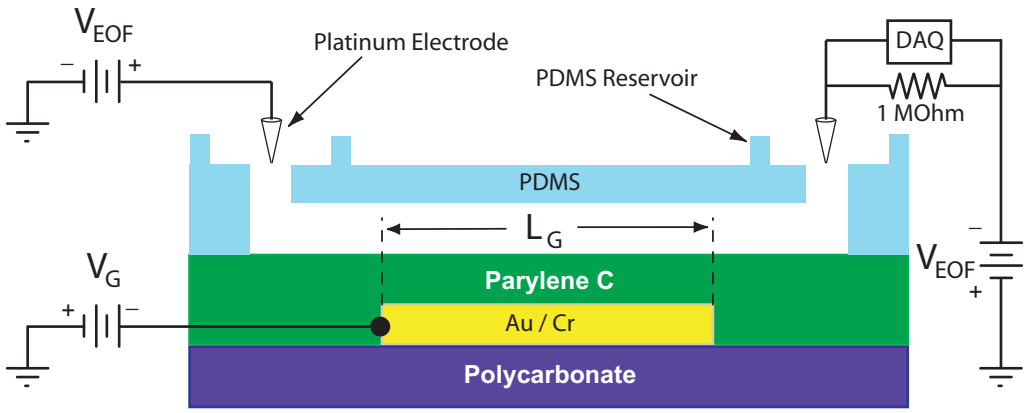

Figure 4.6: Diagram of the testing circuit for the polymer-based FEFC microchannel for gate length study.

the master mold from the full length study (Section 4.2.1). Therefore, the microchannel dimensions were the same as those in Section 4.2.1. The devices were assembled with the gate electrodes at the midpoint of the microchannel. Devices were studied with 66%, 16%, 13%, and 5% coverage area.

Experimental Procedure

The zeta potential was regulated through biasing the Cr/Au metal layers beneath the Parylene C, thus achieving field-effect flow control in the polymer microchannel. A diagram of the device layout is shown in Figure 4.6. Devices were assembled with different L_G to study if reduced gate coverage adversely affects FEFC. Current monitoring was used to measure the EOF. The devices were tested using the same experimental system as the full gate electrode case in Section 4.2.1. The EOF mobility was determined from current monitoring as 10 mM acetic buffer solution replaced 20 mM acetic buffer solution at pH 3.1. The devices were tested at gate voltages of ±90 V, ±60 V, ±30 V, and 0 V.

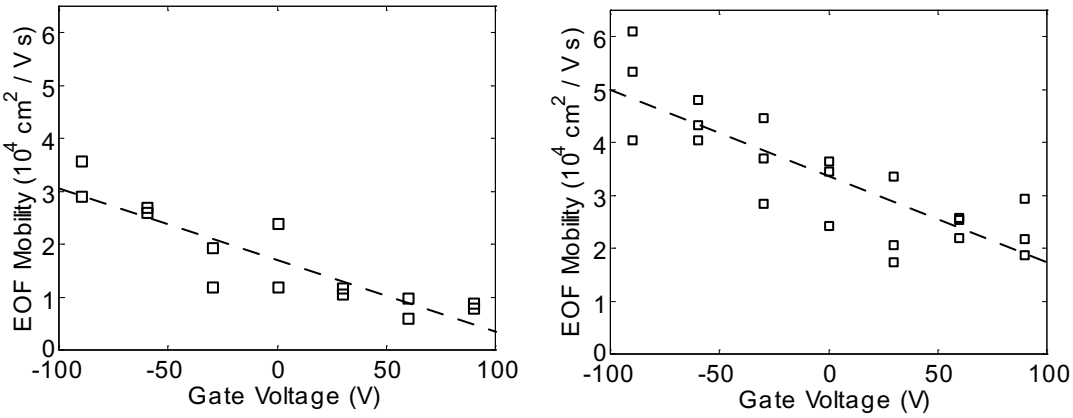

(a) (b)

Figure 4.7: EOF mobility measurements versus gate voltage for (a) 66% gate coverage and (b) 16% gate coverage.

4.2.4 Partial Length Results

The EOF mobility versus gate voltage results for 66% and 16% coverage are shown in Figure 4.7 and for 13% and 5% coverage in Figure 4.8. The results are shown as single data points and the each figure contains the results from one device for each coverage area. Best-fit lines are plotted with the data to determine the control slope for the applied voltages. The scatter in the data is attributed to a pressure gradient in the microchannel from unequal dispensed volumes at the fluid reservoirs between tests. Additionally, the four plots are shown with the same axes for slope comparison. The data for the 66% coverage area have a y-intercept that was lower than the other three tests, which means that the EOF mobility was lower for a gate voltage of zero than the other three cases. The lower EOF mobility may be a result of the larger coverage area. Despite this, the results show that FEFC is possible at low gate coverage.

At the edges of the gates, the internal voltages in the microchannel are dif-

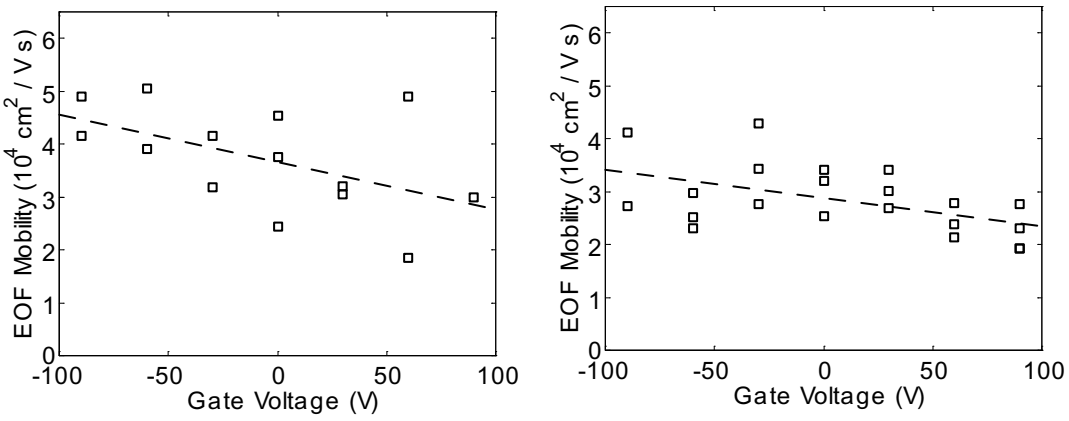

(a) (b)

Figure 4.8: EOF mobility measurements versus gate voltage for (a) 13% gate coverage and (b) 5% gate coverage.

ferent because of the longitudinal electric fields, E, which are shown in Table 4.2. In the double capacitor model, the difference between the gate voltage, V_G, and the voltage potential above the gate region, V_i, determines the transverse electric field. However, even for zero gate voltage, a transverse electric field is transmitted across the microchannel wall because of the nonzero values of V_i at the gate. Since V_i varies linearly across the microchannel, the values of V_i at the gate vary as well. As a result, the magnitude of transverse electric field varies linearly across the gate. At one end of the gate, there is a lower transverse electric field than at the other end. As a result of this, the zeta potential is lower at one end of the gate than at the other. As a result of this, for the 66% gate coverage, the minimum and maximum values for zeta potential at the edges of the gate are larger than the other three, due to the larger area and larger range of V_i. The interaction of the linearly varying zeta potentials may be the source for the lower EOF mobilities observed for the 66% coverage tests.

Gate Coverage	L (cm)	E (V/cm)	V_i (V)
66%	1.53	52.3	±26.2
16%	1.86	43.0	±6.5
13%	1.57	51.0	±5.1
5%	1.86	43.0	±2.2

Table 4.2: Total microchannel length (L), longitudinal electric field (E), and internal voltages (V_i) in the polymer microchannel.

The slope of the best-fit line through the data measures the degree of EOF control versus gate voltage, i.e. the FEFC control slope. The slopes for each test are listed in Table 4.3. The FEFC slope is approximately the same for all tests despite the scatter in the data. The 5% coverage device demonstrated a lower FEFC slope than the others, which may be due to the gate coverage. Overall, the closeness of the control slopes indicates that small gate regions can sufficiently generate FEFC in a polymer microchannel. Using smaller gate areas would allow for other microfluidic components to be integrated along the same microchannel, such as micro-heaters [100] or detection windows [20]. Additionally, smaller gate areas would enable multiple gates to be position along the microchannel for electroosmotic mixing with non-uniform zeta potentials [101, 102, 103, 104]. For microfluidic networks, FEFC with smaller gate areas allows for a high density of microchannel to be interconnected on a LOC device. Each microchannel within the network would have its own EOF control for the realization of M×N networks.

Gate Coverage	FEFC Slope (μm cm/(V^2 s))
66%	-14
16%	-16
13%	-9
5%	-5.3

Table 4.3: FEFC slopes for the polymer microchannel.

4.3 Conclusion

Several polymers were investigated for their performance and compatibility in an all-polymer FEFC device. The critical properties of the polymers are the dielectric constant and dielectric strength. These two values determine the change in EOF for an applied gate voltage in FEFC. Of the polymers investigated, Parylene C had the highest quality factor for FEFC and fabrication compatibility with other polymer substrates. Therefore, this polymer was chosen for the fabrication of the all-polymer FEFC device.

Parylene C allows for the development of an all-polymer microfluidic device that uses FEFC to control the EOF. The bottom gate electrode was initially a silicon wafer that was coated with the polymer. Second generation devices were built on a polycarbonate wafer with metal electrodes for an all-polymer FEFC device. The later tests confirmed that FEFC is possible with gates that do not span the full length of the microchannel. The control slopes were lower than the silicon-based microfluidic multiplexer due to the wall thickness and lower dielectric constant. Despite the lower performance, the devices were able to change the EOF by 260% to 40% of the original value.

Presented in this chapter is the first demonstration of FEFC through a poly-

mer material. Previous research in FEFC have used inorganic materials as the microchannel wall, through which the transverse electric field is applied. Parylene C enables a cost reduction in the implementation with comparable fabrication performance. Moreover, the demonstration of FEFC in an all-polymer microchannel is promising for inexpensive high-throughput analysis.

Chapter 5

Field-Effect Flow Control in a Polymer Microfluidic Network

The next research phase explored the development of an all-polymer microfluidic network with integrated FEFC gates. The implementation of FEFC has the ability to compensate for electric field interactions at the intersections of microchannels with internal flow control components. As discussed in Section 1.3, the operation of microfluidic networks without flow control becomes input-limited and all the internal flows cannot be controlled independently. The use of FEFC in microfluidic devices enables dynamic changes to the local zeta potentials, without having to change the surface coatings in the microchannel. Addressable flow control allows the network to be adjusted during operation.

In order to study the control of the EOF in the microfluidic network, a flow visualization technique using fluorescent polystyrene microparticles was developed. The microfluidic network had independent FEFC gates, which allowed for different EOF pumping rates in the microchannels. The network was first demonstrated as a planar microfluidic device with a T-intersection. Collaboration with Calibrant Biosystems enabled the development of a 3D microfluidic network using FEFC gates.

5.1 Flow Visualization

As discussed briefly in Section 3.3.4, measuring the flow in the microchannel with current monitoring [77] is limited to straight channels or capillaries. Current monitoring is adequate for determining the bulk flow of the fluid in a single microchannel or capillary since the change in current corresponds to the velocity of the buffer solution. For characterization of EOF in FEFC microfluidic networks, an imaging technique needed to be developed that enabled velocity measurements in interconnected microchannels. Flow visualization is critical for FEFC since the change in zeta potentials will induce a pressure that disrupts the plug-like flow of EOF.

In selecting a flow marker for imaging the EOF, the dye or sample plug needed to be neutral at the pH level of the buffer solution. However, at low pH, where field-effect flow control is greatest, most dyes exhibit a positive electrophoretic charge. The additional electrophoretic velocity toward the cathode results in a visualization measurement of both the EOF and the electrophoresis. Recall that charged state at low pH was observed for Rhodamine B dye. Therefore, the methods of caged fluorescence, alternative fluorescent dyes, Shah convolution detections, and micro-particle image velocimetry were investigated.

5.1.1 Caged Fluorescence

Caged fluorescence [23, 78, 105, 106] is a method to measure EOF in a microchannel. The caged dyes are fluorescent dyes that have been made non-fluorescent through the binding of chemical groups, which are also present in the solution. A pulse of focused UV light (365 nm) unlocks a small volume of the dye, which then fluoresces for illumination. The illuminated spot serves as a flow

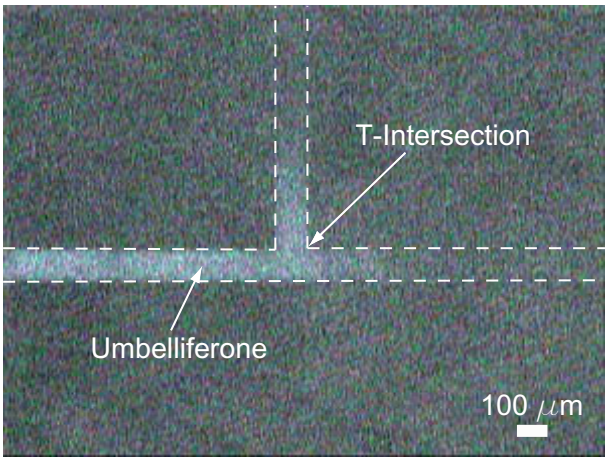

Figure 5.1: Microchannel T-intersection with umbelliferone dye used to characterize flow.

marker for recording the flow as it travels down the microchannel with the EOF. The method is not suited for FEFC because the caged fluorescent dye and buffer solution typically have a high pH. Recent studies report that the inclusion of the caged fluorescent dye increases the EOF because it changes the zeta potential at the microchannel wall [107, 108].

5.1.2 Fluorescent Dye

The mobility of a sample plug or dye is another method to measure the EOF but the choice of neutral markers at low pH is limited [82]. Umbelliferone has been used to measure the EOF velocity in polymer capillaries at low pH [109]. It has an excitation at 330 nm wavelength and an emission at 390 nm. Umbelliferone (Fisher Scientific, Pittsburg, PA) was dissolved to a 10mM concentration in 20 mM acetic acid buffer solution at pH 4. When injected into the microchannel, the dye illuminated with poor intensity as seen in Figure 5.1. Higher concentrations of umbelliferone were not possible without the onset of salt precipitation.

Additional investigated dyes were BODIPY FL and Oregon Green 488 (Molecular Probes, Eugene, OR). These fluorescent dyes have excitation at 504 nm and 490 nm and emission at 511 nm and 514 nm, respectively. The dyes were prepared separately with 20 mM acetic acid buffer at pH 4. When illuminated in the microchannels, the fluorescent intensity was too low to be observed. The low intensity is a result of the low pH of the buffer solution. The dyes illumination intensity falls off at pH levels below neutral (pH $\leq$ 7) and no fluorescence is possible at low pH (pH $\leq$ 5) [110].

5.1.3 Shah Convolution Detection

Shah convolution Fourier transform is another technique to measure the velocity in microfluidic devices [111, 112, 113]. In this method, a mask with a periodic array of slits is fabricated on the microchannel or superimposed onto the video. The slits spatially modulate the excitation beam aimed at the microchannel. Fluorescent microparticles with micrometer to nanometer diameters are introduced into the flow. When the microparticles flow across the slits, the spatial modulation is converted into a temporal modulation. The distribution of velocities is found with a Fourier transform of the temporal signal. After the transformation, the peaks identify the frequency of the microparticles. With the known length of the slit spacing and the microparticle frequency, the velocity is obtained for flow characterization.

This method was tested for FEFC flow measurements. A masking grid was superimposed onto the recorded flow video to act as the periodic array of slits. The Fourier transformation of the video did not result in a distinct frequency peak for the velocity measurements. Instead, large scatter was observed yielding

Figure 5.2: Microchannel with microparticles under an excitation of 465-495 nm.

inconclusive measurements.

5.1.4 Micro-Particle Image Velocimetry

A promising flow imaging method using fluorescent microparticles is particle imaging velocimetry (micro-PIV) [114, 115]. Video imaging of the flow is used to record the displacement of the microparticles within a known time interval to obtain the velocity fields in a microchannel. This technique can measure planar flow fields [23, 114, 115, 116, 117] and 3D flow fields [118, 119]. Moreover, micro-PIV of the Brownian motion of nanometer diameter microparticles is a method to measure the temperature in a microchannel [120].

Previous researchers used micro-PIV methods to measure the EOF in a microchannel. Due to the electrophoresis of surface charge of the microparticles, the electrophoretic component of the velocity was subtracted out to isolate the EOF [116, 117]. For FEFC testing, fluorescent polystyrene microparticles flowed in the microchannel under EOF and a sample image, with velocity vectors, is shown in Figure 5.2. The polystyrene microparticles were treated with $Fe(NH_4)_2(SO_4)_2{\cdot}6H_2O$ to neutralize their surface charge. The iron ammonium sulfate solution binds to the sulfate groups (SO_4^-) of the microparticles, which are residual from the manufacturer's fabrication process.

The iron ammonium sulfate treatment was successful in neutralizing the elec-

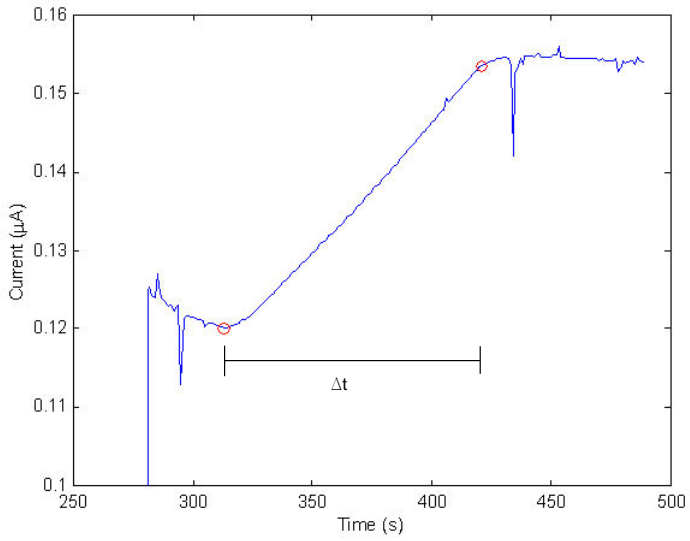

Figure 5.3: Current monitoring in a straight microchannel with fluorescent microparticles.

trophoretic charge of the microparticles. To verify their neutrality, current monitoring was performed simultaneously in a single microchannel with visual recording of the microparticle flow (Figure 5.2). The current monitoring yielded an electroosmotic mobility of 3.27 μm·cm/(V·s) as seen in Figure 5.3. The recorded mobility of the microparticle from the video was 3.29 μm·cm/(V·s), which demonstrates the suppression of the microparticle's electrophoretic flow. The current monitoring test confirmed that the velocity of the neutralized microparticle is only due to EOF and pressure. With this technique developed, the characterization of flow in microchannel networks could be effectively studied.

To measure the velocity of the individual microparticles, their displacements between subsequent video frames were measured in MATLAB's image processing toolbox. Standard PIV techniques use a cross correlation algorithm to extract velocity vectors. Although the standard PIV method reduces data analysis time,

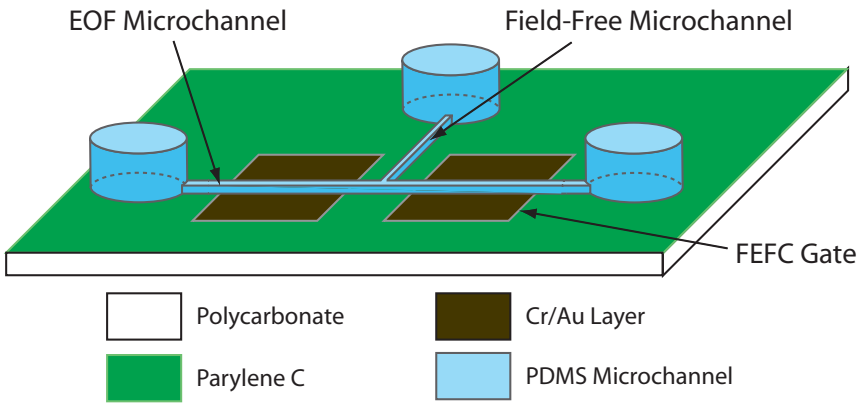

Figure 5.4: Schematic of the T-intersection polymer microfluidic network.

individual particle tracking was performed in order to extract the maximum velocity measurements from the low density bead flow. Each frame was loaded into MATLAB for the displacement measurements. The center position for each microparticle was obtained with a Sobel edge detection subroutine and the microparticle displacement between frames was measured.

5.2 FEFC in a Polymer T-Intersection Microfluidic Network

To demonstrate the utility of FEFC, the gate electrodes were integrated into a polymer microchannel network with a T-intersection [121, 122]. FEFC was used to modulate the zeta potential in two microchannels for dynamic control of the EOF pumping rates. A third, field-free microchannel was connected to the two FEFC microchannels at the T-intersection. The different EOF pumping rates induced pressure pumping in the field-free microchannel. The microfluidic network device is shown in Figure 5.4. The gate voltages, under constant EOF, were varied to study the resulting flow in the field-free microchannel.

5.2.1 Fabrication

The FEFC gate electrodes were built on polycarbonate substrates (Makrolon, Sheffield Plastics Inc., Sheffield, MA). The plastic wafers were placed in an e-beam evaporator for metal deposition. The chromium layer was first evaporated onto the polycarbonate substrate to a 200 Å thickness to be the adhesion layer for the next metal layer. The second layer was gold, deposited to a 3500 Å thickness. The metal layers were patterned with AZ5214 (Clariant, Somerville, NJ) and the exposed metal areas were removed with Au and Cr etchant (Transene, Danvers, MA). The thickness of the metal layers is sufficient to protect the underlying polycarbonate from the solvents in the photoresist [100]. Parylene C was deposited to a thickness of 1.8 μm on the entire wafer surface at NASA Goddard Space Flight Center (Greenbelt, MD).

The master mold for the microchannel network was fabricated on a bulk etched 100 mm silicon wafer (Silicon Quest Intl., Santa Clara, CA) with 2 μm of silicon dioxide. After patterning with photolithography, the silicon dioxide was etched with 5:1 buffered oxide etchant (J.T Baker, Phillipsburg, NJ) and the underlying bulk silicon was etched in preferential silicon etchant (Transene, Danvers, MA) at 60°C. The microchannels were molded from PDMS (Sylgard 184, Dow Corning, Midland, MI) poured onto the silicon wafer master. After curing the PDMS for 2 hours at 60°C in a convection oven, the entrance to the microchannels were opened with 2 mm diameter holes punched into the PDMS for the reservoirs. The cross-section of all the PDMS microchannels were 45 μm in height, with widths varying from 100 μm (top) to 165 μm (bottom) due to the angled sidewall geometry of the silicon master mold.

Placing the PDMS microchannels and polycarbonate substrate into contact

finished the assembly of the device. The reversible adhesion of the PDMS layer enabled devices to be taken apart and washed between tests. During assembly, the T-intersection in the PDMS microchannels were aligned to bisect the distance between the FEFC gates. The network was filled with buffer solution in all three microchannels.

5.2.2 Induced Pressure Pumping

Electrodes were placed in the fluid reservoirs at the ends of the EOF microchannels to generate the longitudinal electric field for EOF. The fluid reservoir at the end of the third microchannel was left at a floating potential so that the microchannel was field-free. Without a bias voltage at the fluid reservoir, EOF pumping was absent in this microchannel. Gate electrodes underneath the EOF microchannels locally controlled the zeta potential. Differential EOF pumping resulted when the FEFC gates were biased with different voltages for unequal zeta potentials. The differential EOF from the positive and negative gate voltages is shown in Figure 5.5.

Differential EOF Pumping

In a similar manner as the T-intersection microfluidic network, static methods to achieve differential EOF and quasi-independent flow control have been demonstrated with surface coatings on glass [21, 22] and plastic [23, 48, 49] substrates. The surface coatings change the zeta potential in the microchannel and establish an EOF pumping rate that is different from the uncoated microchannels. At the intersection of the coated and uncoated microchannels, the sum of the flow rates balance due to the conservation of mass principle. Accordingly, the different EOF

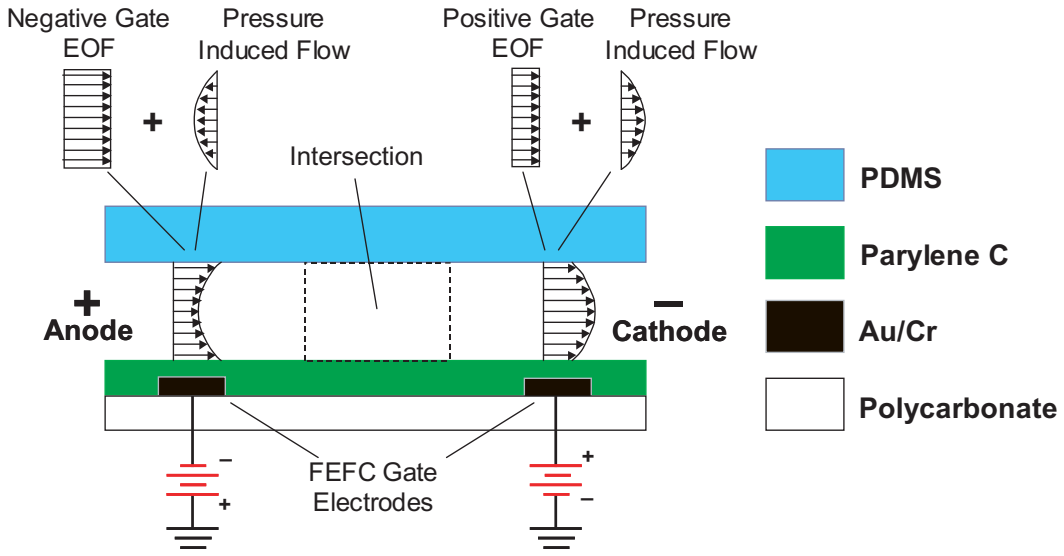

Figure 5.5: Cross-section schematic of the FEFC gate electrodes in a T-intersection microchannel network. The field-free microchannel is shown between the gate electrodes [121, 122].

rates induce a pressure flow in the microchannels to maintain continuity of the flow rates. The induced pressure pumping was applied to generate hydrodynamic pumping in a field-free microchannel [21, 22, 23]. As with the T-intersection microfluidic network, the fluid reservoir at the end of this microchannel was left at a floating potential for no EOF electric field.

Induced pressure was also demonstrated in capillaries. The technique of unequal zeta potentials for induced pressure was applied to capillaries with different buffer concentrations [54] and with surface coatings [78]. In a capillary with two unequal zeta potential regions due to different buffer concentration, induced pressure was generated at the interface of the two buffer solutions to balance the electroosmotic pumping rates [54]. A capillary with a surface coating that suppressed the zeta potential ($\zeta = 0$) was placed in union with an uncoated capillary

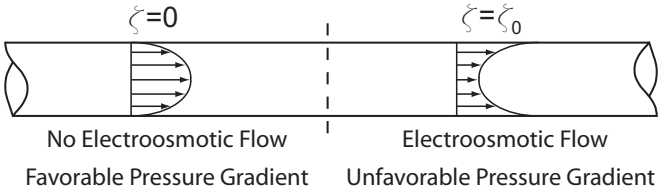

Figure 5.6: Schematic of flow profiles in joined capillaries.

[78] (Figure 5.6). In this configuration, one capillary had electroosmotic pumping and the other did not. However, to balance the two flow rates in the joined capillaries, the induced pressure generated pumping in the coated capillary.

Visualization experiments of caged fluorescent dye in the joined capillaries confirmed that two types of parabolic flow profiles existed in the capillaries - positive and inverted. The coated capillary exhibited a positive parabolic flow profile, as shown in Figure 5.6 due to the favorable pressure gradient from the negative induced pressure at the capillary union. In the capillary with EOF, the induced pressure creates an unfavorable pressure gradient and superimposed an inverted parabolic flow profile on the EOF. Despite the different flow profiles, the average flow rate is equal in both sections to preserve continuity. In a microfluidic network, similar velocity profiles results were obtained with finite element modeling of a T-channel intersection with differential zeta potentials [123, 124].

T-Intersection Pressure Pumping

A representation of the induced velocity profiles from zeta potentials due to FEFC are shown in Figure 5.5 and Figure 5.7. In the cross-sectional view of the microfluidic network in Figure 5.5, a negative gate voltage in the anodic microchannel increases the EOF. Likewise, a positive gate voltage in the cathodic microchannel creates decreased EOF. Due to the conservation of mass flow, the

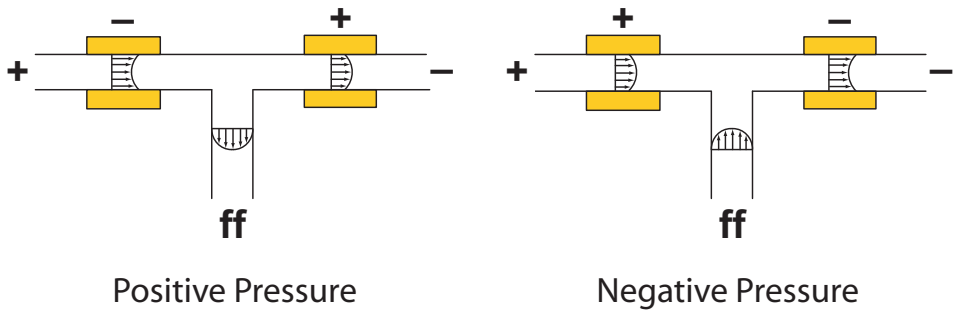

Figure 5.7: Diagram of induced pressure flow in the T-intersection microchannel network [121].

flow rates between the three microchannels must balance. Thus, pressure is induced at the microchannel intersection. The unfavorable pressure gradient in the anodic microchannel combines with the increased EOF flow to create an inverted parabolic flow profile. Similarly, the favorable gradient in the cathodic microchannel creates a parabolic flow profile. Consequently, the induced pressure at the T-intersection generates pumping down the field-free microchannel.

Figure 5.7 shows a top-view schematic of the positive pressure generated under positve and negative gate voltages in Figure 5.5. The flow in the field-free microchannel results from the induced pressure at the T-intersection. For this reason, it has a positive flow profile, without an EOF component. Also shown in Figure 5.7 are the flow profiles for negative induced pressure. This condition occurs when the gate voltages are reversed, so that the anodic microchannel has lower EOF flow than the cathodic. The resulting flow in the field-free microchannel pumps the bulk fluid from the reservoir towards the intersection. Moreover, the flow in the field-free microchannel maintains the positive parabolic flow profile as for positive pressure.

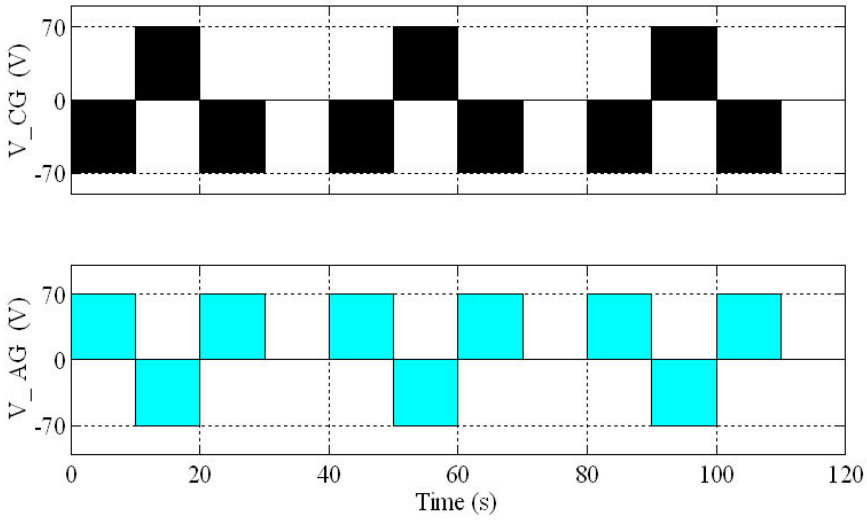

Figure 5.8: Voltage sequence applied to the anodic gate (V_{AG}) and cathodic gate (V_{CG}) [121].

5.2.3 Experimental Proceedure

Two power supplies were used to apply the EOF electric field and three power supplies were used for the two FEFC gate electrodes. Control of the power supplies was performed with Labview (National Instruments, Austin, TX), a PCI-6711 multiplexer card (National Instruments) and two MR62-6S relays (NEC Tokin, Seoul, Korea). The bias voltages of the FEFC gate electrodes were switched at 10 second intervals between three voltage configurations (see Figure 5.8): positive V_{AG} and negative V_{CG} for negative pressure at the T-intersection (+/-), negative V_{AG} and positive V_{CG} for positive pressure (-/+), and zero voltage at both gates for zero pressure (off). The voltage switching allowed for the study of positive and negative pressure flow in the field-free microchannel over a range of gate voltages (±90 V, ±70 V, ±50 V, and 0 V).

Microparticle Treatment

Acetic buffer solutions for the visualization experiments were prepared to 2 mM concentrations at pH 3.8. To reduce the surface charge of the microparticles for visualization measurements, polystyrene Fluorobrite microparticles (2.0 μm diameter, Polysciences, Warrington, PA) were treated for 12 hours in 25 mM $Fe(NH_4)_2(SO_4)_2 \cdot 6H_2O$. The microparticles were filtered from the Fe-solution with a syringe filter (0.45 μm MCE Filter, Fisher Scientific), rinsed with deionized water, and extracted into the acetic buffer solution to be used for the flow visualization experiments.

Micro-PIV Proceedure

The flow of fluorescent microparticles was recorded in the microchannel network for velocity measurement of the combined EOF and pressure induced pumping. The image recording was performed on a Nikon TE-2100-S fluorescent inverted microscope (Nikon, USA) using a B-2E/C FITC filter (excitation 465-495 nm, emission 515-555 nm). A 640x480 pixel CCD camera (DKF-4303, The Imaging Source, Charlotte, NC) was used to record the flow of the microparticles in the microchannel at 30 fps. Post-processing of the velocity measurements was performed with the aid of the Image Processing Toolbox in MATLAB (The Mathworks, Natick, MA). A Sobel edge detection method was used to determine boundary pixels of each of the microparticles. The position of the center pixel for each of the microparticles was measured every ten image frames, which corresponded to a 0.33 second time interval. A scale conversion of 0.75 μm/pixel was used to measure the position of the microparticles in each frame. The velocity for each voltage configuration of the FEFC gate electrodes was determined with

a best-fit slope line through the position measurements.

5.2.4 Characterization of the Induced Pressure Pumping

The induced pressure pumping was studied in a microchannel network consisting of three microchannels at a T-intersection as shown in Figure 5.5. The microchannel length between anodic and cathodic reservoirs was 1.83 cm and the length of the field-free microchannel was 0.54 cm. Two independent FEFC gate electrodes, each with length of 2 mm and a distance of 1.5 mm from the T-intersection, were used to modify the zeta potential in the anodic and cathodic microchannels. The field-free microchannel did not have a FEFC gate electrode since its reservoir was kept at a floating potential. The EOF electric field was held constant at 30.1 V/cm for all tests. The microchannels were filled with buffer solution and the neutralized fluorescent microparticles were injected into the anodic reservoir. The voltage control sequence loop of the FEFC gate voltages was initiated in LABVIEW and the sequence of potentials is illustrated in Figure 5.8 for gate voltages of 70 V. The generation of negative or positive induced pressure was instantaneous to the change in applied FEFC gate voltage. The change occurred faster than the frame speed of the CCD camera (30 fps).

Visualization of Pressure Pumping at the T-Intersection

Flow video taken at the T-intersection show the induced pressure pumping (Figure 5.9). In the field-free microchannel, the microparticles flowed away from the intersection due to a positive induced pressure at the intersection. The gate voltage in the anodic microchannel produced a higher pumping rate than that in the cathodic to develop positive pressure at the intersection. At t = 45 seconds,

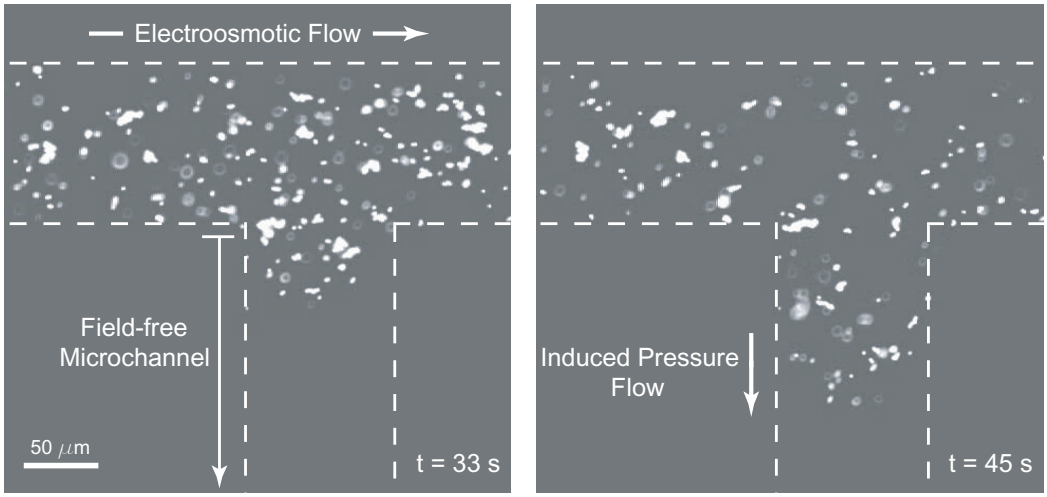

Figure 5.9: Image sequence of induced pressure flow in the field free microchannel [125]. The left side is the anodic microchannel and the right side is the cathodic microchannel.

the microparticles flowing to down the field-free microchannel distinctly shows a parabolic flow profile as they proceed towards the field-free reservoir. The profile is due to the pressure-driven pumping in the field-free microchannel, without the presence of EOF. Likewise, the microparticles in the field-free microchannel flowed toward the intersection when the cathodic gate voltage was greater than that of the anodic due to a negative induced pressure.

Bi-directional Flow

The plot of average velocity and microparticle position measurements over time in Figure 5.10 illustrates the bi-directional switching of the field-free flow rate for a test conducted at V_{AG} = +70 V and V_{CG} = -70 V applied to the FEFC gates. The position measurements over time obtained from micro-PIV are shown with a dashed line. The average velocity measurements are determined

from the slope of the best-fit line through the position data. Across the top of the graph is the corresponding gate voltage configuration that produced the positive or negative field-free pumping.

The results for the tests show that the flow in the field-free microchannel could be switched with repeatability in flow rates between voltage configurations. With zero gate voltages applied to the FEFC gate electrodes, the microparticles exhibited negligible flow in the field-free microchannel due to the lack of induced pressure, as expected for equal EOF pumping rates. The corresponding maximum velocity in the field-free microchannel was 2.4 μm/s, although higher rates were achieved by using larger gate bias voltages ($\pm$90 V).

Sample images of the microparticle tracking data in Figure 5.10 are shown in Figure 5.11. At 50 seconds, the FEFC gates are set to produce positive pressure in the field-free microchannel (frame a). Ten seconds later, the gate voltages are switched to produce negative pressure and the microparticle flows back towards the T-intersection (frame b). The microparticle returned to approximately the same position in the field-free microchannel under the negative pressure pumping. At 70 seconds, the gate voltages are switched off. The flow in the field-free microchannel stopped and the microparticle remained stationary because the zeta potentials in the EOF microchannel were equal. Then, ten seconds later, the FEFC gates are turned back on for positive pressure and the microparticle resumes its flow down the field-free microchannel. The repeatability of the microparticle position and ultra-low flow control is promising for non-mechanical, non-peristaltic pumping in the field-free microchannel.

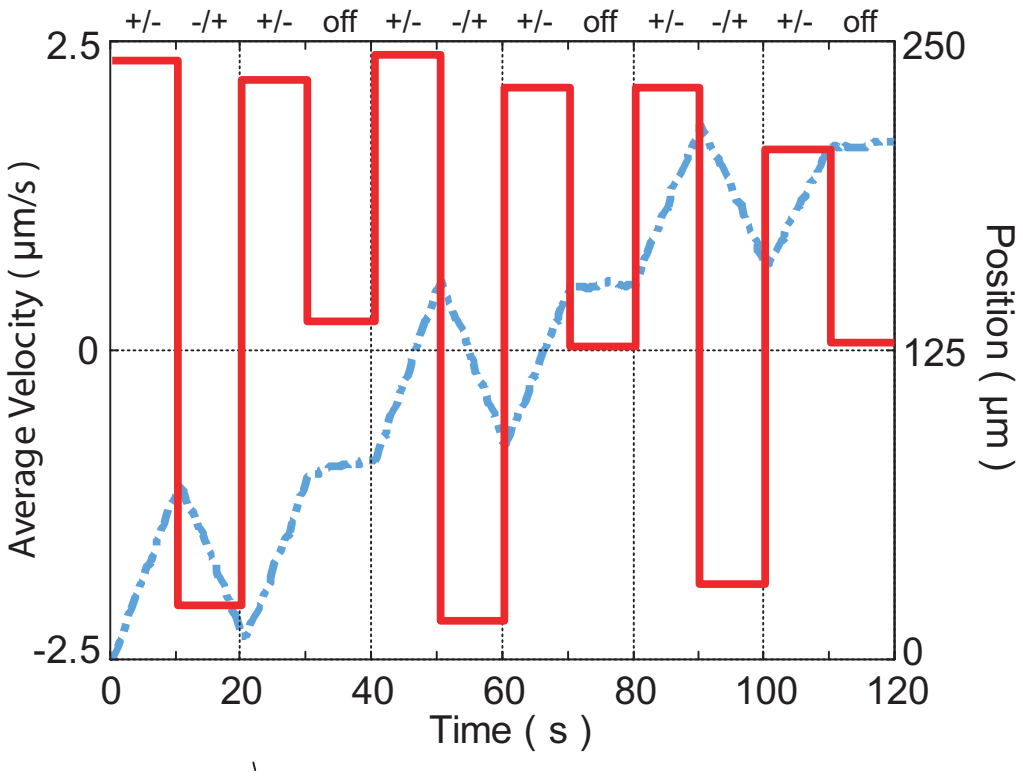

Figure 5.10: Microparticle measurements from induced pressure pumping in the field-free microchannel of the average velocity (solid line) and the microparticle position (dashed line) for gate voltages of ± 70 V (V_{AG}/V_{CG}) [121, 122].

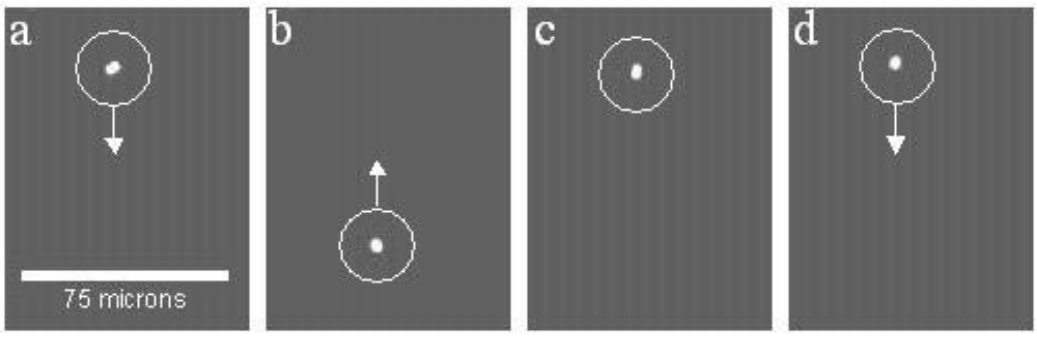

Figure 5.11: Particle images in the field-free microchannel for data in Figure 5.10 at times a) 50, b) 60, c) 70, and d) 80 sec [121].

Differential EOF

To illustrate the changes in the flow rates between the anodic and cathodic microchannels due to FEFC, the velocity of a microparticle that flowed past the T-intersection is plotted in Figure 5.12. The position of the microparticle in the microchannel is labeled across the top of the graph. As shown in the figure, the microparticle started in the anodic microchannel and flowed across to the cathodic microchannel. The induced pressure was not strong enough to divert the microparticle down the field-free microchannel as it crossed the T-intersection.

From 0 to 8.3 seconds, the FEFC gates were set to V_{AG} = -90 V and V_{CG} = +90 V to generate positive pressure at the T-intersection. Due to the increased EOF pumping rate, the velocity of the microparticle was 79±4 μm/s as it flowed through the anodic microchannel ($0 \leq t \leq 4$ s). The microparticle then flowed across the 100 μm wide T-intersection region ($4 \leq t \leq 6$ s), which caused its velocity to decrease to 55 μm/s due the flow down the field-free microchannel. Once the microparticle left the intersection region, the velocity increased to 65±1 μm/s. The new velocity was lower than in the anodic microchannel due to the lower EOF pumping rate in the cathodic microchannel. At 8.3 sec, the gate voltages were switched to generate negative pressure at the intersection. The cathodic gate voltage was set to V_{CG} = -90 V for increased EOF pumping. The change in EOF pumping increased the microparticle's total velocity to 71±2 μm/s.

No Presence of Dielectric Breakdown

Figure 5.13 shows a sequence of images taken at the T-intersection of two microparticles. In frames a-c, the gate voltages were configured to produce pos-

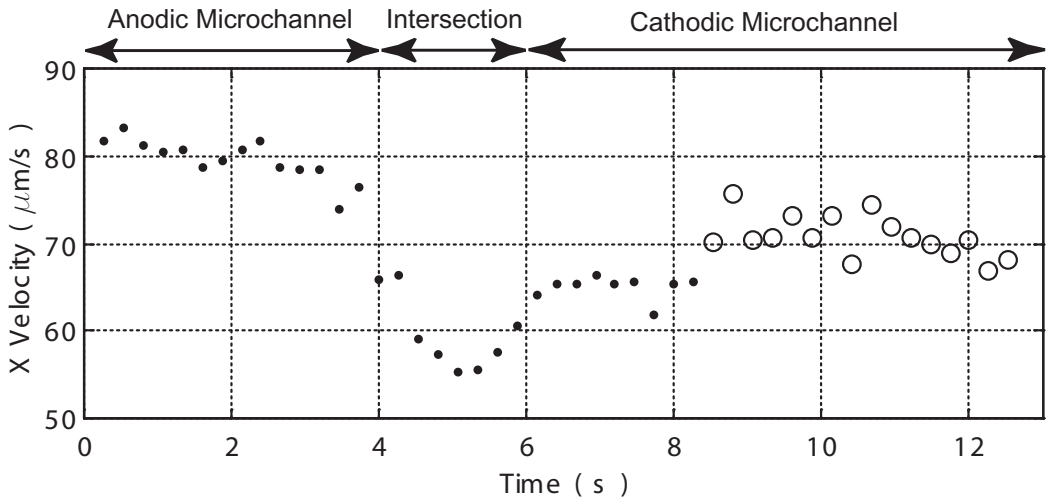

Figure 5.12: Velocity of microparticle flow across the T-intersection. The FEFC gates were initially set for positive pressure (closed circle •). At t = 8.3 sec the gate voltages were switched for negative pressure (open circle ○).

itive pressure at the T-intersection. The top microparticle was in the anodic microchannel and continued toward the cathode. The bottom microparticle in the field-free microchannel changed flow direction when the FEFC gate voltages were switched from positive pressure to negative pressure (frame d). The microparticle continued to flow toward the T-intersection under negative induced pressure (frame e-f).

The sequence of images in Figure 5.13 show that the field-free pumping is not a result of dielectric breakdown of the Parylene C microchannel wall, since the top microparticle continues along toward the cathode under both gate voltage configurations. If dielectric breakdown had occurred, then the additional electric field between the gate electrodes would be greater than the EOF electric field between the reservoirs. To elaborate, the applied gate voltages are larger than the voltages at the reservoirs (±30 V). Also, the distance between the gate electrodes

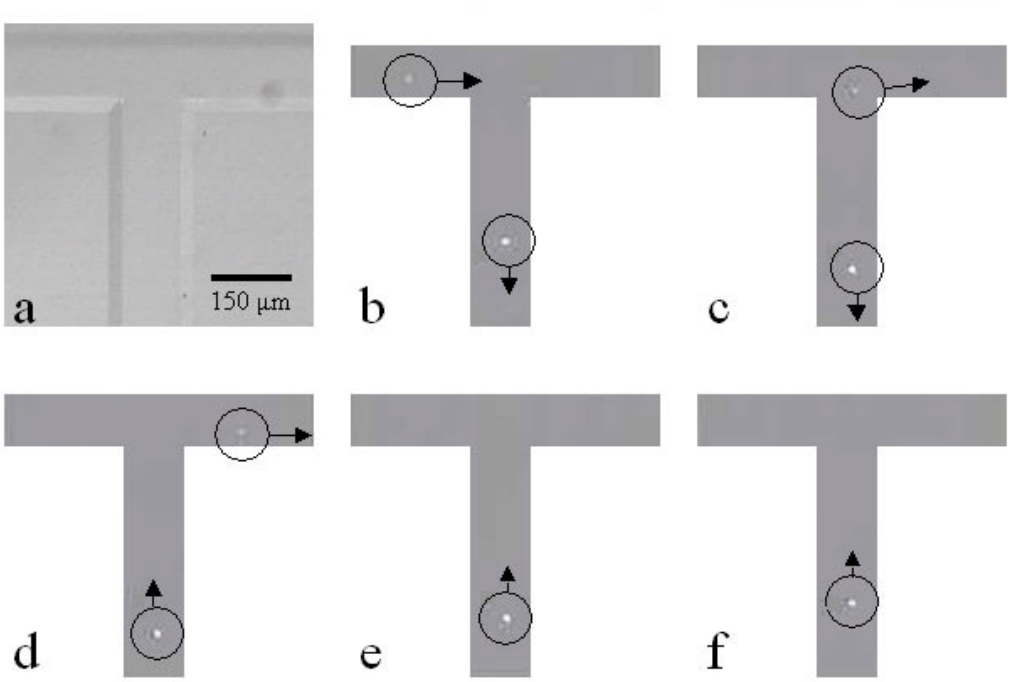

Figure 5.13: FEFC gate voltages of V_{AG} = -90 V and V_{CG} = +90 V initially produced flow down the field-free microchannel as seen in the first row of images (a-c). At 13.9 sec, the voltages were switched to V_{AG} = +90 V and V_{AG} = -90 V and created flow up the field-free microchannel as seen in images d-f [121, 122].

is shorter than the distance between the reservoirs. Therefore, if breakdown occurred in frame d, there would be a strong electric field from the cathodic gate to the anodic gate so that the EOF would flow in the opposite direction in both EOF microchannels. However, the top microparticle does not change direction. Flow reversal was not observed in the EOF microchannels during switching of the FEFC gates for all tests. The absence of flow reversal confirmed that the gate electrodes influence only the zeta potential and not the EOF electric field.

Field-free Pumping versus Gate Voltage

The average velocity in the field-free microchannel was found to be linearly dependent on the difference between the gate voltages (Figure 5.14). Using the voltage control sequence loop, the induced pressure pumping was characterized for three, equal but opposite, gate voltage pairs ($\pm$90 V, $\pm$70 V, and $\pm$50 V) that were applied to the FEFC gate electrodes. The average flow rates from the tests are plotted in Figure 5.14 along with a best-fit line, which highlights the linearity of the results. The maximum flow rate in the field-free microchannel is approximately 20% of the flow rate in the anodic microchannel, which shows low flow switching efficiency. For ideal microfluidic networks, the flow in the anodic microchannel would be diverted 100% into the field-free microchannel. However, the flow control could be improved with different microchannel dimensions and lower inherent zeta potentials (section 6.2).

During the tests, a small inherent pressure difference existed between the field-free reservoir and the intersection, which resulted in a measurable microbead velocity of the microbeads in the field-free microchannel for equal FEFC gate voltages. This is displayed in the graph as a small negative pumping rate for

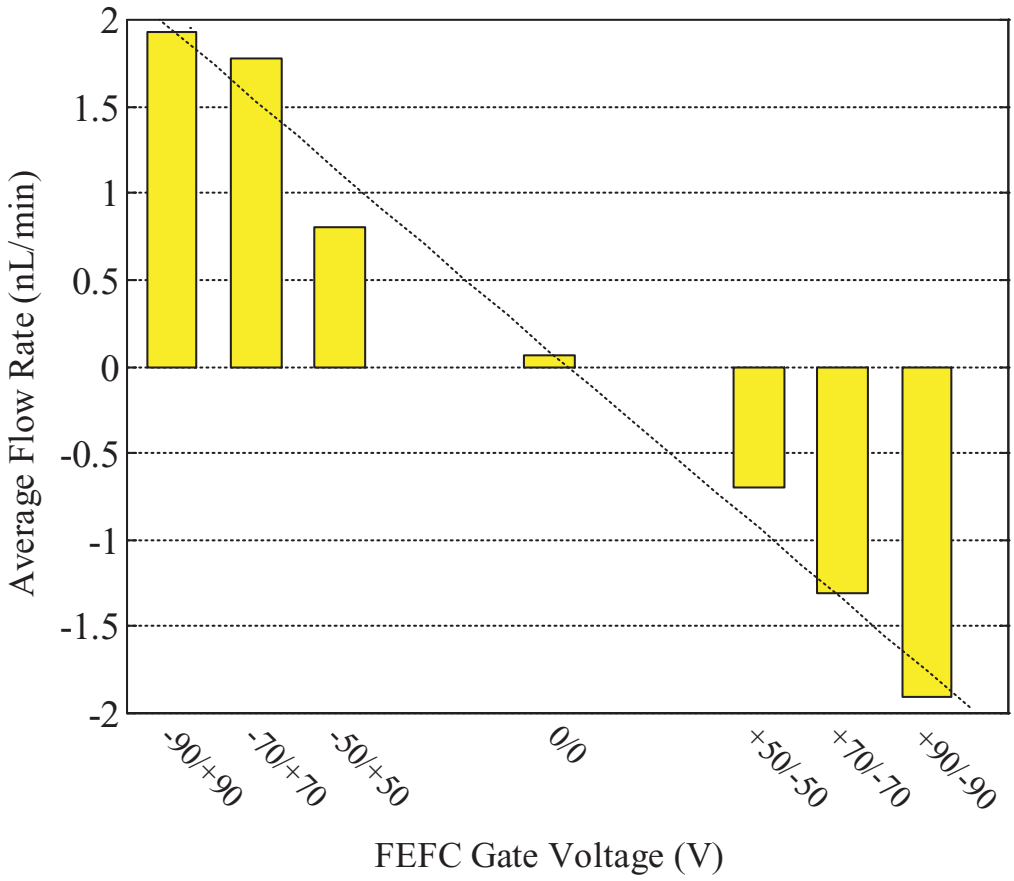

Figure 5.14: Average flow rate in the field-free microchannel versus FEFC gate voltage configuration (V_{AG}/V_{CG}). Negative flow is towards the T-intersection [121, 122].

equal gate voltages (0/0 V). For all tests, the induced pressure from the FEFC gate voltages was sufficient to counteract this flow and thus changing the velocity of the microbeads.

For characterization of the field-free microchannel flow, the trapezoidal sidewalls were modeled as rectangular. The flow rate for incompressible, steady flow in a rectangular cross-section due to pressure pumping [59] is

$$Q = \frac{4ba^3}{4\eta}\left(-\frac{\partial p}{\partial x}\right)\left[1 - \frac{192a}{\pi^5 b}\sum_{i=1,3,5,\ldots}^{\infty}\frac{\tanh\left(i\pi b/2a\right)}{i^5}\right] \tag{5.1}$$

where $2a$ is the distance between sidewalls, $2b$ is the distance between top and bottom walls, and $\partial p/\partial x$ is the pressure gradient. For a positive induced pressure at the T-intersection, the pressure gradient along the field-free microchannel is negative, which cancels with the negative sign in the coefficient to produce positive mass flow to the field-free reservoir. The flow rate equation suggests a linear relationship between the flow in the microchannel and the induced pressure at the T-intersection. Therefore, the induced pressure is linearly dependent on the difference in the applied gate voltages.

Solving for the pressure gradient in equations 5.1, the maximum negative and positive pressure gradients for the experimental flow rates is -36.0 Pa/m and 36.1 Pa/m. Thus, the pressure induced at the T-intersection is between -194 mPa to 195 mPa for the 0.54 cm long field-free microchannel. The induced pressure is extremely small and results in the ultra-low flow rates in the field-free microchannel.

An application for the ultra-low flow rates produced in the field-free microchannel is electrospray, a versatile ionization technique used with mass spectrometry. This pair of delivery and detection methods provide an analytical technique that is used to identify unknown compounds, to quantify known mate-

rials, and to elucidate the structural and chemical properties of molecules. The ability to analyze intact proteins, protein mixtures, or low protein concentrations makes electrospray mass spectrometry an indispensible tool for proteomics [126, 127]. In electrospray, charged liquid droplets are formed from solutions at high voltages and sprayed from a needle or microchannel to the entrance of the mass spectrometer. The liquid droplets contain the analyte molecules so that increasing the surface to volume ratio of the droplet enables ultra-low analyte detection. To reduce the droplet volume, the diameters have been shown to be proportional to 2/3 power of the flow rate [126]. As a result, nanoliter per minute flow rates produce droplets that are sufficient for femtomole or attomole detection sensitivty at the mass spectrometer [126, 127, 128, 129]. Additionally, the ultra low flow rates enable longer measurement time at unchanged signal levels for longer signal averaging.

The next section explores the effect of reducing the length of the field-free microchannel to improve the induced pressure gradient. The technique of induced pressure via FEFC gates enables a non-mechanical, non-peristaltic means of pressure pumping. The induced pressure can be employed to adjust the total flow rate from EOF without the need to adjust the reservoir voltages. Moreover, the pressure can be induced at any intersection in an M×N microfluidic network with independent FEFC gates. Thus, if the network is input-limited, then the internal pressure can be used to adjust the total flow at any internal microchannel within the network.

5.3 FEFC in a 3D Microfluidic Network

In addition to controlling the flow in a planar microfluidic device, the control over the flow can be extended into the third dimension. For the increasing complexity of LOC devices, a high density of separation microchannels, flow mixing components, addressible chemical reactors, and detection sensors are required to improve their high-throughput performance [8]. Thus, complex systems of microchannels require a higher degree of connectivity between the microchannels than can be generated with simple, planar LOC devices [33]. The need for an increased density of components has led to the development of 3D microfluidic systems [8, 33, 34], in which multiple levels of planar microchannel networks are interconnected with short, 3rd dimensional microchannels. With these complex systems, flow control in the 3rd dimension is necessary to enable a high degree of multiplexing of the sample analysis.

In order to address flow control in the 3rd dimension, an all-polymer 3D microchannel microfluidic network [130] was developed in collaboration with Calibrant Biosystems, Inc. (Rockville, MD) using FEFC technology described in Section 5.2. The 3D network used two layers of PDMS molded microchannels on a Parylene C coated silicon wafer. A short microchannel in the 3rd dimension connected the microchannels in the layers. A schematic of the microdevice is shown in Figure 5.15 to illustrate the two layers of PDMS. The results presented in this section were produced by Dr. Ponniah Sivanesan (Calibrant Biosystems, Inc.) in close consultation with the present author and are offered here to provide a view of another potential application of all-polymer FEFC. Additionally, the results are summarized here for comparison with the matrix-form model in Chapter 6. The 3D microfluidic network was designed with a field-free microchannel

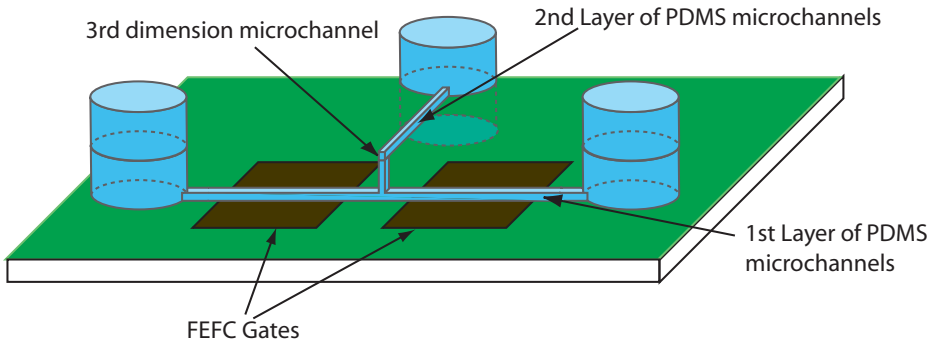

Figure 5.15: 3D microfluidic network.

in the 2nd PDMS layer. The length of the field-free microchannel was varied in order to study its effect on the induced pressure pumping.

5.3.1 Fabrication

The gate electrodes were fabricated on a silicon wafer with a 200 Å layer of Cr and a 1500 Å layer of Au deposited onto the wafer surface with e-beam deposition. After patterning the electrodes, the wafer was coated with 1.2 μm of Parylene C (Specialty Coating Systems, Indianapolis, IN). The first layer of the PDMS microchannels was formed from a master mold that used a two layer lithographic process with SU-8 photoresist (MicroChem Corp., Newton, MA). The first layer mold produced the anodic and cathodic microchannels and the 3rd dimensional microchannel. The second layer of the PDMS microchannels was formed from a single layer of SU-8 to form the field-free microchannel and reservoirs. The application of SU-8, a thick negative photoresist, enables the creation of a master mold with rectangular cross-sections for the microchannels. An SEM image of the SU-8 mold for the first layer of PDMS is shown in Figure 5.16. The 3rd dimension microchannel was 120 μm in width and 100 μm in

height. The microchannels in both the first layer and second layer were 100 μm wide and 40 μm high.

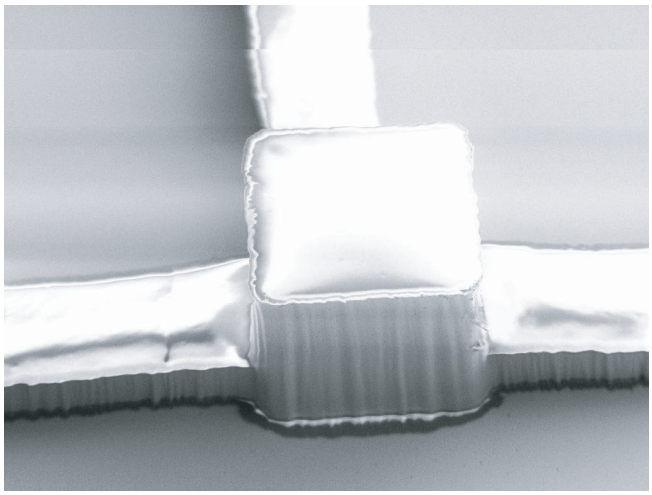

Figure 5.16: SEM of the SU-8 master mold for the 1st PDMS layer (*courtesy of Dr. Ponniah Sivanesan*)[130].

5.3.2 Micro-PIV Testing

The operation of the device is similar to that described for the T-intersection microfluidic network. The longitudinal electric field was $E = 26$ V/cm and the applied gate voltages was equal but opposite for V_{AG} and V_{CG} throughout the study. The different gate voltages created a differential EOF pumping rate that resulted in induced pressure pumping in the 3rd dimension microchannel and the field-free microchannel in the 2nd layer of PDMS.

Non-fluorescent microparticles with 2 μm diameters were neutralized in an ammonium ferrous sulfate solution as described in Section 5.1.4. The velocity of the beads was recorded with a CCD camera (The Imaging Source, Charlotte, NC) on a probe-station (RF-1, Cascade Microtech, Inc., Beaverton, OR) under visible

light. The average velocity of the microparticles in the field-free microchannel was measured from the position of microparticles in a set of three frames from the video at 2 second intervals.

5.3.3 Experimental Results

The pressure induced flow velocities in the field-free microchannel were characterized with different pumping parameters: the width of the gate electrodes, the distance between the electrodes, and the field-free microchannel length. Table 5.1 lists the values studied of each of these lengths. The flow velocity represents a mean value of at least 75 velocity measurements.

Gate Voltage (V)	Electrode Width (mm)	Electrode Distance (mm)	Field-Free Length (mm)	Average Velocity (μm/s)
100	2	8	5	5.43
100	3	5	2.5	15.28
100	4	4	5	11.13
100	4	4	3	16.75
100	4	4	1	25.04
100	4	4	0.5	29.05
80	4	4	1	20.02
60	4	4	1	14.85

Table 5.1: Summary of 3D FEFC microfluidic network test results [130].

The field-free microchannel length was varied for a constant gate electrode width and distance. The test results showed that the induced pressure pumping

is dependent on the length of the field-free microchannel. In addition, the results for the 1 mm field-free microchannels in Table 5.1 also confirm that the velocity is linearly dependent of the gate voltages applied to the FEFC gates. Due to an oversight in the design of the electrodes, the width and separation of the electrodes could not be studied independently.

5.4 Conclusion

The development of microfluidic networks using FEFC is presented. Due to the limitations of current monitoring in microchannel networks, a flow visualization technique was developed to characterize the flow control. Fluorescent dye or caged fluorescence was not chosen due to inaccurate representation of the EOF pumping. Micro-particle image velocimetry of neutralized fluorescent microparticles was used instead for the flow characterization.

A polymer-based FEFC micropump with a T-intersection was successfully demonstrated and characterized for dynamic control of pressure induced pumping. The pumping mechanism enables fully bi-directional hydrodynamic flow by coupling multiple FEFC gate electrodes in a microchannel network for differential EOF. Pumping rates from approximately -2 to 2 nL/min were readily achieved in the field-free microchannel using differential EOF in the anodic and cathodic microchannels. A linear relationship between the gate voltage and the induced pressure pumping was observed.

The T-intersection microchannel network was expanded into the third dimension for the realization of a 3D microfluidic network. The base layer used FEFC gates on a silicon wafer with a Parylene C coating, combined with a PDMS microchannel fabrication method that used SU-8 for multiple layers of PDMS

microchannels. These layers were connected with a microchannel in the third dimension. With these networks, the length of the field-free microchannel was varied to study its effect on the field-free pumping.

Overall, the FEFC technique does not require adjustment of the reservoir pressure or manipulation of the longitudinal EOF electric fields at the fluid reservoirs nor does it need complex methods to dynamically modify the microchannel surface chemistry. The control over the differential EOF in both networks by means of FEFC makes tunable pumping possible at internal nodes within microfluidic networks, providing dynamic flow control within field-free microchannels.

Chapter 6

Modeling Field-Effect Flow Control in Microfluidic Networks

The previous results in the literature described in Section 5.2.2 have shown that the Smoluchowski model (equation 2.1) does completely express the flow in FEFC microfluidic networks due to the induced pressure pumping. Re-examination of the Navier-Stokes relation (equation 2.6) is necessary for analysis of the flow effects from FEFC. The development of a new model that describes the EOF and pressure pumping can then be used to improve the performance of the FEFC microfluidic network. The matrix-form model presented here closely matches the experimental results, allowing for future optimization of device layouts to minimize fabrication costs and eliminate design iterations. With the matrix-form model, the following trends from the tests with the microfluidic networks can be addressed:

- The bulk pumping rates and induced pressure versus gate voltages.
- Attainability of 100% flow "shut-off" in an EOF microchannel.
- Optimum microchannel dimensions for improved field-free pumping.
- Location of gate electrodes for improved FEFC.

6.1 Analytical Model of FEFC Networks

Previous studies of electroosmotic flow in microchannel networks with dissimilar zeta potentials have been conducted using finite element simulations [123], meshless analysis [131], and compact models [124]. These works are seminal in the development of a model specific to flow in a FEFC system. An approximate analytical model, derived from the Navier-Stokes relation, was conducted for the FEFC system with a T-intersection to develop the relationship between the induced pressure and the FEFC gate voltage. The model solves for the induced pressure gradients in matrix-form.

6.1.1 Navier-Stokes Equation for FEFC Induced Pressure

For thin electric double layers in the microchannel, the description of the fluid mechanics is approximately the Stokes equation. Computer simulations [132] have shown that pressure effects are negligible in the inner flow region. The effect of pressure on the flow inside the electric double layer is small because it increases from zero effect at the plane shear to a value at the plane of slip, which are typically separated in distance on the order of tens of nanometers, that scales with the distance squared. However, as the distance from the wall increases in the outer flow region, the inertial and pressure forces become important so that the flow becomes dependent on time and the pressure gradient. As a result, it is widespread to consider the electroosmotic flow in a microchannel or capillary as a slip velocity condition for thin electric double layers [101, 133, 134, 135]. This approximation uncouples the flow outside the plane of slip from the flow inside, where electrokinetic and viscous forces dominate. Outside the plane of slip, for low Re and negligible pressure gradients, the flow is irrotational and the material

pathlines follow those of the electric field lines [135]. The slip velocity at the plane of slip is equal to the Smoluchowski equation (equation 2.1).

To model the FEFC microfluidic networks, recall the Navier-Stokes relation (equation 2.5), but with non-negligible pressure gradients in the network. Previously in deriving the Smoluchowski equation for EOF, the electrical body force from the longitudinal electric field was used to solve for the effect of the zeta potential on the velocity. For the model, the effect of the longitudinal electric field on the flow is included as a slip boundary condition when solving the Navier-Stokes relation [124]. Recall the classical Navier-Stokes relation from Section 2.2:

$$\frac{\partial \vec{u}}{\partial t} + \vec{u} \cdot \nabla \vec{u} = -\nabla p + F + \eta \nabla^2 \vec{u}$$

For incompressible flow at low Reynolds numbers without a body force, the Navier-Stokes equation reduces to

$$\eta \nabla^2 \vec{u} = \nabla p \tag{6.1}$$

This relation is a balance between the viscous forces and the pressure forces. Integrating equation 6.1 twice for flow between two infinite flat plates separated by height, h, and with slip velocities of u_{eo} at $z = h/2$ and $z = -h/2$ yields

$$u = -\frac{\epsilon \zeta E}{\eta} - \left(\frac{\partial p}{\partial x}\right) \frac{1}{2\eta} \left(z^2 - \frac{h^2}{4}\right) \tag{6.2}$$

It is important to point out that this expression pertains to a different coordinate system (see Figure 6.1) than that used previously to describing pure EOF in section 2.2. Here, the flow is in the x-direction and the velocity is denoted as u.

The first term in equation 6.2 is similar to Couette flow, which is flow driven by a moving flat plate or, more specifically, by a slip velocity boundary condition. Here, there are two slip velocities at both walls and expressed from the

Smoluchowski equation (equation 2.1). The second term is equal to the Poiseuille flow for infinite flat plates due to the pressure gradient along the microchannel ($\partial p/\partial x$). Integrating the combined Couette-Poiseuille type flow in equation 6.2 with respect to z gives the flow rate per unit width:

$$q = -\frac{\epsilon\zeta E}{\eta}h - \left(\frac{\partial p}{\partial x}\right)\frac{h^3}{12\eta} \tag{6.3}$$

The flow rate contains two superimposed components - the EOF flow rate and the induced pressure flow rate - such that the volumetric flow rate can be described as the sum of two components

$$Q_{total} = Q_{electroosmosis} + Q_{pressure}$$

The infinite flat plate does not accurately model the flow in the microfluidic network since it is a planar description. The cross-sectional shapes for the microchannels are either trapezoidal due to the anisotropic etching of the silicon master mold or rectangular due to the SU-8 mold. For approximation, both shapes are considered to be rectangular cross-section. This approximation enables the induced pressure flow rate in equation 6.3 to be replaced with the analytical solution for Poiseuille flow through a rectangular cross-section ($-a \leq y \leq a$, $-b \leq z \leq b$) as listed in White (1991). The velocity distribution is expressed as:

$$u(y,z) = \frac{16a^2}{\mu\pi^3}\left(-\frac{\partial p}{\partial x}\right)\sum_{j=1,3,5,\ldots}^{\infty}(-1)^{(j-1)/2}\left[1-\frac{\cosh(j\pi z/2a)}{\cosh(j\pi b/2a)}\right]\frac{\cos(j\pi y/2a)}{j^3} \tag{6.4}$$

The flow rate, Q, is obtained from integrating the velocity distribution over the area, yielding:

$$Q = \frac{4ba^3}{4\eta}\left(-\frac{\partial p}{\partial x}\right)\left[1-\frac{192a}{\pi^5 b}\sum_{j=1,3,5,\ldots}^{\infty}\frac{\tanh\left(j\pi b/2a\right)}{j^5}\right] \tag{6.5}$$

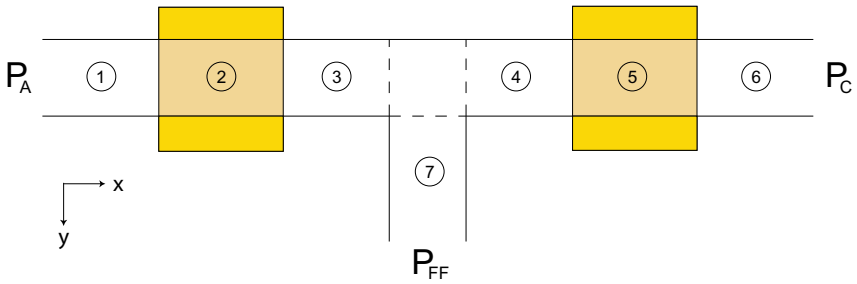

Figure 6.1: Analytical model of the discretized T-intersection. The z-direction is out of the plane.

Combining equation 6.5 with the volumetric flow rate for EOF, the total flow rate through a rectangular cross-section microchannel becomes:

$$Q = -\frac{\epsilon\zeta E}{\eta}(4ab) + \frac{4ba^3}{4\eta}\left(-\frac{\partial p}{\partial x}\right)\left[1 - \frac{192a}{\pi^5 b}\sum_{j=1,3,5,\ldots}^{\infty}\frac{\tanh\left(j\pi b/2a\right)}{j^5}\right] \tag{6.6}$$

where $2a$ is the distance between sidewalls, $2b$ is the distance between top and bottom walls. The flow rate in equation 6.6 is the EOF flow rate superimposed on classical flow rate for Poiseuille flow through a rectangular duct. It is important to point out that the zeta potential is assumed to be equal on the four microchannel walls. For electroosmotic flow with different zeta potentials, the reader should refer to the work of Andreev *et al.* [136] and Bianchi *et al.* [137].

6.1.2 Continuity Principle

The microchannels in the T-intersection microfluidic network contain different slip velocity boundary conditions from changes in the zeta potential due to the FEFC gates. To analyze the flow, the three original microchannels, the anodic, cathodic, and field-free microchannels, are divided into seven sections as shown in Figure 6.1. Discretizing the microchannels allows for different zeta potentials, ζ_i, for each section of the model. With in each section, the zeta potential is

assumed to be uniform on all four walls of the microchannel[1]. The different zeta potentials between sections are due to influence of the tranverse electric fields from the underlying FEFC gates. The modified zeta potential values are obtained from the double capacitor model. Moreover, discretizing allows for the calculation of the different pressure gradients, $(\partial p/\partial x)_i$, in each section. Thus, the expression of equation 6.6 for each section is

$$Q_i = -\frac{\epsilon \zeta_i E}{\eta}(4ab) + \frac{4ba^3}{4\eta}\left(-\frac{\partial p}{\partial x}\right)_i \left[1 - \frac{192a}{\pi^5 b}\sum_{j=1,3,5,\ldots}^{\infty} \frac{\tanh\left(j\pi b/2a\right)}{j^5}\right] \tag{6.7}$$

Since the flow is incompressible, the flow rates between connected sections balance due to the principle of continuity:

$$Q_1 + Q_2 = 0$$
$$Q_2 + Q_3 = 0$$
$$Q_3 + Q_4 + Q_7 = 0$$
$$Q_4 + Q_5 = 0$$
$$Q_5 + Q_6 = 0$$

Since the double capacitor model determines the zeta potentials due to the FEFC, the unknowns that need to be solved for in the model are the seven induced pressure gradients. Applying the continuity principle between all the sections results in five equations, which is insufficient to solve for the seven pressure gradients. Therefore, an assumption about the pressure distribution between the sections is required solve for the pressure gradients.

[1]The zeta potential in the gated section may not be uniform. The transverse electric field may only modify the zeta potential along the bottom microchannel wall, and so this contention is outlined for future work.

6.1.3 Linear Piece-wise Continous Pressure

In order to fully solve for the induced pressure gradients, the continuity equations are coupled with an assumption on the pressure in the microchannel. A valid assumption, used in capillaries with different zeta-potentials, is that the pressure gradient is constant and that the pressure distribution in the capillary is linear, piece-wise continuous [54, 78]. Using the same assumption for the microchannels, the pressure in a section is dependent on the pressure in the adjacent microchannel section:

$$\begin{array}{lcll}
\left(\frac{\partial p}{\partial x}\right)_1 x + & P_A & = p\left(x\right) & \text{for } \ 0 \leq x \leq L_1 \\
\left(\frac{\partial p}{\partial x}\right)_2 x + & p\left(L_1\right) & = p\left(x\right) & \text{for } \ L_1 \leq x \leq L_1 + L_2 \\
\left(\frac{\partial p}{\partial x}\right)_3 x + & p\left(L_1 + L_2\right) & = p\left(x\right) & \text{for } \ L_1 + L_2 \leq x \leq L_1 + L_2 + L_3 \\
\vdots \quad + & \vdots & = \ \vdots & \\
\left(\frac{\partial p}{\partial y}\right)_7 y + p\left(L_1 + L_2 + L_3\right) & & = p\left(y\right) & \text{for } \ 0 \leq y \leq L_7
\end{array}$$

From these relations, two piece-wise continuous equations for the pressure between the reservoirs can be expressed: the pressure distribution between the anodic and cathodic reservoirs and the pressure distribution between the anodic and field-free reservoir. With the five continuity equations, the two pressure equations needed to solve for the induced pressure gradients are

$$\left(\frac{\partial p}{\partial x}\right)_1 L_1 + \left(\frac{\partial p}{\partial x}\right)_2 L_2 + \ldots + \left(\frac{\partial p}{\partial x}\right)_6 L_6 = P_C - P_A \tag{6.8}$$

$$\left(\frac{\partial p}{\partial x}\right)_1 L_1 + \left(\frac{\partial p}{\partial x}\right)_2 L_2 + \left(\frac{\partial p}{\partial x}\right)_3 L_3 + \left(\frac{\partial p}{\partial y}\right)_7 L_7 = P_{FF} - P_A \tag{6.9}$$

6.1.4 Matrix-Form Solution

The goal is to determine the induced pressure gradients due to the different zeta potentials in the microchannel. To accomplish this, the pressure equations

and the continuity equations are written in matrix-form to solve for the induced pressure gradients:

$$\begin{bmatrix} -H & H & 0 & 0 & 0 & 0 & 0 \\ 0 & -H & H & 0 & 0 & 0 & 0 \\ 0 & 0 & -H & H & 0 & 0 & H \\ 0 & 0 & 0 & -H & H & 0 & 0 \\ 0 & 0 & 0 & 0 & -H & H & 0 \\ L_1 & L_2 & L_3 & L_4 & L_5 & L_6 & 0 \\ L_1 & L_2 & L_3 & 0 & 0 & 0 & L_7 \end{bmatrix} \begin{pmatrix} \left(\frac{\partial p}{\partial x}\right)_1 \\ \left(\frac{\partial p}{\partial x}\right)_2 \\ \left(\frac{\partial p}{\partial x}\right)_3 \\ \left(\frac{\partial p}{\partial x}\right)_4 \\ \left(\frac{\partial p}{\partial x}\right)_5 \\ \left(\frac{\partial p}{\partial x}\right)_6 \\ (\partial p/\partial y)_7 \end{pmatrix} = \begin{pmatrix} Q_{eof}\left(\zeta_1 - \zeta_2\right) \\ Q_{eof}\left(\zeta_2 - \zeta_3\right) \\ Q_{eof}\left(\zeta_3 - \zeta_4\right) \\ Q_{eof}\left(\zeta_4 - \zeta_5\right) \\ Q_{eof}\left(\zeta_5 - \zeta_6\right) \\ P_C - P_A \\ P_{FF} - P_A \end{pmatrix} \tag{6.10}$$

where the shape factor for the rectangular cross-section is

$$H = \frac{4ba^3}{4\eta}\left[1 - \frac{192a}{\pi^5 b}\sum_{j=1,3,5,\ldots}^{\infty}\frac{\tanh\left(j\pi b/2a\right)}{j^5}\right]$$

and the EOF flow coefficient for the zeta-potential is

$$Q_{eof} = \frac{\epsilon E\left(4ab\right)}{\eta}$$

For simplification, equation 6.10 can be expressed as:

$$\mathcal{M}\ \ P = Z \tag{6.11}$$

The elements in matrix $\mathcal{M}$ consist of the shape factor, H, and the microchannel section lengths. Since the microchannel dimensions are in micrometers and the section lengths are in millimeters, the order of magnitude difference between H and L_i is on the order of 10^{-16}. This difference in magnitudes could cause $\mathcal{M}$ to be close to singular, depending on the precision of the computation machine[2]. To keep $\mathcal{M}$ nonsingular, the pressure equations could be multiplied by a scaling

[2]MATLAB's machine precision is $\approx 2.2204 \times 10^{-16}$

factor to reduce the difference between H and L_i. Subsequetly, equation 6.11 can easily be solved with Gaussian elimination for the induced pressure gradients:

$$P = \mathcal{M}^{-1} Z \tag{6.12}$$

6.1.5 Fully Developed Flow Assumption

The analytical model assumes that the flow is fully developed. A consequence of this assumption is that the model is not valid for regions wherein the zeta potential changes in value. Therefore, outside the gate regions, there is a transition in the flow. For comparison, consider flow through a straight duct of arbitrary but constant shape. Shah and London [138] showed that there will be an entrance effect of length, L_e, wherein the flow is not yet fully developed. After the entrance length, the flow is purely axial and varies only along the lateral dimensions of the duct, i.e. fully developed. The size of the transition region from a zeta potential discontinuity can be approximated by the relationship Shah and London developed empirically:

$$L_e \approx D_h \left(0.5 + 0.05 \text{ Re}\right) \tag{6.13}$$

where D_h is the equivalent hydraulic diameter of the duct and Re is the Reynolds number of the flow. For the T-intersection microfluidic network, the hydraulic diameter for the trapezoidal microchannel dimensions is

$$D_h = 4A/P = 63.4 \ \mu\text{m}$$

where A is the area and P is the perimeter of the microchannel cross-section. Since flow in the microchannel is on the order of μm per second, Re is extremely small. Table 6.1 lists the expected lengths of the transition regions for a range of

appropriate Re numbers for the flow through the network. Due to the dominance of the viscous forces over the inertial forces, the entrance length is equivalent to approximately half the hydraulic diameter of the microchannel. Thus, the flow in the microfluidic network is predominately fully developed, except for the small regions, which are on the order of micrometers, where the zeta potentials change magnitude.

Velocity (mm/s)	Re	L_e (μm)
100	7.1×10^{-3}	31.9
50	3.6×10^{-3}	31.8
1	7.1×10^{-4}	31.7
0.1	7.1×10^{-5}	31.7

Table 6.1: Entrance length for fully developed flow.

6.2 T-Intersection Microfluidic Network Model

The matrix-form model developed in Section 6.1 is applied to the experimental results of the T-intersection microfluidic network from Chapter 5 for validation of the model. The microchannels in the network are divided into seven sections to solve for the induced pressure gradients. The pressure at the anodic and cathodic reservoirs is set to zero. The pressure at the field-free microchannel is nonzero to model the small field-free pumping when the gate voltages are set to zero. The unmodified zeta potential, $\zeta_{i=1,2,4,6}$, is obtained from the EOF velocity versus gate voltage data in Figure 4.5 on page 66. For disclosure, Table 6.2 lists the values used in performing the matrix-form model.

The double capacitor model was used to determine the modified zeta potential

Property	Value	Property	Value
P_A	0 Pa	d	1.8 μm
P_C	0 Pa	L_1	5.7 mm
P_{FF}	30 mPa	L_2	2.0 mm
$\zeta_{i=1,2,4,6}$	-13.5 mV	L_3	1.5 mm
E	30.1 V/cm	L_4	1.5 mm
a	66.25 μm	L_5	2.0 mm
b	22.5 μm	L_6	5.7 mm
c	2 mM	L_{FF}	5.4 mm

Table 6.2: Dimensional values used in the T-intersection model.

at the two gated regions. For consistency, the potential at the center of each gate was used for the internal potential, V_i, in equation 2.16 on page 26. The internal potential above the two gate regions was not identical, but instead decreased longitudinally due to the EOF electric field, E. Taking the potential above each gate into consideration resulted in different modified zeta potentials when the same voltage was applied to different gates (Table 6.3). For example, when -90 V is applied to the anodic gate (V_{AG}) the resulting zeta potential is -28.2 mV, while for the cathodic gate (V_{CG}) the zeta potential is -26.0 mV. It is important to point out that a gate voltage of zero does induce a small degree of FEFC, due to the internal voltage above the gates as shown in Table 6.3.

Over the range of applied voltages, the anodic gate never achieves a positive zeta potential, which signifies reverse EOF. However, the double capacitor model predicts that the cathodic gate achieves reverse EOF for an applied gate voltage of +90 V. On the contrary, reverse flow was never observed in the T-intersection

V_{AG} (V)	-90	-70	-50	0	+50	+70	+90
ζ_2 (mV)	-28.2	-25.2	-22.3	-15.0	-7.6	-4.7	-1.8
V_{CG} (V)	+90	+70	+50	0	-50	-70	-90
ζ_5 (mV)	0.4	-2.5	-5.4	-12.8	-20.1	-23.0	-26.0

Table 6.3: Zeta potentials from the double capacitor model.

microchannel for the +90 V gate condition. For this reason, the matrix-form model is pertinent to investigate why reverse EOF was not observed.

6.2.1 Flow Rate Results

The matrix-form model was written in MATLAB and computed for the seven paired gate conditions listed in Table 6.3. The $\mathcal{M}$ matrix was sufficiently conditioned to avoid singularity, and so a scaling factor was unnecessary. For all gate configuration simulations, the continuity equation holds, yielding equal pumping rates in connected microchannels (Table 6.4). Moreover, the flow rate in the anodic microchannel ($Q_{1,2,3}$) is equivalent to the sum of the flow rates in the cathodic microchannel ($Q_{4,5,6}$) and the field-free microchannel (Q_{FF}).

V_{AG} (V)	-90	-70	-50	0	+50	+70	+90
V_{CG} (V)	+90	+70	+50	0	-50	-70	-90
$Q_{1,2,3}$ (nL/min)	12.6	12.4	12.1	11.5	10.9	10.6	10.4
$Q_{4,5,6}$ (nL/min)	10.3	10.6	10.8	11.5	12.1	12.3	12.6
Q_{FF} (nL/min)	2.3	1.8	1.3	0.0	-1.2	-1.7	-2.2

Table 6.4: Flow rates in the microchannel sections.

The results for the predicted field-free pumping listed in the last row of Table 6.4 were compared to the experimental data from the micro-PIV experiments in

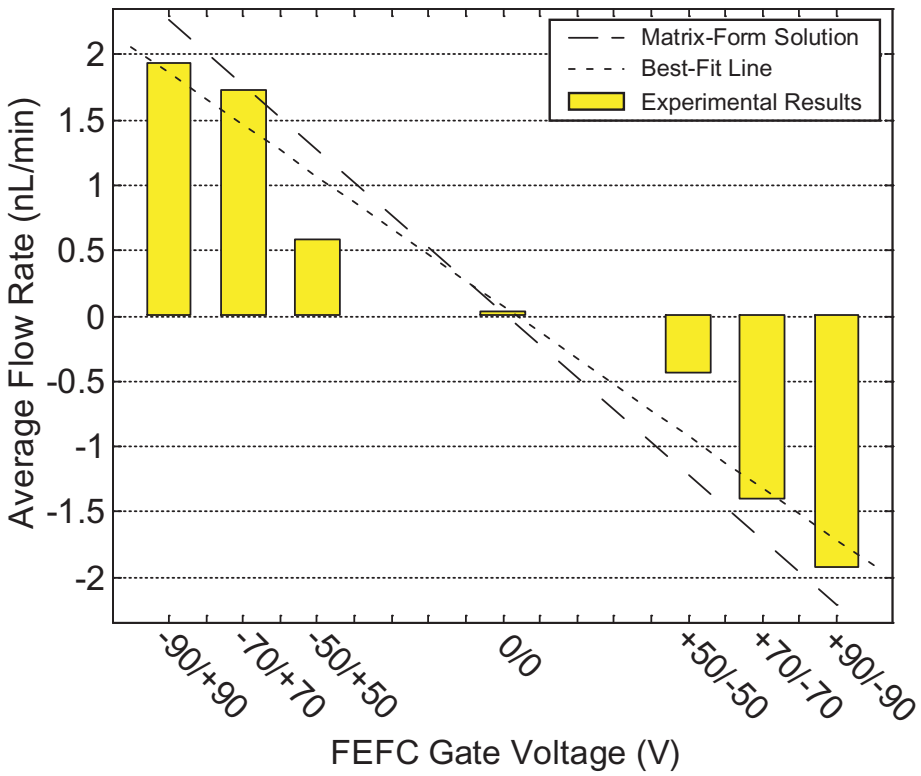

Figure 6.2: Comparison of flow rates between model and experimental results for the T-intersection microfluidic network.

Figure 5.14 on page 96. The comparison is plotted in Figure 6.2. The matrix-form model predicted a linear relationship between the induced pressure pumping and the applied gate voltages. The source of the linearity can be attributed to the difference in the zeta potentials between the FEFC gates:

$$\Delta\zeta_{52} = \zeta_5 - \zeta_2$$

To illustrate the close approximation of the matrix-form model to the experimental results, the slopes of the best-fit line and the matrix-form solution are shown in Table 6.5.

	FEFC Slope (nL/min·V)
Best-fit Line	-0.20
Matrix Solution	-0.25

Table 6.5: Comparison of the slopes of flow rate versus gate voltage for the model and experimental results.

6.2.2 Pressure Distribution Results

Examination of the pressure distribution in the microchannel network highlights how the induced pressures counterbalance the unequal EOF pumping rates. In balancing the flow rates, the difference between the zeta potentials, $\Delta\zeta_{52}$, results in either positive or negative pressures at the T-intersection. To illustrate this relationship, the pressure distributions between the anodic and cathodic reservoirs (equation 6.8) are shown in Figure 6.3 for positive induced pressure and in Figure 6.4 for negative induced pressure. As the applied gate voltages increase, so does the induced pressure at the T-intersection ($x = 9.2$ mm). Also shown in both figures is the pressure profile for the zero gate condition (0/0). The small degree of difference in the zeta potentials for the zero gate condition is sufficient to induce positive pressure at the T-intersection.

Positive Induced Pressure

In Figure 6.3, the pressure decreases over the first section of the microchannel ($0 \leq x \leq 5.7$ mm) prior to the anodic gate. This section has a smaller EOF pumping rate than the adjacent, anodic gate region. A favorable (negative) pressure gradient arises in the first section to balance between the high EOF pumping rate at the anodic gate and the low inherent EOF rate at the first section.

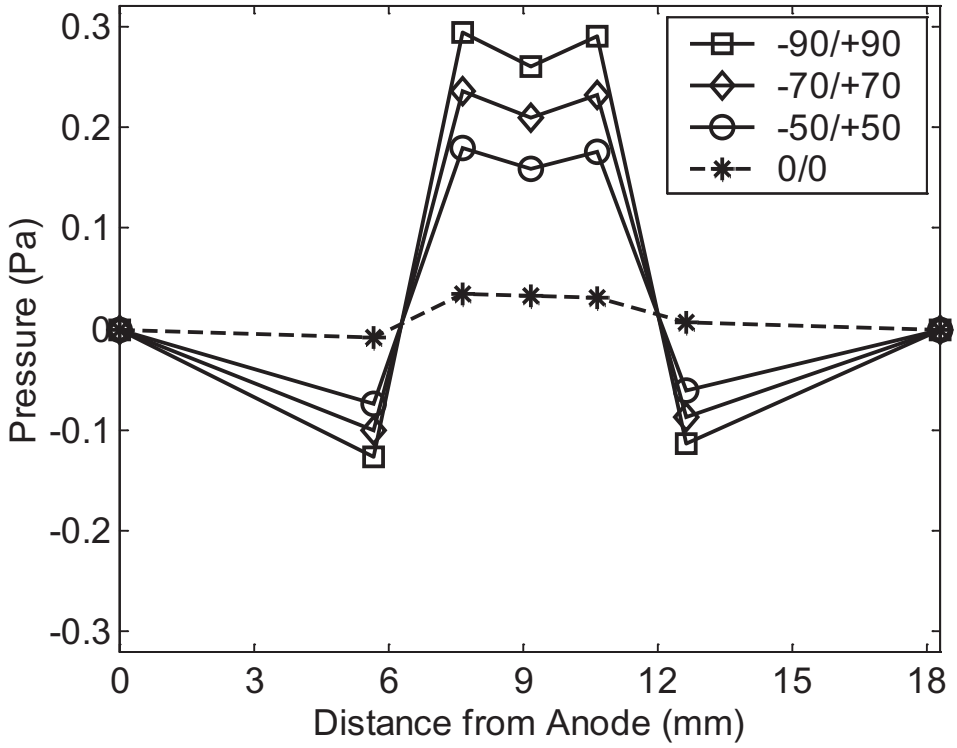

Figure 6.3: Pressure versus microchannel length for positive induced pressure.

The favorable pressure gradient is necessary to increase the total pumping rate in the first section and preserve continuity. Likewise, at the anodic gate ($5.7 \leq x \leq 7.7$ mm), an unfavorable (positive) pressure gradient is induced to lower the total flow rate from the high EOF flow rate from FEFC. A result of the unfavorable pressure gradient is that the pressure rapidly increases and the maximum pressure in the EOF microchannels occurs at the edge of the anodic gate ($x = 7.7$ mm). Similarly, the third section ($7.7 \leq x \leq 9.2$ mm) has a positive total pressure but the favorable pressure gradient is equal to the first section in both magnitude and sign. Identical gradients arise because both sections have the same zeta potential and so the EOF pumping rates are equal between the sections. Therefore, the same favorable pressure gradient is required to maintain continuity between these two sections and the anodic gate section.

On the cathodic side of the intersection, the pressure distribution follows a similar, but opposite trend as the anodic. The fourth ($9.2 \leq x \leq 10.7$ mm) and six sections ($12.7 \leq x \leq 18.4$ mm) have equal, unfavorable pressure gradients due to identical zeta potentials. The unfavorable pressure gradients in the two sections are necessary to decrease the flow rate in order to match with the cathodic gate region. Similarly, the cathodic gate section ($10.7 \leq x \leq 12.7$ mm) has a favorable pressure gradient, since it is necessary to compensate for the low EOF pumping rate from FEFC.

As mentioned in Section 6.3 and shown in Table 6.3, the applied voltage of +90 V at the cathodic gate, V_{CG}, should theoretically produce reverse EOF. However, as seen in the pressure distribution in Figure 6.3 for "-90/+90", the favorable pressure gradient at the cathodic gate increases the total flow rate. On account of this, the favorable pressure gradient acts against the reverse EOF

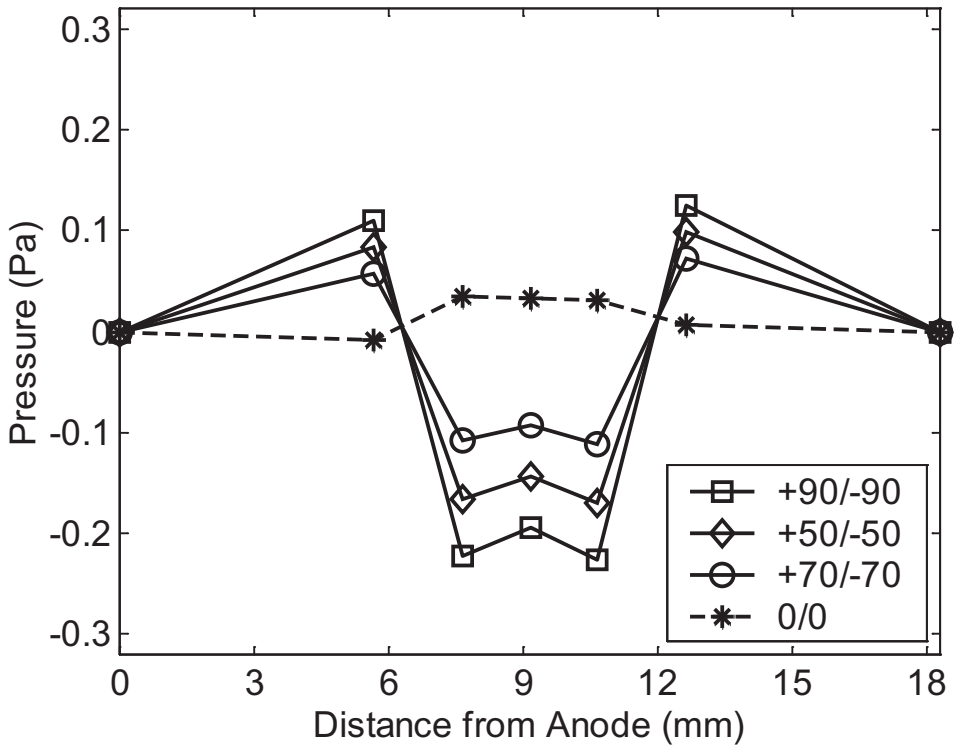

Figure 6.4: Pressure versus microchannel length for negative induced pressure.

pumping. For this reason, reverse EOF may have been present during the micro-PIV experiments, but not observable in the bulk flow.

Negative Induced Pressure

The negative induced pressure distribution in Figure 6.4 is similar to the positive induced pressure, but with opposite pressure gradients. On account of this, the anodic gate region has a favorable pressure gradient to increase the low EOF pumping and decrease the intersection pressure. The opposite is true for the cathodic gate region, where an unfavorable pressure gradient counteracts the high EOF pumping. Additionally, the identical zeta potentials in sections 1 and 3 produce equal pressure gradients. The same is true for sections 4 and 6.

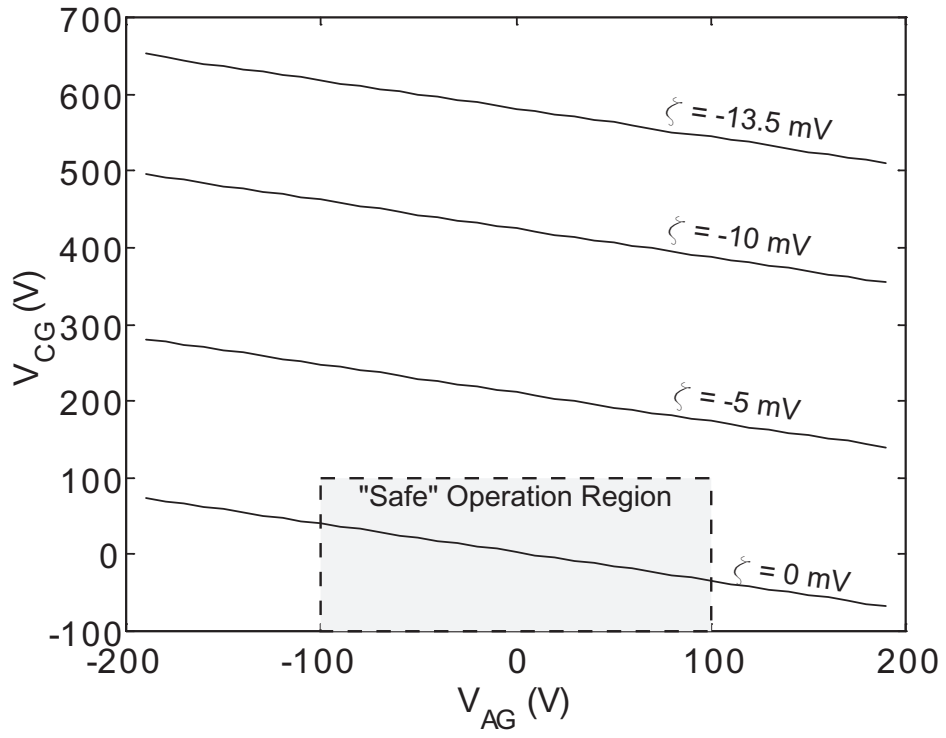

Figure 6.5: Anodic gate voltage versus cathodic gate voltage for 100% flow switching.

6.2.3 Flow Switching

A goal of FEFC in microfluidic networks is the ability to completely "turn-off" the flow in the cathodic microchannel for 100% flow switching between the field-free and cathodic microchannels. This switching allows for efficient transfers of the analytes between microchannels in the network because the cathodic microchannel is closed. To achieve this mode of operation in the T-intersection microfluidic network, the EOF pumping from the inherent zeta potential needs to be compensated with a large gate voltage.

Obtained from the matrix-form model, Figure 6.5 illustrates the gate voltages required for zero flow in the cathodic microchannel, where the effect of induced

pressure is included. The model used the same parameters listed in Table 6.2. At the inherent zeta potential in the experiments ($\zeta = -13.5$ mV), flow switching of 100% is only possible for an extremely high cathodic gate voltage ($V_{CG} \geq 500$ V) for the range of anodic gate voltages shown. However, lower gate voltages can produce 100% flow switching when the inherent zeta potential is extremely low or zero. To avoid dielectric breakdown of the Parylene C, the inherent zeta potential must be very small (≈ 1 mV) in order to achieve ideal flow switching. The region of "safe" operation is illustrated in Figure 6.5. The use of surface coatings [57, 58] in the microchannels may be a viable method to suppress the zeta potential for the demonstration of 100% flow switching. Additionally, lowering the pH of the buffer solution can also reduce the inherent zeta potential, but this can also restrict the type of analytes that can be studied in the network.

6.3 3D Microfluidic Network Model

The matrix-form model developed in Section 6.1 is applied to the experimental results of the 3D microfluidic network from Chapter 5 for further validation of the model. The model verifies that the length of the field-free microchannel influences the flow rate from the induced pressure at the intersection. As before, the microchannels in the network are divided into seven sections to solve for the induced pressure gradients. The pressures at all reservoirs are set to zero. Table 6.6 lists the values used in performing the matrix-form model.

6.3.1 Average Velocity from Model

The matrix-form model for the 3D microfluidic network was written in MATLAB and computed for the different microchannel dimensions and gate voltages

Property	Value	Property	Value
$P_{A,C}$	0 Pa	d	1.2 μm
P_{FF}	0 Pa	L_1	5.6 mm
$\zeta_{i=1,2,4,6}$	-13.5 mV	L_2	4.0 mm
E	26 V/cm	L_3	2.0 mm
a	50 μm	L_4	2.0 mm
b	24 μm	L_5	4.0 mm
c	10 mM	L_6	5.6 mm

Table 6.6: Dimensional values used in 3D network model.

in Table 6.7. As before, the $\mathcal{M}$ matrix was sufficiently conditioned to avoid singularity, and so a scaling factor was unnecessary. In all calculations, the conservation of mass flow was preserved.

The results of the model confirm the experimental trends have agreement between the experimental velocities. As shown in Table 6.7, where the last column is the predicted field-free velocities, the matrix-form model shows that the length of the field-free microchannel determines the degree of induced pressure pumping. The physical explanation for this phenomenon is that induced pressure at the intersection is predominately dependent on the differential EOF from the FEFC gates. As the field-free microchannel length is shortened, the pressure difference between the intersection and the field-free reservoir increases. Hence, this produces larger, favorable pressure gradients in the field-free microchannel.

Overall, the results from the matrix-form model are in close proximity to the experimental velocities. However, some deviation between the results can be seen for the 0.5 mm and 1 mm field-free microchannel lengths. The model

Gate Voltage (V)	Electrode Wid./Dist. (mm)	Field-Free Length (mm)	Measured Velocity (μm/s)	Model Velocity (μm/s)
100	2/8	5	5.43	7.00
100	3/5	2.5	15.28	15.92
100	4/4	5	11.13	13.68
100	4/4	3	16.75	18.83
100	4/4	1	25.04	30.20
100	4/4	0.5	29.05	35.57
80	4/4	1	20.02	24.73
60	4/4	1	14.85	19.25

Table 6.7: Comparison of model and test results for the 3D microfluidic network.

predicted a velocity in the field-free microchannel that was larger than observed experimentally. However, a finding in both of these studies is that FEFC is well suited for pressure pumping between PDMS microchannel layers in a 3D network if they are connected with a short ($L \leq 0.5$mm) microchannel length in the 3rd dimension. Under this configuration, the large pressure pumping rate increases the efficiency of the sample transfer between the microchannel layers.

6.4 Conclusion

A first-order model, derived from the Navier-Stokes relation, is presented in this chapter. The results of the model were in agreement with the experimental data in Chaper 5. The continuity equations in the matrix-form model consisted of a Couette flow term from the EOF and a Poiseuille flow due to the induced

pressure. To solve for the induced pressure gradients from unequal EOF pumping rates, an assumption on the pressure distribution in the system was made. Considering the pressure in the microchannels to be linear piece-wise continuous allowed for solution of the matrix-form model. Conditioning the matrix equations may be required if it is close to singular, depending on the precision of the computation machine. Since the model assumes that the flow is fully developed and due to low Reynolds number flow, the model is valid throughout the network, except near the edges of the FEFC gates.

The matrix-form solution closely matches the experimental results for the field-free pumping in both the T-intersection and 3D microfluidic networks. The accuracy is promising for the application of the model toward future FEFC designs. The pressure gradients in the microchannels adjust the total flow rate in the microchannel to compensate for the differential EOF pumping rates. Reverse EOF may be possible in the microchannel network, but the pressure gradients can act to suppress it. Due to the inherent zeta potentials in the microchannel, completely turning off the flow in the cathodic microchannel is difficult to achieve without exceeding the dielectric strength of the Parylene C film. The 3D microfluidic network demonstrates that decreasing the field-free microchannel length enables larger pumping rates in the field-free microchannel. One issue that was not addressed was whether the location of gate electrodes can improve FEFC. This question will be addressed in the next chapter. With a model that closely matches the experimental results obtained for the polymer microfluidic network, device simulations can be conducted for future microfluidic applications incorporating FEFC in order to minimize fabrication costs and reduce prototyping design steps.

Chapter 7

Multiple Gate Interaction in FEFC

The effect of gate electrodes distance from the FEFC gate is addressed in this chapter. Previous work by Hayes *et al.* [68] demonstrated that the zeta potential control is not localized to the gated region. The authors used a conductive coating on the outside of the glass capillary as the gate electrode. Changing the coverage area of the coating led to the finding that large coverage areas are not required for adequate FEFC. Instead, EOF control was possible for 4% and 60% electrode coverage of the capillary length with similar results. The authors attributed the improved control to the spreading of the zeta potential due to surface conductance in the diffuse layer.

To study the presence of surface conductance in microfluidics using FEFC, a T-intersection network with multiple gates along the EOF microchannels was studied. In this set-up, four of the eight gates were toggled to determine if gate width and gate position have an effect on the control of the EOF. The results were then compared with two models for the zeta potential distribution. The first was the localized model, where the change to the zeta potential was only locally modified at the gate regions. The second model considered that FEFC had extended control over the zeta potentials outside the gate regions.

7.1 T-Intersection with Multiple Gates

To investigate the extension of zeta potential control to regions outside the gate, an all-polymer, multi-gate microfluidic device was built with a T-intersection network [125]. A third, field-free microchannel was connected to the two FEFC microchannels at the T-intersection. The microfluidic network device is shown in Figure 7.1. The cathodic gates (5-8) were held constant with a positive bias to lower the EOF in the cathodic microchannel. The anodic gates were toggled individually with a negative bias to increase EOF in the anodic microchannel. The differential EOF pumping rates induced pressure at the intersection of the microchannels. As a result of the unequal EOF pumping rate, the induced pressure generated pumping in the field-free microchannel. While the anodic gates were toggled, the change in the flow velocity in the field-free microchannel was characterized with micro-PIV.

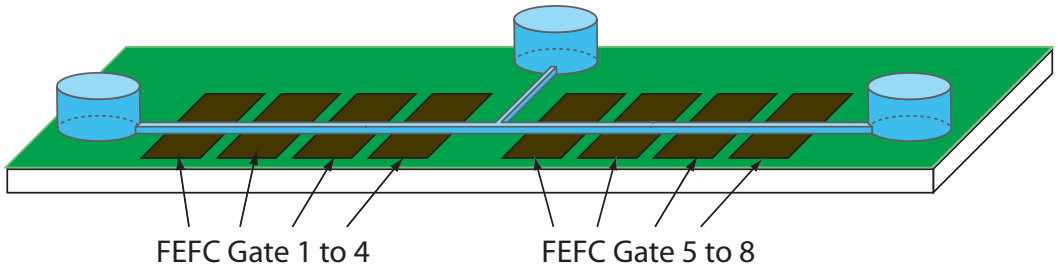

Figure 7.1: Schematic of the multi-gate T-intersection network.

7.1.1 Fabrication

The FEFC gate electrodes were built on polycarbonate substrates (Makrolon, Sheffield Plastics Inc., Sheffield, MA). The plastic wafers were placed in an e-beam evaporator for metal deposition. The chromium layer was first evaporated onto

the polycarbonate to a 200 Å thickness to be the adhesion layer for the next metal layer. The second layer was gold deposited to a 3500 Å thickness. The metal layers were patterned and etched prior to the Parylene C coating, which was deposited to a thickness of 2.55 μm on the entire wafer surface at NASA Goddard Space Flight Center (Greenbelt, MD).

The master mold for the microchannel was fabricated with SU-8 on a 100 mm silicon wafer (Silicon Quest Intl., Santa Clara, CA). After spinning the SU-8 photoresist (MicroChem Corp., Newton, MA) to a 30 μm thickness on the wafer, the photoresist was patterned with a flood exposure lamp (Sunray 400, Unvitron International Inc., West Springfield, MA) and developed with SU-8 developer (MicroChem Corp., Newton, MA). The mold produced microchannels with vertical sidewalls and rectangular cross-sections. The microchannels were molded from PDMS (Sylgard 184, Dow Corning, Midland, MI) poured onto the SU-8 master. After curing the PDMS for 2 hours at 60°C in a convection oven, the entrance to the microchannels were opened with 2 mm diameter holes punched into the PDMS for the reservoirs. The cross-section of all the PDMS microchannels were 30 μm in height and 105 μm wide.

7.1.2 Experimental Proceedure

Two power supplies were used to apply the EOF electric field and three power supplies were used for the eight FEFC gate electrodes. Control of the power supplies was performed with LABVIEW (National Instruments, Austin, TX), a PCI-6711 multiplexer card (National Instruments) and eight MR62-6S relays (NEC Tokin, Seoul, Korea). The cathodic gate voltages were held at a constant positive bias during the experiments and the anodic gates were addressed indi-

vidually with a zero, floating, or negative bias. The biasing for the gates was ±90 V for the first tests and ±135 V for the second tests. The voltage configurations created positive pressure flow in the field-free microchannel.

The voltages applied to the anodic gates were switched at 7 second intervals between the voltage configurations shown in Table 7.1, which was automated in LABVIEW. The first voltage configuration (case 'All') activated all the gates for large gate coverage area. Before switching to the next gate configuration, the gates are grounded (GND) to remove the charge at the gates. The single gate configurations (cases 1 to 4) held one anodic gate at a negative bias and the other three gates at a floating potential (FLT) to deactivate them. If the gates were grounded instead, then FEFC would be present at each gate due to the potential difference between the voltage in the microchannel from the longitudinal electric field and the grounded gate potential. A floating potential at the deactivated gates enables the zeta potential to be defined without the influence of FEFC. Previous experiments showed that grounding the gate electrodes was necessary prior to the floating potential condition in order to remove the residual charge at the gate electrode from the previous voltage configuration.

Acetic buffer solutions for the visualization experiments were prepared to 2 mM concentrations at pH 3.8. As before with previous micro-PIV experiments in Chapter 5, the 2.0 μm diameter microparticles (polystyrene Fluorobrite microparticles, Polysciences, Warrington, PA) were treated for 12 hours in 25 mM $Fe(NH_4)_2(SO_4)_2{\cdot}6H_2O$ to reduce their electrophoretic charge. The microparticles were filtered out of the iron ammonium sulfate solution with a syringe filter (0.45 μm MCE Filter, Fisher Scientific), rinsed with deionized water, and extracted into the acetic buffer solution to be used for the flow visualization experiments.

Case	Gate 1	Gate 2	Gate 3	Gate 4
All	**-VG**	**-VG**	**-VG**	**-VG**
-	GND	GND	GND	GND
1	**-VG**	FLT	FLT	FLT
-	GND	GND	GND	GND
2	FLT	**-VG**	FLT	FLT
-	GND	GND	GND	GND
3	FLT	FLT	**-VG**	FLT
-	GND	GND	GND	GND
4	FLT	FLT	FLT	**-VG**
-	GND	GND	GND	GND

Table 7.1: Multi-gate voltage sequence.

The fluorescent microparticles flow was recorded in the field-free microchannel for velocity measurement of the pressure induced pumping. The image recording was performed on a Nikon TE-2100-S fluorescent inverted microscope (Nikon, USA) using a B-2E/C FITC filter (excitation 465-495 nm, emission 515-555 nm). A 640x480 pixel CCD camera (DKF-4303, The Imaging Source, Charlotte, NC) was used to record the flow of the microparticles in the microchannel at 30 fps. Post-processing of the velocity measurements was performed with the aid of the image processing toolbox in MATLAB (The Mathworks, Natick, MA). A Sobel edge detection method was used to determine boundary pixels of each of the microparticles. The position of the center pixel for each of the microparticles was measured between two image frames, separated by a 2 second time interval. A scale conversion of 0.75 μm/pixel was used to measure the position of the

microparticles in each frame. The velocity for each voltage configuration of the FEFC gate electrodes was determined from the position change between the two frames.

7.1.3 Micro-PIV Results

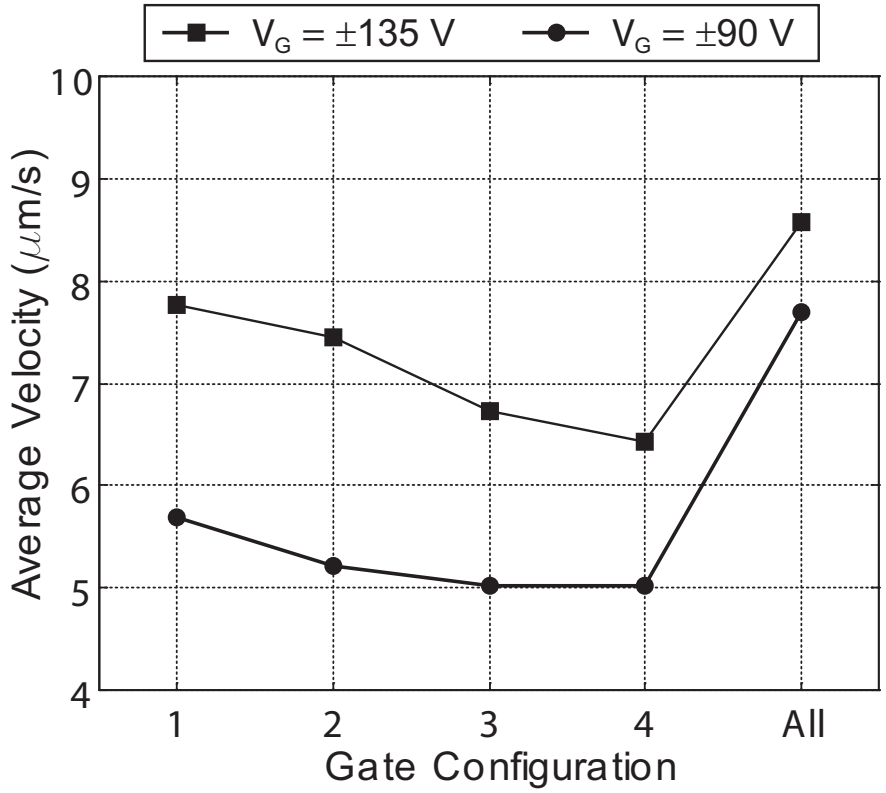

Figure 7.2: Velocity measurements for the multi-gate network.

The goal of the gate voltage configurations in Table 7.1 was to determine the effect of gate area and gate position on the FEFC-modified zeta potentials. Case 'All' toggled all four gates in the anodic microchannel on at the same negative bias for large gate coverage. The other four cases individually toggled the four anodic gates for small gate coverage and for varied gate positions. The field-free

pumping was recorded and analyzed to gauge the change in the EOF pumping in the microchannel network. The results from the micro-PIV analysis is shown in Figure 7.2 for the two gate voltages (±90 V and ±135 V).

The results from the multi-gate network show that both gate position and gate area have an effect on the induced pressure pumping in the field-free microchannel. Toggling between gates 1 to 4 resulted in decreased pressure pumping in the field-free microchannel as the active gate was moved closer to the T-intersection. When all gates are turned on (case 'All') the field-free velocity was greater than for the single gate cases.

Gate Position Results

As developed in Section 6.2.1, field-free pumping is attributed to unequal EOF pumping rates between connected microchannels. As the active gate moved closer to the intersection, the experimental results in Figure 7.2 show that the field-free velocity decreases (cases 1 to 4). Since the cathodic gates were held constant, the EOF pumping rate in the anodic microchannel must have decreased during the four cases in order to lower the field-free pumping rate. The change in the EOF pumping versus gate position can be attributed to a lower transverse electric field for the gates closer to the T-intersection. A lower transverse electric field reduces the change in the EOF pumping of the anodic microchannel.

The lower transverse electric field was due to the fact that the internal voltage was largest at gate 1 and linearly decreased along the microchannel, on account of the longitudinal electric field that produces the EOF. The change in internal voltage resulted in a lower transverse electric field as the active gate moved toward the intersection. Since the gate voltage applied to gates 1 to 4 was a constant

negative value throughout the configurations, the difference in the inner voltage potentials reduced the transverse electric field. Moreover, the decrease in field-free pumping followed a negative linear slope as the active gate drew closer to the T-intersection, which supports the claim that the longitudinal electric field was the source of this phenomenon. For cases 1 to 4, the negative linear slope between the field-free flow and gate position is apparent in Figure 7.2 for both the VG = ±90 V and VG = ±135 V data. Verification of the effect of gate position and the longitudinal electric field is addressed with the matrix-form model in the next section.

Gate Area Results

For both gate voltages applied, the gate coverage in case 'All' produced the largest field-free pumping. Also, the magnitude of the gate voltage affected the field-free pumping, since VG = ±135 V produced a higher velocity than VG = ±90 V. The lower pumping for the single gate cases implies that the induced pressure at the intersection also depended on the gate coverage area. Clearly, the larger gate area has a larger EOF pumping rate than the single gate cases. As a result of this, a larger unfavorable pressure gradient was required to maintain continuity in the anodic microchannel. Thus, a larger positive pressure was generated at the intersection due to the induced pressure gradient. Further conclusions on the effect of increased gate area are addressed with the matrix-form model in the next section.

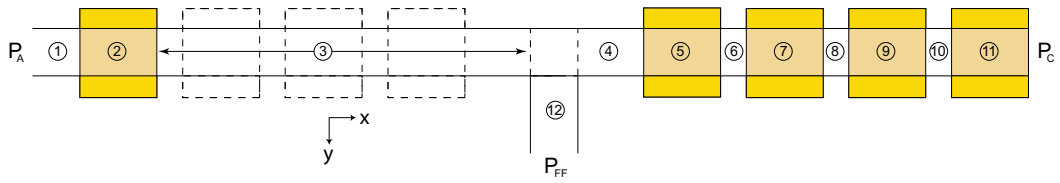

Figure 7.3: Analytical model of discretized multi-gate network.

7.2 Zeta Potential Distribution

Two models are proposed to investigate whether FEFC has extended influence over the zeta potentials at regions outside the gates. Experimental results in Section 7.1 showed that both gate position and gate area influence the induced pressure pumping in the microchannel network. The first model localizes the change in the zeta potentials so that the modification occurs only at the gated regions. The second model includes the proposed "spreading" of the FEFC-modified zeta potential to regions outside the gated areas. The second model describes the extended influence of FEFC with zeta potentials that follow an exponential decay. The extended zeta potential control may be due to the surface conductance or another form of charge distribution.

7.2.1 Localized Model

In the localized model, the effect of the transverse electric field modifies the zeta potential at only the gate regions. Outside of the gates, the zeta potential remains unchanged and is equal to the inherent zeta potential, ζ_0, which is due to the chemical surface charge of the Parylene C wall with the acetic acid buffer solution. The double capacitor model predicts the localized changes to the zeta potential at the gate regions in this model.

The localized model is nearly equivalent to the matrix-form model presented

in Chapter 6, but the microchannel is discretized into twelve sections as seen in Figure 7.3. The lengths of sections 1 to 3 are varied in order to model the toggling of the active gates (cases 1 to 4). As with the matrix-form model in Chapter 6, the continuity equations for the ten interfaces are coupled with two pressure equations to create a matrix-form equation to solve for the induced pressure gradients. To help illustrate the twelve equations used in the localized model, $\mathcal{M}$ in equation 6.11 is:

$$\mathcal{M} = \begin{bmatrix} -H & H & 0 & 0 & 0 & \dots & 0 & 0 \\ 0 & -H & H & 0 & 0 & \dots & 0 & 0 \\ 0 & 0 & -H & H & 0 & \dots & 0 & H \\ 0 & 0 & 0 & -H & H & \dots & 0 & 0 \\ \vdots & \ddots & \ddots & \ddots & \ddots & \ddots & \ddots & \vdots \\ 0 & \dots & \dots & \dots & 0 & -H & H & 0 \\ L_1 & \dots & \dots & \dots & \dots & L_{10} & L_{11} & 0 \\ L_1 & L_2 & L_3 & 0 & \dots & \dots & 0 & L_{12} \end{bmatrix} \tag{7.1}$$

7.2.2 Exponential Decay Model

In the exponential decay model ($\exp(-\alpha x)$), the change in the zeta potential at the gate region extends over the sections of the microchannel adjacent to the gate. The "spreading" of the modified zeta potential is modeled with exponential decay. To illustrate this model, the exponential decay on either side of the gate region is shown in Figure 7.4. For the sections adjacent to the gates, the zeta potentials decay toward the inherent zeta potential, ζ_0, according to the coefficient in the exponential, α, which has units of inverse meters. In contrast, at the gate region, the double capacitor model is applied to determine the modified zeta

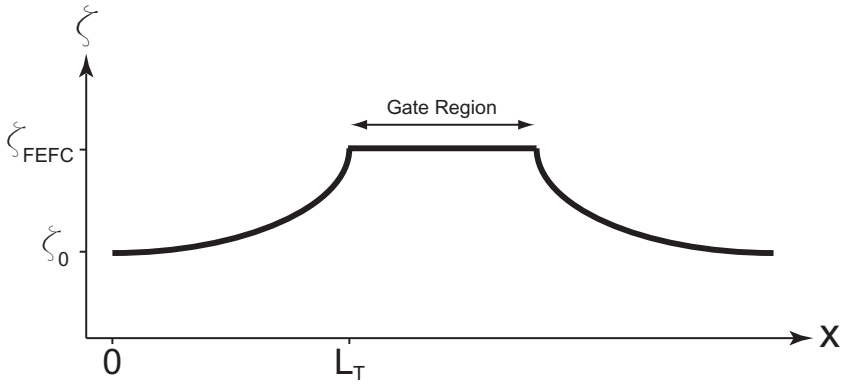

Figure 7.4: Diagram of exponential decay of the zeta potential for a single gate. L_T is the distance between the origin and the gate region.

potential, ζ_{FEFC}. Here, the zeta potential is assumed to be constant over the entire gate region. An exponential decay description was chosen because at large values of the exponential coefficient ($\alpha \rightarrow \infty$), the exponential decay model reduces to the localized model described in Section 7.2.1.

The function that describes the zeta potential to the left of the gate region with respect to position is

$$\zeta_L(x) = \zeta_0 + (\zeta_{FEFC} - \zeta_0) \exp(-\alpha (L_T - x)) \tag{7.2}$$

where L_T is the length of the region to the left of the gate region. Likewise, the zeta potential function for the other side of the gate region is

$$\zeta_R(x) = \zeta_0 + (\zeta_{FEFC} - \zeta_0) \exp(-\alpha x) \tag{7.3}$$

With these two basic functions, the model can describe the zeta potential distribution for each section of the microchannel network. Recall that the microchannel is sparsely discretized in the matrix-form model, so that one length element describes either a single gate region or an adjacent, ungated region. On account of this, the *average* of the zeta potential distribution for each section is calculated

for individual zeta potentials in the vector Z of equation 6.11. With the average zeta potential known for each of the twelve sections, the matrix-form solution can be applied to determine the resulting induced pressure gradients.

To measure the extended control, the zeta potential decays to 5% of its gate region value at a distance, L_d, from the gate. From equation 7.3, the following relationship is derived to characterizes the decay length, L_d:

$$\frac{\zeta_R(L_d) - \zeta_0}{\zeta_{FEFC} - \zeta_0} = \exp(-\alpha L_d) \tag{7.4}$$

$$0.05 = \exp(-\alpha L_d) \tag{7.5}$$

$$L_d \approx \frac{3}{\alpha} \tag{7.6}$$

The relationship is inversely proportional to the coefficient of the exponential, α, and Table 7.2 lists the distance L_d for a range of values of α from equation 7.6. The value of $\alpha = 1000$ denotes the region where the decay length begins to follow a quasi-linear relationship with the coefficient of the exponential, so that large changes in α result in small changes in L_d. Lower values ($\alpha \leq 1000$) correspond to the asymptotic region, where the decay length has large changes for small changes in α.

Single Gate Equations

With the exponential decay descriptions in equations 7.2 and 7.3, the average zeta potential, $\bar{\zeta}$, is the integral average over the length of the section. For the section to the left of the gate region, the average zeta potential is

$$\bar{\zeta_L} = \frac{1}{L}\int_0^L \zeta_L(x)\, dx$$

$$\bar{\zeta_L} = \zeta_0 + \frac{1}{\alpha L}\left[\alpha\zeta_0 L + (\zeta_{FEFC} - \zeta_0)(1 - \exp(-\alpha L))\right] \tag{7.7}$$

α (m^{-1})	L_d (mm)
100	30
200	15
300	10
500	6
1000	3
2000	1.5
3000	1

Table 7.2: Exponential decay coefficient (α) versus decay length (L_d).

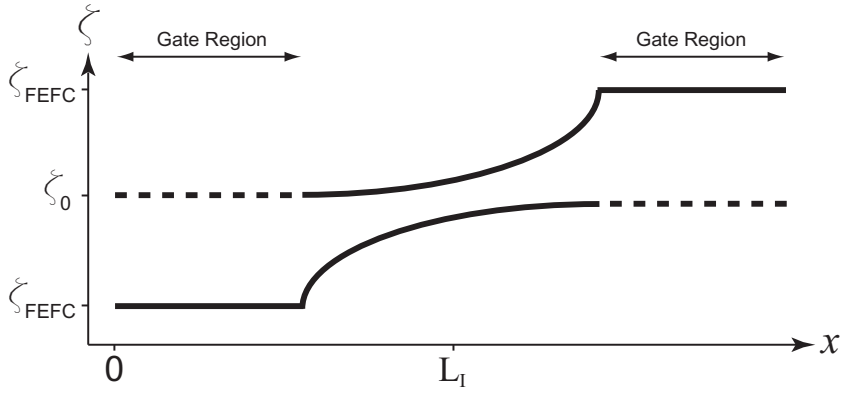

Figure 7.5: Overlap of the zeta potential exponential decay for two gates.

The integral average for the section to the right of the gate region is identical to equation 7.7:

$$\bar{\zeta_R} = \frac{1}{L}\int_0^L \zeta_R(x)\, dx$$

$$\bar{\zeta_R} = \zeta_0 + \frac{1}{\alpha L}\left[\alpha\zeta_0 L + (\zeta_{FEFC} - \zeta_0)\left(1 - \exp(-\alpha L)\right)\right] \tag{7.8}$$

Double Gate Equations

In addition to the single gate equations, the interaction of the exponential decay for two gates is required. When the two potential distributions overlap as shown in Figure 7.5, the average value of both functions are taken in determining the average zeta potential. It is assumed that the "spreading" of the zeta potential is confined to only the ungated regions. Therefore, it is assumed that the neighboring gate regions do not affect each other and that their model zeta potential is determined from the double capacitor model solely. The overlap from adjacent gate regions occurs at sections 3, 4, 6, 8, and 10 in Figure 7.3. For all five sections, the integral average is

$$\bar{\zeta_i} = \frac{1}{2L_i} \int_0^{L_i} \left(\zeta_L\left(x\right) + \zeta_R\left(x\right)\right)\, dx$$

where L_i is the length of the section over which the average is taken. The zeta potentials ζ_L and ζ_R correspond to the modified zeta potentials for the left and right gate regions, respectively.

For sections 3 and 4, which are adjacent to the T-intersection of the microchannels ($x = L_I$), the average zeta potential is determined from the overlap. For section 3, which is to the left of the intersection, the average zeta potential is

$$\begin{aligned} \bar{\zeta_3} &= \zeta_0 + \frac{1}{2\alpha L_3}\left[\left(\zeta_0 - \zeta_2\right)\left(\exp\left(-\alpha L_3\right) - 1\right)\right. \\ &\quad \left. + \left(\zeta_5 + \zeta_0\right)\left(\exp\left(-\alpha\left(L_4\right)\right) - \exp\left(-\alpha L_T\right)\right)\right] \end{aligned} \tag{7.9}$$

and for section 4, which is to the right of the intersection

$$\begin{aligned} \bar{\zeta_4} &= \zeta_0 + \frac{1}{2\alpha L_4}\left[\left(\zeta_0 - \zeta_2\right)\left(\exp\left(-\alpha L_T\right) - \exp\left(-\alpha L_3\right)\right)\right. \\ &\quad \left. + \left(\zeta_5 - \zeta_0\right)\left(1 - \exp\left(-\alpha\left(L_4\right)\right)\right)\right] \end{aligned} \tag{7.10}$$

where L_3 and L_4 are the lengths of the sections to the left and right of the intersection, respectively, and L_T is the total length of the region between the two gates ($L_T = L_3 + L_4$). For sections 6, 8, and 10, there is only one microchannel section between the two gate regions and so the average zeta potential is

$$\bar{\zeta_i} = \zeta_0 + \frac{1}{2\alpha L_i}\left[\left(\zeta_{i-1} + \zeta_{i+1} - 2\zeta_0\right)\left(1 - \exp\left(-\alpha L_i\right)\right)\right] \tag{7.11}$$

7.2.3 Model Comparison with Test Data

With equations 7.7 to 7.11 to describe the zeta potental distribution, the matrix-form model of the continuity and pressure equations can be solved to determine the induced pressures in the multi-gate microfluidic network. The matrix-form model was written in MATLAB and computed for the five gate conditions listed in Table 7.1. The $\mathcal{M}$ matrix was sufficiently conditioned to avoid singularity, and so a scaling factor was unnecessary. The results for the predicted field-free pumping were compared to the experimental data (Figure 7.2) in Figure 7.6 for VG = $\pm$135 V and in Figure 7.7 for VG = $\pm$90 V. It is important to note that the localized model is denoted as $\alpha = \infty$ in both figures. The exponential decay model was performed for two arbitrary values of α ($\alpha = 300$ and $\alpha = 1000$). These values correspond to the quasi-linear and asymptotic regions in Table 7.6.

Predicted Velocity For Single Gate Cases

For both gate voltages, the localized model better predicted the linear trend in the experimental results for the effect of gate position. Figure 7.8 illustrates the close agreement between the localized model (dashed line) and the experimental results. In contrast, the exponential model in Figure 7.6 and 7.7 predicted that

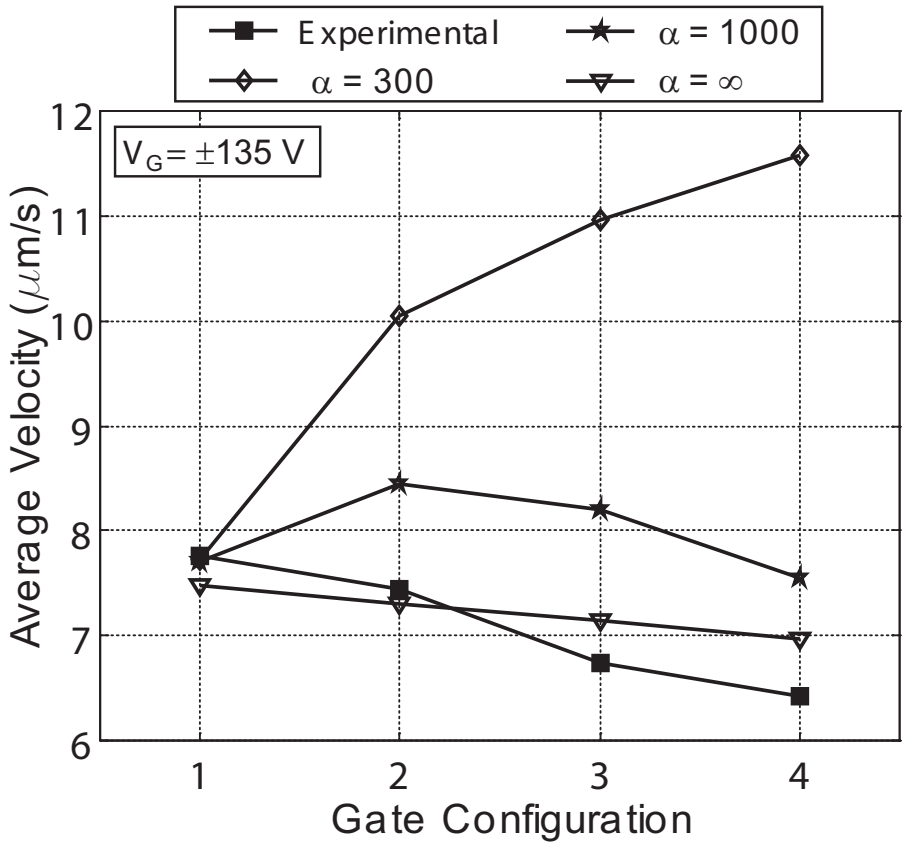

Figure 7.6: Comparison of localized model ($\alpha = \infty$) and exponential decay model ($\alpha = 300, 1000$) versus the experimental results for the multi-gate network at VG = $\pm$135 V.

the field-free pumping increased as the toggled gate moved closer to the intersection. Thus, the exponential model did not predict the experimentally observed trend.

For low exponential decay and large "spreading" of the zeta potential, ($\alpha = 300$), the model predicted that the field-free pumping increased as the active gate was moved closer to the T-intersection. The results for high exponential decay ($\alpha = 1000$) were closer to the experimental, but the predicted field-free velocities were larger than those observed. As seen in the two values of α displayed, the

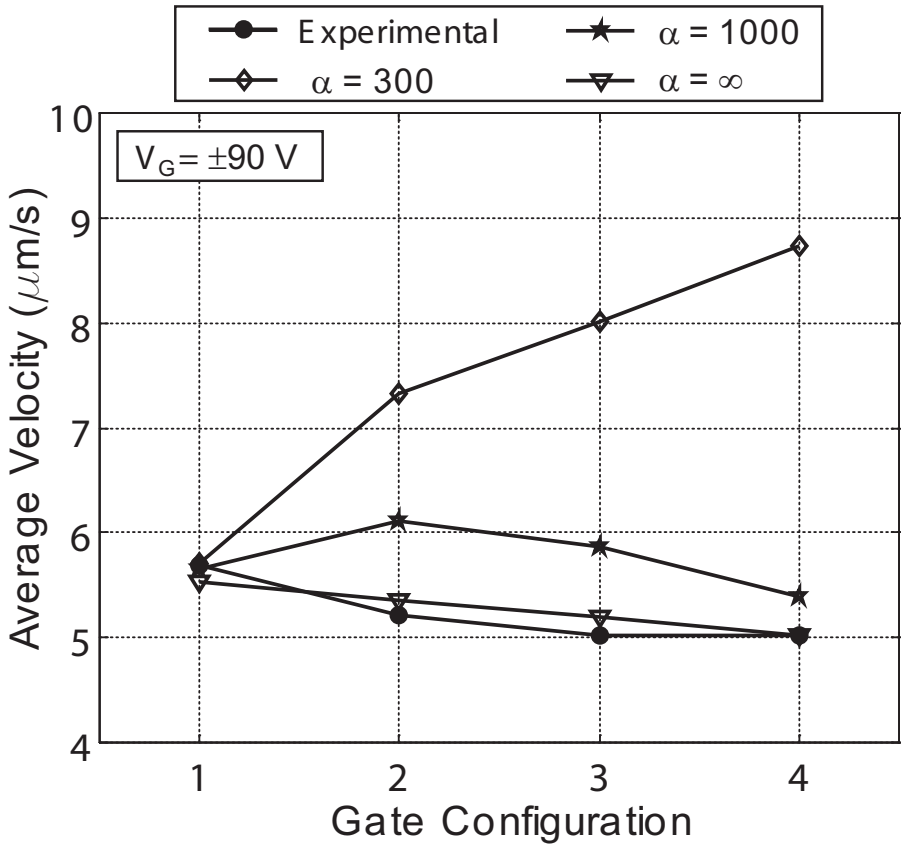

Figure 7.7: Comparison of localized model ($\alpha = \infty$) and exponential decay model ($\alpha = 300, 1000$) versus the experimental results for the multi-gate network at VG = $\pm$90 V.

exponential decay model would reduce to the localized model for large values of α. The convergence to the localized model is seen in the results for $\alpha = 1000$ which show a linear relationship with gate position for gates 2, 3, and 4 that closely resembles the localized model.

As discussed in Section 7.1.3, the decrease in field-free pumping is due to lower internal voltages at the gates closer to the T-intersection. Both models took the EOF potential above the gates into consideration during the calculations. However, the "spreading" of the modified zeta potential in the exponential decay

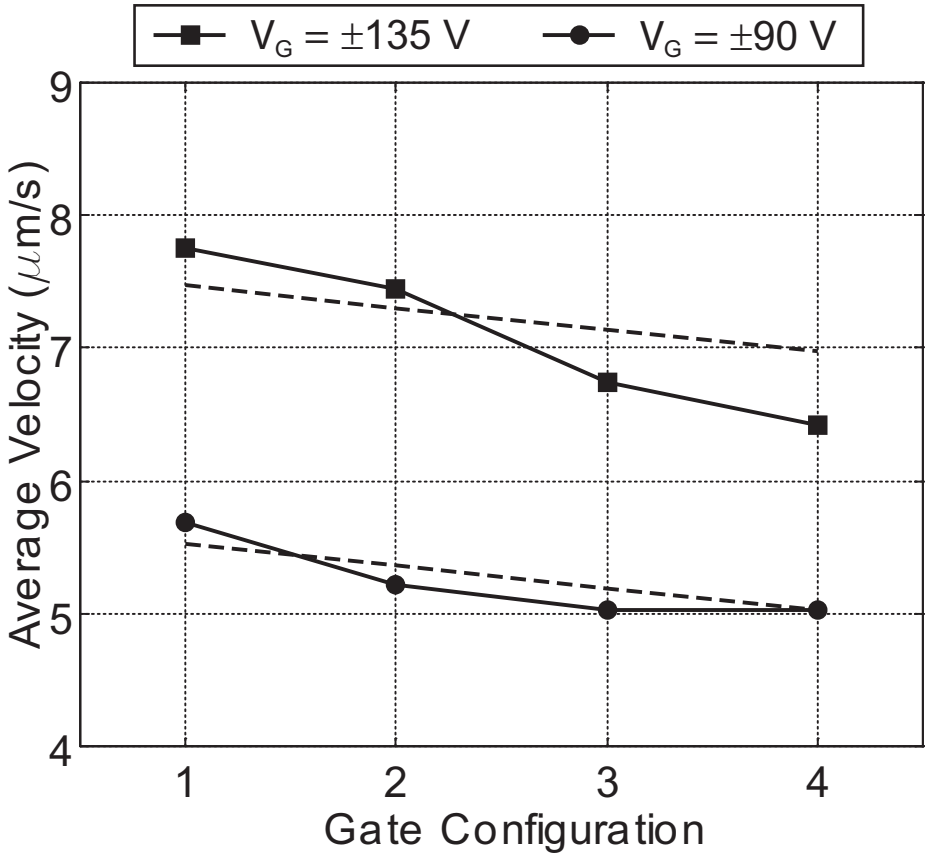

Figure 7.8: Localized model (dashed lines) versus the experimental results for the multi-gate network at VG = ±135 V and VG = ±90 V.

model deviated the results from the experimental. In this model, the average zeta potential to the left of the anodic gate was larger than the inherent zeta potential, due to the exponential decay effect. This resulted in a larger predicted EOF pumping in the anodic microchannel than that for the localized model. As the toggled gate moved toward the intersection, the exponential decay model predicted the EOF pumping in the anodic microchannel to increase, which was a result of the extended zeta potential region. In contrast, the localized model predicted the EOF pumping to decrease. Thus, the exponential model predicted

larger field-free velocites for gates closer to the T-intersection than the localized model.

Predicted Velocity For Case 'All'

Neither the localized matrix-form model nor the exponential decay model accurately predicts the effect of gate coverage on the field-free velocity. The model and experimental results for case 'All' are listed in Table 7.3 for both applied gate voltages. These velocities are nearly double those observed experimentally. In addition, the experimental results observed a field-free velocity for case 'All' that was 10% to 45% larger than those for the four single gate velocities. Instead, the localized model predicted a field-free velocity that was 60% to 66% larger than the single gates velocities. The lack of agreement between the experimental results and local model predictions highlights the need for further evaluation of the mechanism for the effect of gate coverage.

	Field Free Velocity (μm/s)			
Voltage	Data	$\alpha = 300$	$\alpha = 1000$	$\alpha = \infty$
$\pm$90 V	7.69	15.04	13.63	13.87
$\pm$135 V	8.58	20.34	19.18	19.50

Table 7.3: Comparison of experimental data and model results for flow velocity in the field-free microchannel for case 'All'.

Recalling the FEFC control slopes for partial gate coverage in a single microchannel (Table 4.3), the control slopes for 66%, 16%, 13%, and 5% gate coverage are in close agreement with each other. However, the 66% gate coverage exhibited lower EOF mobilities for the gate voltages applied than the other three

cases. The lower EOF mobilities may be an artifact of the larger gate areas as discussed in Section 4.2.4. This trend may support the lower than expected field-free pumping in the multi-gate network, due to a lower EOF pumping in the anodic microchannel. In the calculations, the internal voltage was taken at the midpoint of the gate length, which does not account for the linearly varying internal voltage across the gate. Thus, for large gate area calculations, the localized matrix-form model does not consider the varying transverse electric field. In the multi-gate microchannel network, the gate area for a single active gate was 20%. For all four gates active, it was 80%. Thus, case 'All' may have had a lower EOF pumping than predicted in the matrix-form model.

Pressure Distribution for Localized Model

Using the localized matrix-form model, the pressure distribution between the anodic and cathodic reservoirs is plotted in Figure 7.9 for VG = ±90 V. In the anodic microchannel, the pressure gradient at the active gate decreased as it moved closer to the T-intersection (cases 1 to 4). This trend is attributed to the decrease in the transverse electric field for gates closer to the intersection. Likewise, the pressure distribution in the cathodic microchannel remains relatively unaffected by the toggling of the anodic gates. As a result of this, the active gate position only minutely affected the induced pressures at the intersection (see inset in Figure 7.9).

For case 'All', the cathodic pressure distribution changes to compensate for the increased induced pressure at the T-intersection. The differences between the single gate cases and case 'All' show that the pressure gradients in the cathodic microchannel are only slightly dependent on the position of the anodic gate and

more dependent on the gate coverage area. For all cases, the pressure gradients in sections 1 and 3 are equal and the gradients in sections 4, 6, 8, and 10 are equal, which is due to identical inherent zeta potentials. This was confirmed in Section 6.2.2 for the double gate T-intersection network.

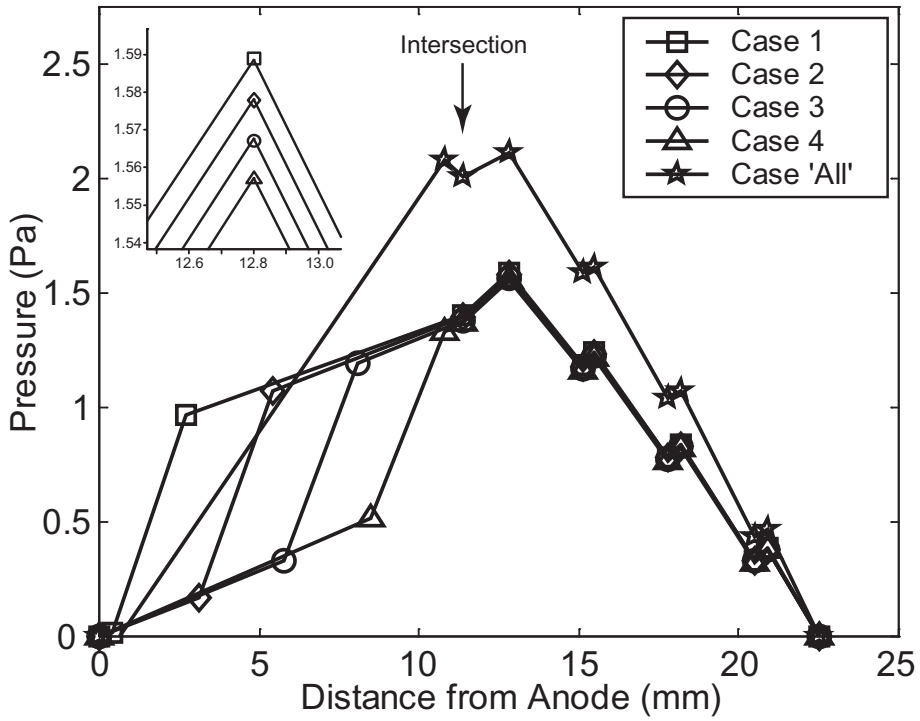

Figure 7.9: Pressure versus microchannel length for the multi-gate network for VG = ±90 V from the localized model.

7.3 Conclusion

The development of a multi-gate microfluidic network for the investigation into the effect of gate position and gate coverage is presented. The four cathodic gates were biased with a positive voltage and the four anodic gates were toggled individually with a positive bias for positive induced pressure. The experimental

results showed that the field-free velocity decreased as the active gate moved closer to the T-intersection due to the longitudinal EOF electric field. The results also revealed that gate coverage area has an effect on the field-free pumping to increase the EOF pumping rate.

To better understand the experimentally obtained trends in gate position and gate area, two models were proposed, both which use the matrix-form solution developed in Chapter 6. The first model includes the effect of FEFC as a local change in the zeta potential at the gate region. The second model uses an exponential decay to describe an extended control of the zeta potential to regions outside the gates. When compared to the experimental results, the localized matrix-form model better predicts the experimental results for gate position. However, neither model accurately predicts the effect of gate coverage area, which requires further investigation. In spite of this, for future applications of FEFC, the position of the gate electrodes must consider the internal voltage above each gate to predict the performance of FEFC.

From both the experimental and model results, there is a relationship between gate coverage area and induced pressure pumping, but the source of this phenomenon is uncertain. However, given the accuracy in the localized matrix-form model for the effect of gate position, the "spreading" of the zeta potential is not likely to be present with Parylene C or PDMS as the microchannel wall material. These polymer materials may lack the degree of surface conductance at the microchannel wall that has been reported in fused silica capillaries.

Chapter 8

Conclusions and Future Work

In this dissertation, the development of all-polymer microfluidic network devices using FEFC gates are presented. In pursuit of this goal, the design and characterization of silicon and polymer microfluidic networks were undertaken. Research contributions were made in the development of a suitable polymer material for FEFC, a novel microflow characterization technique for differential EOF, demonstration of non-mechanical, non-peristaltic bi-directional pumping in a microfluidic network, and the development of an electro-fluid flow model for the design of future FEFC microfluidic networks.

In the fabrication and characterization of field-effect flow control, a silicon microfluidic network was pursued to develop the research strategies necessary for the development of an all-polymer FEFC microfluidic device. The silicon wafer was selectively doped to create p-n junctions for the FEFC gates. Due to overdoping of the implanted boron atoms, the independent FEFC gates were not attainable but a degree of the intended device operation was characterized. The microchannels were fabricated with deep reactive ion etching and the microchannel wall was 0.4 μm thick silicon dioxide. The technique of current monitoring measured the change in flow velocity versus applied FEFC gate voltage. The results showed that the EOF was controllable from 150% to 50% of the original velocity and had

agreement with the double capacitor model. Additionally, improved EOF control at low buffer pH was experimentally confirmed for pH 3, 4, and 5.

Leveraging from the experience gained in the silicon microfluidic multiplexer, the next research phase was the development of an all-polymer microchannel with FEFC. Polymers with high dielectric strengths, high dielectric constants, and ease of fabrication were considered. Of the candidates, Parylene C exhibits the highest FEFC quality and fabrication compatibility with other polymer substrates, due to its low temperature deposition and thin-film conformal coating. The single microchannel device consisted of a silicon wafer with a 1.2 μm of Parylene C coating and micromolded PDMS microchannels that were 40 μm $\times$ 100 μm and 1.7 cm long. With current monitoring, the EOF was shown to be controllable from 240% to 60% of the original velocity. From the experimental velocity results, the gate voltages from -120 V and +120 V varied the zeta potential from -33 mV to -8 mV. Partial gate coverage was also tested for a single microchannel for their feasiblity in microfluidic networks. The devices consisted of polycarbonate substrates with metal electrodes, which varied in length. The polycarbonate substrate and metal electrodes were coated with a 1.2 μm thick Parylene C coating. The current monitoring for the 66%, 16%, 13%, and 5% gate coverage devices demonstrated similar flow controllability, but with lower EOF mobilities for the 66% gate coverage devices.

The all-polymer FEFC microchannels were incorporated into microfluidic networks with 2nd and 3rd dimensional microchannels. Current monitoring is limited to measuring the flow in a single microchannel and so a flow visualization method was developed for the interconnected microchannels. Adapted from micro-particle image velocimetry, 2.0 μm diameter fluorescent microparticles were

treated in an iron ammonium sulfate solution to reduce their electrophoretic mobility for the flow characterization. The first microfluidic network consisted of two EOF microchannels and a third microchannel that was field-free. Voltages of ±90 V, ±70 V, and ±50 V were applied to the two FEFC gates for independent EOF control. The different flow rates in the EOF microchannels induced pressure at the T-intersection, which resulted in non-mechanical, non-peristaltic, and ultra-low pressure pumping in the field-free microchannel. The pressure pumping was demonstrated to be bi-directional from the ability to switch the voltage applied at the two gates and induce both positive and negative pressure at the intersection. The velocity in the field-free microchannel was characterized for the different gate voltages with an in-house MATLAB code. The gate voltages induced field-free pressure gradients between -36.0 Pa/m to 36.1 Pa/m. Additionally, a linear relationship of -0.20 nL/min·V between induced flow rate and applied gate voltage was observed. The applied gate voltages varied the flow rate in the field-free microchannel from -2.0 nL/min to 2.0 nL/min but larger or smaller flow rates are possible with different microchannel dimensions, as observed in the 3D microfluidic network and the multi-gate network.

With the microfluidic network technology demonstrated, investigation into the system-level considerations was undertaken with a matrix-form solution of the analytical equations for the system. The matrix-form model solved for the induced pressure gradients with the continuity equations, which were developed from the Navier-Stokes relation and double capacitor theory, and with the pressure distribution equations in the network, which were assumed to be linear piece-wise continuous. The matrix-form model closely agreed with the control slopes for the field-free pumping that were experimentally obtained for the T-intersection net-

work (-0.20 nL/min·V vs. -0.25 nL/min·V). The model also predicted that 100% flow switching was attainable in the T-intersection network for low inherent zeta potentials ($\zeta_0 \approx 1$ mV). Moreover, the matrix-form model verified the field-free length versus induced pressure of the 3D network results.

The matrix-form model was further tested with a study of the interaction of multi-gates in a microchannel network. The T-intersection microfluidic network was fabricated with eight independently FEFC gates. The cathodic gates were held at a constant positive gate voltage and the anodic gates were toggled individually at an equal, but negative gate voltage. The changes in the positive field-free pumping were recorded as each of the four gates were toggled on. For gate voltages of $\pm$135 V and $\pm$90 V, the field-free pumping decreased as the active gate moved closer to the intersection. The matrix-form model verified that these results were due to the different internal voltages above the four gates. Additionally, when all four anodic gates were toggled on, the field-free velocity was greater than for the velocities obtained for the single gate toggling. To explain the increased flow rate, a localized model and an exponential decay model for the zeta potential distribution was proposed. The localized model described the zeta potential changes at the gate region only and the inherent zeta potential outside the gate region is unmodified. The exponential decay model proposed that the zeta potential outside the gate region is defined by an exponential decay (constant α) from the zeta potential at the gate region. Comparison of the two models and the experimental results from multi-gate network revealed that the zeta potential is only locally modified. In contrast, both models predicted a velocity in the field-free microchannel for the large gate coverage case that was larger than that observed experimentally. For the multi-gate network, the re-

sults exhibited an experimental trend that was observed in the data for single microchannel with partial gate coverage. Lower EOF pumping may be present for larger gate coverage areas.

The dynamic zeta potential control in FEFC is an improvement over the static modification methods, such as surface coatings, in that the chemistry of the microchannel wall can be adjusted during the analysis. Additionally, in a microfluidic network with FEFC gates, pressure pumping can be generated with bi-directional control with a response time that was observed to be smaller than tens of milliseconds. This pumping method, with nanoliter-per-minute pumping rates, has the potential for fine resolution chemical mixing and non-mechanical pressure pumping. The reliability of the device is dependent on the dielectric strength of the material. Therefore operation at low gate voltages improves its reliability. Moreover, the FEFC polymer device demonstrated an inexpensive, durable, and compact LOC device. First, the use of polymer materials is a cost-reduction over silicon and glass microfabrication. Second, the pumping method is non-mechanical so that a robust implementation is possible. Lastly, the FEFC polymer devices enable the future development of miniaturized, automated chemical processes for compact LOC devices.

8.1 Significant Contributions

The work presented in this dissertation is novel in the pursuit of high-throughput LOC devices and microfluidic networks. The significant contributions of this work are:

- The development of a microfluidic multiplexer, which leveraged from the FEFC work in silicon.

- The first demonstration of FEFC in an all-polymer microfluidic device.
- An all-polymer FEFC device with 2D and 3D microfluidic networks and independent flow control components.
- A flow visualization technique with neutralized fluorescent microparticles to characterize the network devices.
- An analytical model that predicts the electroosmotic and induced pressure flow in matrix-form.
- Experimental investigation into various gate conditions, gate designs, and microchannel dimensions for future FEFC microfluidic networks.

8.2 Future Work

The Parylene C microchannel wall technology must be refined for consistent and repeatable device operation. A prime concern is the effect of gate coverage on the EOF control. Previous researchers in FEFC have hypothesized that extended zeta potential flow control is possible because of surface conductance, whose presence has been experimentally verified for fused silica capillaries [139, 68]. Characterization of the surface conductance (or lack of) for Parylene C and PDMS is needed. To improve the FEFC performance of Parylene C, the surface chemical groups that generate the electric double layer should be identified in order to better understand the mechanism of EOF and FEFC in the all-polymer microchannels. Additionally, surface treatment methods need to be investigated that will reduce the inherent zeta potential for improved flow control. If Parylene C is untreatable, then FEFC devices with Parylene A or AB should be explored, because the amine group on the polymer chain could be a target site

for tailoring the surface chemistry. With improved understanding of Parylene C, the performance of the FEFC microfluidic devices can be further improved

The micro-particle image velocimetry was adequate in characterizing the field-free flow, but spatial flow measurements of the combined EOF and pressure flow in the EOF microchannels are needed. Maintaining a plug-like flow profile is critical to reduce sample diffusion and so refined measurements of the induced pressure flow in the complete system are necessary. In this regard, computation simulations of the electrokinetic flow in the network can assist in further describing the induced pressure gradients and sample dispersion. Previous studies [123, 137] have highlighted the inherent problems with modeling EOF, and so this must be overcome to study FEFC. With computation simulations, the assumption of fully developed flow is not required. Also, the flow can be modeled with different zeta potentials along the walls of the microchannel. This may be present in the FEFC microchannels due to different surface charges, hence different surface groups, which may exist between the Parylene C and PDMS walls. If different inherent zeta potentials exist between the Parylene C and PDMS, then the flow may have different slip velocities at the walls, resulting in increased sample diffusion. Parylene C has been used to make a complete microchannel structure [43] and so eliminating PDMS from the all-polymer microchannel design may be necessary, but achievable. Combining spatial velocity measurements and numerical simulations will provide a better understanding of the FEFC phenomena.

Protein or DNA separations or control chemical mixing need to be demonstrated in the single FEFC microchannel and/or microfluidic network. The work of this dissertation has been towards the development of these systems and their characterization through flow measurements and modeling. However, applying

the technology in this dissertation to high performance capillary electrophoresis applications would benchmark the advantage of a disposable, microfluidic system with FEFC for high-throughput analysis and combinatorial chemistry.

Appendix A

Electric Double Layer

The works of Overbeek [139] and Hunter [50] form the basis for the discussion in this section. The thickness of the double layer and distribution of the counter-ions are described. Additionally, the derivation of the capacitance of the double layer is also provided for its relevancy to field-effect flow control.

A.1 Charge Distribution in the Liquid Phase

The distribution of the counter-ions in the liquid phase is discussed because it is critical to understanding the control over the zeta potential. The fundamental electrostatic relationship for the liquid phase of wall-fluid system is Poisson's equation:

$$\nabla^2 \psi = -\frac{\rho_e}{\epsilon} \tag{A.1}$$

where ρ_e is the spatial charge density and ϵ is the dielectric permittivity of the fluid medium. To determine the charge density of the liquid phase, the ion distribution is assumed to be at equilibrium with constant electrochemical potential so that the electrical and diffusive forces balance each other. Additionally, it is questionable to assume permittivity to be independent of position, because the electric fields generated at the fluid-solid interface are sufficiently high to modify

the solvent structure. The assumption of uniformity in permittivity is an ongoing debate among researchers [50], nevertheless it is satisfactory in the fully developed model presented here.

Emphasis is made that at equilibrium, the electrical and chemical diffusion forces balance. For clarification, the electrochemical potential, $\bar{\mu}_i$, is the work done in transferring a charge particle i from infinity into the interior of the phase. Although "chemical" effects are themselves electrical in nature, the electrochemical potential can be separated into its "chemical" part and its "electrical" part:

$$\bar{\mu}_i = \mu_i + z_i e\psi \tag{A.2}$$

where μ_i is the chemical potential of the phase, z_i is the valence of particle i, e is the elementary electric charge, and ψ is the electrical potential. The chemical potential or "intensity" of a chemical is the change in (molar) Gibbs free energy at constant temperature and pressure for a change in infinitesimal molar quantity:

$$\mu_i = (\partial G/\partial n_i)_{T,p}$$

Assuming that the ideal behavior of the solution is dependent on the concentration of i ions, n_i, the chemical potential can be expressed as

$$\mu_i = \mu_i^0 + kT \ln n_i \tag{A.3}$$

where μ_i^0 is the standard chemical potential, k is the Boltzmann constant, and T is the temperature.

In determining the spatial charge density, ρ_e, the liquid phase is assumed to be at equilibrium. Thus, the electrochemical potential of the ions must be constant everywhere ($\nabla\bar{\mu}_i = 0$) yielding a balance between diffusion and static electricity in equation A.2:

$$\nabla\mu_i = -z_i e\nabla\psi \tag{A.4}$$

Applying equation A.3 to express the relationship between ion concentration and electrical potential yields

$$\nabla \ln n_i = -\frac{z_i e}{kT} \nabla \psi \tag{A.5}$$

To find the ion concentration near the solid-liquid interface, let the potential ($\psi = 0$) be defined at a point far into the bulk fluid phase ($x \to \infty$). Then equation A.5 can be solved to yield the Boltzmann equation for the ion concentration:

$$n_i = n_i^0 \exp\left(-z_i e \psi / kT\right) \tag{A.6}$$

where n_i^0 is the concentration of ion i under standard conditions. This relation specifies the local concentration of each ion type in the region near the microchannel wall. It is important to point out that if ψ is positive, then positive ions are depleted from the double layer region ($n_+ < n_+^0$) and negative ions are attracted to the region ($n_- < n_-^0$).

Finally, the spatial charge density is given by the algebraic sum of the ionic charges per unit volume:

$$\rho_e = \sum_i n_i z_i e \tag{A.7}$$

Substituting the Boltzmann (equation A.6) and spatial charge density (equation A.7) into the Poisson equation (equation A.1) yields the classical Poisson-Boltzmann equation

$$\nabla^2 \psi = -\frac{1}{\epsilon} \sum_i n_i^0 z_i e \exp\left(-z_i e \psi / kT\right) \tag{A.8}$$

Equation A.8 can be further simplified by considering only a liquid composed of single binary electrolytes of valency z, such that $z = z_+ = -z_-$. This is a valid assumption because of the single valency of common buffer solutions such as Tris buffer solution. Additionally, in order to preserve electroneutrality of the

solution, the ion concentrations are equal throughout the fluid ($n^0 = n^0_+ = n^0_-$). Equation A.8 further simplifies to

$$\nabla^2\psi = -\frac{1}{\epsilon}\left(n^0_+ z_+ e \exp\left(-z_+ e\psi/kT\right) + n^0_- z_- e \exp\left(-z_- e\psi/kT\right)\right)$$

$$\nabla^2\psi = -\frac{1}{\epsilon}\left(n^0 ze \exp\left(-ze\psi/kT\right) - n^0 ze \exp\left(ze\psi/kT\right)\right)$$

$$\nabla^2\psi = \frac{2n^0 ze}{\epsilon}\sinh\left(ze\psi/kT\right) \tag{A.9}$$

with the application of the trigonometric identity $2\sinh p = \exp(p) - \exp(-p)$.

To find the charged distribution near the microchannel wall, equation A.9 can be integrated after multiplying both sides by $2d\psi/dx$ and applying the previous assumption for the potential at a far distance from the microchannel wall[1]:

$$2\frac{d\psi}{dx}\frac{d^2\psi}{dx^2} = \frac{4n^0 ze}{\epsilon}\sinh\left(ze\psi/kT\right)\frac{d\psi}{dx}$$

$$\int_{x=\infty}\frac{d}{dx}\left(\frac{d\psi}{dx}\right)^2 dx = \frac{4n^0 ze}{\epsilon}\int_{\psi=0}\sinh\left(ze\psi/kT\right)\, d\psi$$

$$\left(\frac{d\psi}{dx}\right)^2 = \frac{4n^0 kT}{\epsilon}\left(\cosh\left(ze\psi/kT\right) - 1\right)$$

$$\left(\frac{d\psi}{dx}\right)^2 = \frac{8n^0 kT}{\epsilon}\sinh^2\left(ze\psi/2kT\right)$$

$$\frac{d\psi}{dx} = \pm\left(\frac{8n^0 kT}{\epsilon}\right)^{\frac{1}{2}}\sinh\left(ze\psi/2kT\right) \tag{A.10}$$

Additionally, equation A.10 is elegantly expressed with the Debye-Hückle parameter, κ, for symmetric electrolyte[2], which strongly depends on the ion concentration:

$$\kappa^2 = \frac{e^2\sum_i n_i^0 z_i^2}{\epsilon kT}$$

[1] as $x \to \infty$, $\psi = 0$ and $d\psi/dx = 0$

[2] For simplicity, assume $z_+ = 1, z_- = -1$.

$$\kappa = \left(\frac{2e^2 n^0}{\epsilon kT}\right)^{\frac{1}{2}} \tag{A.11}$$

Substituting a non-dimensional potential parameter $\tilde{\psi} = e\psi/kT$ allows equation A.10 to be expressed in compact form with the Debye-Hückle parameter:

$$\frac{kT}{e}\frac{d\tilde{\psi}}{dx} = \pm\left(\frac{8n^0 kT}{\epsilon}\right)^{\frac{1}{2}} \sinh\left(z\tilde{\psi}/2\right)$$

$$\frac{d\tilde{\psi}}{dx} = \pm 2\kappa \sinh\left(\tilde{\psi}/2\right) \tag{A.12}$$

Equation A.12 can be integrated to find the ion distribution near the microchannel wall, which has non-dimensional electrostatic potential $\tilde{\psi}_0$:

$$\int_{\tilde{\psi}_0}^{\tilde{\psi}} \frac{d\tilde{\psi}}{\exp\left(\tilde{\psi}/2\right) - \exp\left(-\tilde{\psi}/2\right)} = \int_0^x \pm\kappa\, dx$$

yielding

$$\kappa x = \pm \log \frac{\left(\exp\left(\tilde{\psi}_0/2\right)+1\right)\left(\exp\left(\tilde{\psi}/2\right)-1\right)}{\left(\exp\left(\tilde{\psi}_0/2\right)-1\right)\left(\exp\left(\tilde{\psi}/2\right)+1\right)} \tag{A.13}$$

To visualize the potential near the microchannel wall, the relationship in equation A.13 is illustrated in Figure A.1. From the microchannel wall, the non-dimensional potential decays exponentially at a distance scaled by the measure of the ionic concentration. For all surface potentials, the potential decreases[3] by 1/e at a distance of $1/\kappa$. Moreover, the effect of the electric double layer diminishes to a value of 2% of the wall surface potential, ψ_0, at a distance of $3/\kappa$, showing that the electric double layer affects only a region of nanometers in thickness[4]. Therefore, it is customary to regard the inverse of the Debye-Hückle parameter, $1/\kappa$, as the thickness of the double layer.

[3] e = 2.71828...

[4] κ depends on the ionic concentration so for 1 mM solution at 25 °C, the double layer thickness is 9.62 nm.

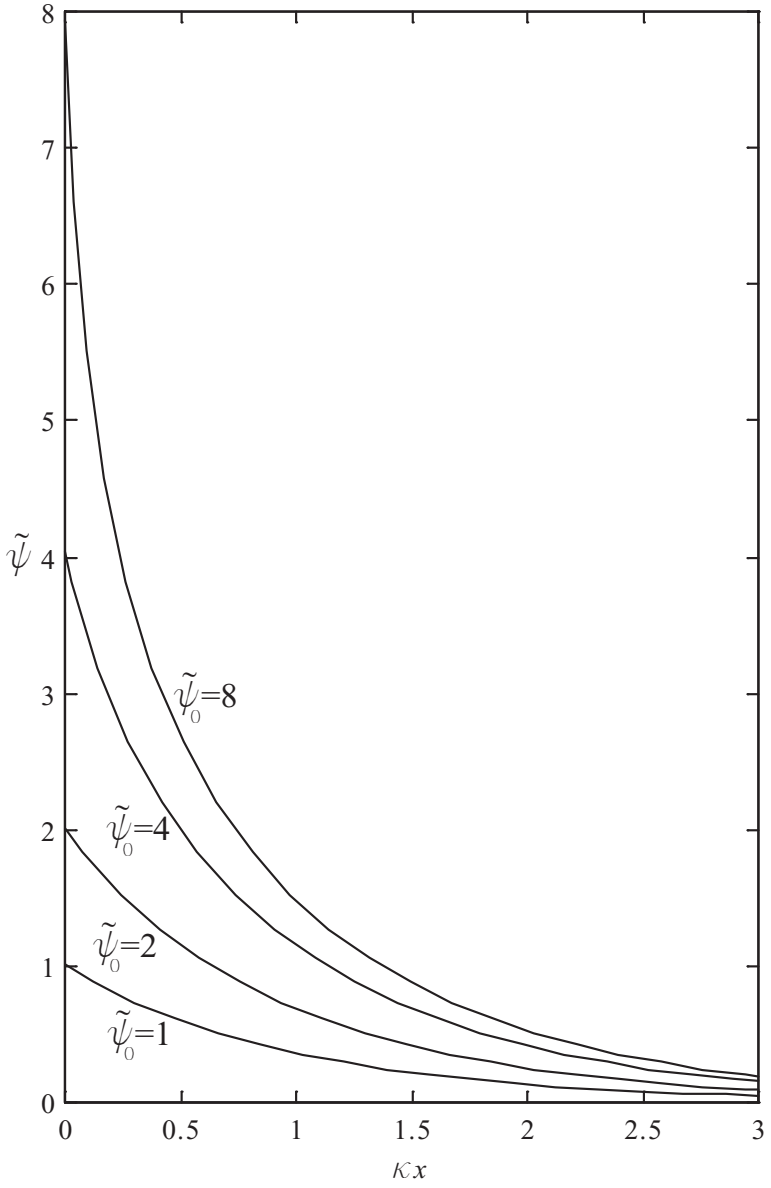

Figure A.1: Electrical potential in the double layer according to equation A.13 for values of wall surface charge $\tilde{\psi}_0 = 1$, 2, 4, and 8.

A.2 Debye-Hückle Approximation

The Poisson-Boltzman equation is often simplified for use in the fluid mechanics analysis of electroosmotic flow. An approximation for the hyperbolic sine function for small angles ($\sinh(x) \approx x$ for small x) is used in equation A.9:

$$\nabla^2\psi = \frac{2n^0 ze}{\epsilon}\left(ze\psi/kT\right) \tag{A.14}$$

This simplification is referred to as the Debye-Hückle approximation and implies that ψ is small everywhere in the double layer ($ze\psi \leq kT$). As a result, the approximation is only valid for

$$\psi \leq \frac{25.7\,\mathrm{mV}}{z}$$

Depending on the pH and the materials chosen for the microchannel wall, the values for ψ are not usually small to satisfy the Debye-Hückle approximation. For example, the zeta potential for fused silica glass is -29 mV [62] and -30 mV for PDMS [35]. At lower pH values, these values decrease to -2.6 mV for fused silica at pH 3 [69] and -4.4 mV for PDMS at pH 3 [35].

The Debye-Hückle parameter, κ (equation A.11), can be substituted into the Debye-Hückle approximation (equation A.14) to yield

$$\nabla^2\psi = \kappa^2\psi \tag{A.15}$$

Equation A.15 is elliptic and can be solved by specifying the boundary conditions. For ψ varying only with x, equation A.15 is multiplied by $2(d\psi/dx)$ and integrated in the same manner as equation A.10:

$$2\frac{d\psi}{dx}\frac{d^2\psi}{dx^2} = 2\kappa^2\psi\frac{d\psi}{dx}$$

$$\int_{x=\infty}\frac{d}{dx}\left(\frac{d\psi}{dx}\right)^2 dx = 2\kappa^2\int_{\psi=o}\psi\,d\psi$$

$$\frac{d\psi}{dx} = -\kappa\psi \tag{A.16}$$

Integrating equation A.16 and applying the boundary condition at the microchannel wall ($\psi = \psi_0$) yields

$$\psi = \psi_0 \exp(-\kappa x) \tag{A.17}$$

which simplifies the description of the potential distribution near the microchannel wall to exponential decay.

A.3 Capacitance of the Double Layer

With the ion distribution in the electric double layer well described, the next area of focus is the derivation of the capacitance of the double layer. This value is of importance in Section 2.3 in order to understand the change in the zeta potential under the transverse electric field. The charge per unit area on the microchannel wall, σ_0, must balance that in the liquid phase

$$\sigma_0 = -\int_0^\infty \rho_e \, dx \tag{A.18}$$

Substituting for ρ_e from Poisson's equation (equation A.1) yields

$$\sigma_0 = \epsilon \int_0^\infty \frac{d^2\psi}{dx^2} \, dx$$

$$\sigma_0 = -\epsilon \left(\frac{d\psi}{dx}\right)_{x=0}$$

For symmetric electrolytes, equation A.10 gives:

$$\sigma_0 = \epsilon \left(\frac{8n^0 kT}{\epsilon}\right)^{\frac{1}{2}} \sinh\left(z_i e\psi_0/kT\right)$$

$$\sigma_0 = \frac{2\epsilon kT}{e}\kappa \sinh\left(z_i e\psi_0/kT\right) \tag{A.19}$$

To obtain the capacitance of the diffuse layer, recall that the differential capacitance at constant temperature, pressure, and chemical potential is given by

$$C = (\partial Q/\partial \Psi)_{T,p,\mu_i,\ldots} \tag{A.20}$$

where Q is the electrical charge and Ψ is the potential with respect to a reference electrode. In the case of the electrical double layer, equation A.20 is

$$C_d = (d\sigma_0/d\psi_0)$$

With equation A.19, the capacitance of the diffuse layer is:

$$C_d = \epsilon z \kappa \cosh\left(\frac{ze\psi_0}{2kT}\right)$$

$$C_d = 2.285 z c^{1/2} \cosh\left(19.4 z \psi_0\right) \tag{A.21}$$

The units for the diffuse layer capacitance is $\mathrm{F/m^2}$ for $\mathrm{c^{1/2}}$ in mol $\mathrm{L^{-1}}$ and ψ_0 in volts. The double layer capacitance resembles the capacitance for parallel plates[5] where $\epsilon z \cosh\left(ze\psi_0/2kT\right)$ is the permittivity of the liquid phase and $1/\kappa$ is the thickness of the double layer. However, unlike a parallel plate capacitor, the double layer has only one plate of charge, at the wall surface, and a distributed charge in the liquid phase.

[5]Capacitance per unit area is $C = \epsilon/d$ where d is the distance between parallel plates

BIBLIOGRAPHY

[1] A. Manz, N. Graber, and H. M. Widmer, "Miniaturized Total Chemical Analysis Sysems: a Novel Concept for Chemical Sensing," *Sensors and Actuactors B*, vol. B1, no. 1-6, pp. 244–248, 1990.

[2] D. J. Harrison, A. Manz, Z. Fan, H. Ludi, and H. M. Widmer, "Capillary Electrophoresis and Sample Injection Systems Integrated on a Planar Glass Chip," *Analytical Chemistry*, vol. 64, no. 17, pp. 1926–1932, 1992.

[3] S. C. Jacobson, R. Hergenroder, L. B. Koutny, and J. M. Ramsey, "High-Speed Separations on a Microchip," *Analytical Chemistry*, vol. 68, no. 7, pp. 1114–1118, 1994.

[4] C. S. Effenhauser, C. J. M. Bruin, A. Paulus, and M. Ehrat, "Integrated Capillary Electrophoresis on Flexible Silicone Microdevices: Anaylsis of DNA Restriction Fragments and Detection of Single DNA Molecules on Microchips," *Analytical Chemistry*, vol. 69, no. 17, pp. 3451–3457, 1997.

[5] A. Weston and P. R. Brown, *HPLC and CE : fundamentals and applications.* San Diego, CA: Academic Press, 1997.

[6] J. Khandurina, T. E. McKnight, S. C. Jacobson, L. C. Waters, R. S. Foote, and J. M. Ramsey, "Integrated System of Rapid PCR-Based DNA Analysis

in Microfluidic Devices," *Analytical Chemistry*, vol. 72, no. 13, pp. 2995–3000, 2000.

[7] H. Liu, C. Felten, Q. Xue, B. Zhang, P. Jedrzejewski, B. L. Karger, and F. Foret, "Development of Multichannel Devices with an Array of Electrospray Tips for High-Throughput Mass Spectrometry," *Analytical Chemistry*, vol. 72, no. 14, pp. 3303–3310, 2000.

[8] T. Thorsen, S. Maerkl, and S. R. Quake, "Microfluidic Large-Scale Integration," *Science*, vol. 298, pp. 580–584, 2002.

[9] M. A. Burns, "Everyone's a (future) Chemist," *Science*, vol. 296, pp. 1818–1819, 2002.

[10] D. R. Reyes, D. Iossifidis, P.-A. Auroux, and A. Manz, "Micro Total Analysis Systems. 1. Introduction, Theory, and Techology," *Analytical Chemistry*, vol. 74, no. 12, pp. 2623–2636, 2002.

[11] S. Hayamizu, K. Higashino, Y. Fujii, Y. Sando, and K. Yamamoto, "Development of a Bi-Directional Valve-less Silicon Micro-pump Controlled by Driving Waveform," *Sensors and Actuactors A*, vol. 103, pp. 83–87, 2003.

[12] A. Terray, J. Oakley, and D. W. M. Marr, "Microfluidic Control Using Colloidal Devices," *Science*, vol. 296, pp. 1841–1844, 2002.

[13] J. M. Berg, R. Anderson, M. Anaya, B. Lahlouh, M. Holtz, and T. Dallas, "A Two-Stage Discrete Peristaltic Micropump," *Sensors and Actuactors A*, vol. 104, pp. 6–10, 2003.

[14] C.-H. Chen and J. G. Santiago, "A planar electroosmotic micropump," *Journal of Microelectromechanical Systems*, vol. 11, no. 6, pp. 672–683, 2002.

[15] J. Zhong, M. Yi, and H. H. Bau, "Magneto hydrodynamic (MHD) pump fabricated with ceramic tapes," *Sensors and Actuactors A*, vol. 96, pp. 59–66, 2002.

[16] Y. Song and T. Zhao, "Modelling and test of a thermally-driven phase-change nonmechanical micropump," *Journal of Micromechanics and Microengineering*, vol. 11, pp. 713–719, 2001.

[17] V. Namasivayam, R. G. Larson, and D. T. Burke, "Transpiration-based micropump for delivering continuous ultra-low flow rates," *Journal of Micromechanics and Microengineering*, vol. 13, pp. 261–271, 2003.

[18] D. S. Kim, K.-C. Lee, T. H. Kwon, and S. S. Lee, "Micro-channel Filling Flow Considering Surface Tension Effect," *Journal of Micromechanics and Microengineering*, vol. 12, pp. 236–246, 2002.

[19] D. C. Duffy, H. L. Gillis, J. Lin, J. Norman F. Sheppard, and G. J. Kellog, "Microfabricated Centrifugal Microfluidic Systems: Characterization and Multiple Enzymatic Assays," *Analytical Chemistry*, vol. 71, no. 20, pp. 4669–4678, 1999.

[20] D. J. Harrison, A. Manz, and P. G. Glavina, "Electroosmotic Pumping within a Chemical Sensor System Integrated on Silicon," in *Proc. Int. Conf. on Solid-State Sensors and Actuators (Transducers '91)*, vol. 1. New York, NY: IEEE, 1991, pp. 792–795.

[21] R. S. Ramsey and J. M. Ramsey, "Generating Electrospray from Microchip Devices Using Electroosmotic Pumping," *Analytical Chemistry*, vol. 69, no. 6, pp. 1174–1178, 1997.

[22] C. T. Culbertson, R. S. Ramsey, and J. M. Ramsey, "Electroosmotically Induced Hydraulic Pumping on Microchips: Differential Ion Transport," *Analytical Chemistry*, vol. 72, no. 10, pp. 2285–2291, 2000.

[23] S. L. R. Barker, D. Ross, M. J. Tarlov, M. Gaitan, and L. E. Locascio, "Control of Flow Direction in Microfluidic Devices with Polyelectrolyte Multilayers," *Analytical Chemistry*, vol. 72, no. 24, pp. 5925–5929, 2000.

[24] R. B. M. Schasfoort, S. Schlautmann, J. Hendrikse, and A. van den Berg, "Field-Effect Flow Control for Microfabricated Fluidic Networks," *Science*, vol. 286, pp. 942–945, 1999.

[25] N. Polson and M. A. Hayes, "Electroosmotic Flow Control of Fluids on a Capillary Electrophoresis Microdevice Using an Applied External Voltage," *Analytical Chemistry*, vol. 72, no. 5, pp. 1088–1092, 2000.

[26] P. K. Yuen, L. J. Kricka, and P. Wilding, "Semi-disposable microvalves for use with microfabricated devices or microchips," *Journal of Micromechanics and Microengineering*, vol. 10, pp. 401–409, 2000.

[27] A. V. Pattekar and M. V. Kothare, "Novel microfluidic interconnectors for high temperature and pressure applications," *Journal of Micromechanics and Microengineering*, vol. 13, pp. 337–345, 2003.

[28] H. Becker and L. E. Locascio, "Polymer microfluidic devices," *Talanta*, vol. 56, pp. 267–287, 2002.

[29] M. A. Roberts, J. S. Rossier, P. Bercier, and H. Girault, "UV Laser Machined Polymer Substrates for the Development of Microdiagnostic Systems," *Analytical Chemistry*, vol. 69, no. 11, pp. 2035–2042, 1997.

[30] L. Klintberg, M. Svedberg, F. Nikolajeff, and G. Thornell, "Fabrication of a Paraffin Actuator Using Hot Embossing of Polycarbonate," *Sensors and Actuactors A*, vol. 103, pp. 307–316, 2003.

[31] L. Yingjie, D. Ganser, A. Schneider, R. Liu, J. Blackwell, D. Fayden, D. Weston, D. Rhine, T. Smekal, and P. Grodzinski, "Polycarbonate-based capillary electrophoresis devices for DNA analysis," in *Proc. Int. Conf. on Solid-State Sensors and Actuactors (Transducers '01)*, E. Obermeier, Ed., vol. 2. Munich, Germany: IEEE, 2001, pp. 1170–1173.

[32] D. C. Duffy, J. C. McDonald, O. J. A. Schueller, and G. M. Whitesides, "Rapid Prototyping of Microfluidic System in Poly(dimethylsiloxane)," *Analytical Chemistry*, vol. 70, no. 23, pp. 4974–4984, 1998.

[33] J. R. Anderson, D. T. Chiu, R. J. Jackman, O. Cherniavskaya, J. C. McDonald, H. Wu, S. H. Whitesides, and G. M. Whitesides, "Fabrication of Topologically Complex Three-Dimensional Microfluidic Systems in PDMS by Rapid Prototyping," *Analytical Chemistry*, vol. 72, no. 14, pp. 3158–3164, 2000.

[34] B.-H. Jo, L. M. Van Lergerhe, K. M. Motsegood, and D. J. Beebe, "Three-Dimensional Micro-Channel Fabrication in Polydimethylsiloxanw (PDMS) Elastomer," *Journal of Microelectromechanical Systems*, vol. 9, no. 1, pp. 76–81, 2000.

[35] G. Ocvirk, M. Munroe, R. Oleschuk, K. Westra, and D. J. Harrison, "Electrokinetic control of fluid flow in native poly(dimethylsiloxane) capillary electrophoresis device," *Electrophoresis*, vol. 21, pp. 107–115, 2000.

[36] J. S. Rossier, M. A. Roberts, R. Ferrigno, and H. H. Girault, "Electrochemical Detection in Polymer Microchannels," *Analytical Chemistry*, vol. 71, no. 19, pp. 4294–4299, 1999.

[37] L. Martynova, L. E. Locascio, M. Gaitan, G. W. Kramer, R. G. Christensen, and W. A. MacCrehan, "Fabrication of Plastic Microfluid Channels by Imprinting Methods," *Analytical Chemistry*, vol. 69, no. 23, pp. 4783–4789, 1997.

[38] R. Truckenmuller, Z. Rummler, T. Schaller, and W. K. Schomburg, "Low-cost thermoforming of micro fluidic analysis chips," *Journal of Micromechanics and Microengineering*, vol. 12, pp. 375–379, 2002.

[39] L. J. Guerin, M. Bossel, M. Demierre, S. Calmes, and P. Renaud, "Simple and Low Cost Fabrication of Embedded Micro-Channnels by using a New Thick-Film Photoplastic," in *Proc. Int. Conf. on Solid-State Sensors and Actuactors (Transducers '97)*. Chicago, IL: IEEE, 1997, pp. 1419–1422.

[40] P. Selvaganapathy, Y.-s. L. Ki, P. Renaud, and C. H. Mastrangelo, "Bubble-Free Electrokinetic Pumping," *Journal of Microelectromechanical Systems*, vol. 11, no. 5, pp. 448–453, 2002.

[41] L. Licklider, X.-Q. Wang, A. Desai, T. Yu-Chong, and T. D. Lee, "A Micromachined Chip-Based Electrospray Source for Mass Spectrometry," *Analytical Chemistry*, vol. 72, no. 2, pp. 367–375, 2000.

[42] X.-Q. Wang and Y.-C. Tai, "A normally closed in-channel micro check valve," in *Proc. IEEE Int. Conf. on Micro Electro Mechanical Systems*. Miyazaki, Japan: IEEE, 2000, pp. 68–73.

[43] J. R. Webster, M. A. Burns, D. T. Burke, and C. H. Mastrangelo, "Monolithic Capillary Electrophoresis Device with Integrated Fluorescence Detector," *Analytical Chemistry*, vol. 73, no. 7, pp. 1622–1626, 2001.

[44] R. J. Beynon and J. S. Easterby, *Buffer Solutions : The Basics*. New York: IRL Press, 1996.

[45] P.-A. Auroux, D. Iossifidis, D. R. Reyes, and A. Manz, "Micro Total Analysis Systems. 2. Analytical Standard Operations and Applications," *Analytical Chemistry*, vol. 74, no. 12, pp. 2637–2652, 2002.

[46] M. B. Kerby, M. Spaid, S. Wu, J. W. Parce, and R.-L. Chien, "Selective Ion Extraction: a Separation Method for Microfluidic Devices," *Analytical Chemistry*, vol. 74, no. 20, pp. 5175–5183, 2002.

[47] C.-M. Ho and Y.-C. Tai, "Micro-Electro-Mechanical Systems (MEMS) and Fluid Flows," *Annual Review of Fluid Mechanics*, vol. 30, pp. 579–612, 1998.

[48] Y. Liu, J. C. Fanguy, J. M. Bledsoe, and C. S. Henry, "Dynamic Coating Using Polyelectrolyte Multilayers for Chemical Control of Electroosmotic Flow in Capillary Electrophoresis Microchips," *Analytical Chemistry*, vol. 72, no. 25, pp. 5939–5944, 2000.

[49] S.-C. Wang, C. E. Perso, and M. D. Morris, "Effects of Alkaline Hydrolysis and Dynamic Coatings on the Electroosmotic Flow in Polymeric Micro-

fabricated Channels," *Analytical Chemistry*, vol. 72, no. 7, pp. 1704–1706, 2000.

[50] R. J. Hunter, *Zeta Potential in Colloid Science : Principles and Applications*. New York: Academic Press, 1981.

[51] M. von Smoluchowski, *Handbuch der Electrizitat und des Magnetismus*. Leipzig: Barth, 1921, vol. II.

[52] M. A. Hayes, I. Kheterpal, and A. G. Ewing, "Effects of Buffer pH on Electroosmotic Flow Control by an Applied Radial Voltage for Capillary Zone Electrophoresis," *Analytical Chemistry*, vol. 65, no. 1, pp. 27–31, 1993.

[53] R. M. McCormick, "Capillary Zone Electrophoresis Separation of Peptide and Proteins Using Low pH Buffers in Modified Silica Capillaries," *Analytical Chemistry*, vol. 60, no. 21, pp. 2322–2328, 1988.

[54] R.-L. Chien and J. C. Helmer, "Electroosmotic Properties and Peak Broadening in Field-Amplified Capillary Electrophoresis," *Analytical Chemistry*, vol. 63, no. 14, pp. 1354–1361, 1991.

[55] W. J. Lambert and D. L. Middleton, "pH Hysteresis Effect with Silica Capillaries in Capillary Zone Electrophoresis," *Analytical Chemistry*, vol. 62, no. 15, pp. 1585–1587, 1990.

[56] C. Schwer and E. Kenndler, "Electrophoresis in Fused-Silica Capillaries: The Influence of Organic Solvents on the Electroosmotic Velocity and Zeta Potential," *Analytical Chemistry*, vol. 63, no. 17, pp. 1801–1807, 1991.

[57] J. W. Jorgenson and K. D. Lukas, "Capillary Zone Electrophoresis," *Science*, vol. 222, pp. 266–272, 1983.

[58] S. Hjerten, "High-performance Electrophoresis : Elimination of Electroendosmosis and Solute Adsorption," *Journal of Chromatography A*, vol. 347, pp. 191–198, 1985.

[59] F. M. White, *Viscous Fluid Flow*. New York: McGraw-Hill, 1991.

[60] G. K. Batchelor, *An Introduction to Fluid Dynamics*. New York: Cambridge University Press, 1967.

[61] C. L. Rice and R. Whitehead, "Electrokinetic Flow in a Narrow Cylinderical Capillary," *Journal of Physical Chemistry*, vol. 69, no. 11, pp. 4017–4024, 1965.

[62] C. S. Lee, W. C. Blanchard, and C.-T. Wu, "Direct Control of the Electroosmosis in Capillary Zone Electrophoresis by Using an External Electric Field," *Analytical Chemistry*, vol. 62, no. 14, pp. 1550–1552, 1990.

[63] K. Ghowsi and R. J. Gale, "Field Effect Electroosmosis," *Journal of Chromatography*, vol. 559, pp. 95–101, 1991.

[64] C. S. Lee, D. McManigill, C.-T. Wu, and B. Patel, "Factors Affecting Direct Control of Electroosmosis Using an External Electric Field in Capillary Electrophoresis," *Analytical Chemistry*, vol. 63, no. 15, pp. 1519–1523, 1991.

[65] C. S. Lee, C.-T. Wu, T. Lopes, and B. Patel, "Analysis of Separation Efficiency in Capillary Electrophoresis with Direct Control of Electroosmosis by Using an External Electric Field," *Journal of Chromatography A*, vol. 559, pp. 133–140, 1991.

[66] M. A. Hayes and A. G. Ewing, "Electroosmotic Flow Control and Monitoring with an Applied Radial Voltage for Capillary Zone Electrophoresis," *Analytical Chemistry*, vol. 64, no. 5, pp. 512–516, 1992.

[67] S. Wu, T. Lopes, B. Patel, and C. S. Lee, "Effect of Direct Control of Electroosmosis on peptide and protein separations in capillary electrophoresis," *Analytical Chemistry*, vol. 64, no. 8, pp. 886–891, 1992.

[68] M. A. Hayes, I. Kheterpal, and A. G. Ewing, "Electroosmotic Flow Control and Surface Conductance in Capillary Zone Electrophoresis," *Analytical Chemistry*, vol. 65, no. 15, pp. 2010–2013, 1993.

[69] T.-L. Huang, P. Tsai, C.-T. Wu, and C. S. Lee, "Mechanistic Studies of Electroosmotic Control at the Capillary-Solution Interface," *Analytical Chemistry*, vol. 65, no. 20, pp. 2887–2893, 1993.

[70] C. A. Keely, R. R. Holloway, and T. A. van de Goor, "Dispersion in Capillary Electrophoresis with External Flow Control Methods," *Journal of Chromatography A*, vol. 652, pp. 283–289, 1993.

[71] M. A. Hayes, "Extension of External Voltage Control of Electroosmosis to High-pH Buffers," *Analytical Chemistry*, vol. 71, no. 17, pp. 3793–3798, 1999.

[72] N. K. Hartley and M. A. Hayes, "Examination of Theoretical Models in External Voltage Control of Capillary Electrophoresis," *Analytical Chemistry*, vol. 74, no. 6, pp. 1249–1255, 2002.

[73] R. B. M. Schasfoort, J. Hendrikse, and A. van den Berg, "μTransparent Insulating Channels as Components for Miniaturized Chemical Separation

Devices," in *Microprocesses and Nanotechnology Conference, 2000 International*. Tokyo, Japan: IEEE, 2000, pp. 20–24.

[74] Y.-S. Leung Ki, R. B. M. Schasfoort, S. Sclautmann, P. Renaud, and A. van den Berg, "Modeling of FlowFET Characteristics," in *Modeling and Simulation of Microsystems (MSM) 2000,*. San Diego, CA: Applied Computational Research Society, 2000, pp. 544–547.

[75] J. S. Buch, P.-C. Wang, D. L. DeVoe, and C. S. Lee, "Field-Effect Flow Control in a Polydimethylsiloxane-based Microfluidic System," *Electrophoresis*, vol. 22, no. 18, pp. 3902–3907, 2001.

[76] H. Poppe, A. Cifuentes, and W. T. Kok, "Theoretical Description of the Influence of External Radial Fields on the Electroosmotic Flow in Capillary electrophoresis," *Analytical Chemistry*, vol. 65, no. 5, pp. 888–893, 1996.

[77] X. Huang, M. Gordon, and R. N. Zare, "Current-Monitoring Method for Measuring the Electroosmotic Flow in Capillary Zone Electrophoresis," *Analytical Chemistry*, vol. 60, pp. 1837–1838, 1988.

[78] A. E. Herr, J. I. Molho, J. G. Santiago, M. G. Mungal, T. W. Kenny, and M. G. Garguilo, "Electroosmotic Capillary Flow with Nonuniform Zeta Potential," *Analytical Chemistry*, vol. 72, no. 5, pp. 1053–1057, 2000.

[79] N. J. Sniadecki, P.-C. Wang, C. S. Lee, and D. L. DeVoe, "A Silicon Microfluidic Multiplexer Using Field Effect Flow Control," in *Micro Total Analysis Systems 2001*, J. M. Ramsey and A. van den Berg, Eds. Monterey, California: Kluwer, 2001, pp. 187–188.

[80] G. Parker, *Introductory Semiconductor Device Physics*. New York: Prentice Hall, 1994.

[81] S. R. Morrison, M. J. Madou, and K. W. Frese, "Imperfections in and ion diffusion through oxide layers on silicon," *Applications of Surface Science*, vol. 6, pp. 138–148, 1980.

[82] K. F. Schrum, I. Joseph M. Lancaster, S. E. Johnston, and S. D. Gilman, "Monitoring Electroomostic Flow by Periodic Photobleaching of a Dilute, Neutral Fluorophore," *Analytical Chemistry*, vol. 72, no. 18, pp. 4317–4321, 2000.

[83] P. Horowitz and W. Hill, *The Art of Electronics*. New York, NY: Cambridge University Press, 1980.

[84] J. R. Reitz and F. J. Milford, *Foundations of Electromagnetic Theory*, 2nd ed. Palo Alto: Addison-Wesley, 1962.

[85] J.-M. Bureau, F. Bernard, and D. Broussoux, "High Performance Polymers for Packaging and Interconnections in Microelectronics," *Revue Technique Thomson - CSF*, vol. 20-21, no. 4, pp. 689–724, 1989.

[86] M. Howe-Grant, Ed., *Encyclopedia of Chemical Technology, Fourth Edition : Supplement Volume : Aerogels to Xylylene Polymers*. New York: Wiley, 1998.

[87] "Cyclotene 4000 Series Product Information."

[88] "Pyralin PI2800, PI5800, PI2540 Series Polyimides."

[89] "Molecular-PTFE Specification."

[90] "Information about Dow Corning brand Silicon Encapsulants."

[91] "Teflon AF Product Information."

[92] V. Srinivasan, V. K. Pamula, M. G. Pollack, and R. B. Fair, "Clinical Diagnostic on Human Whole Blood, Plasma, Serum, Urine, Saliva, Sweat, and Tears on a Digital Microfluidic Platform," in *Micro Total Analysis Systems*, vol. 2, Squaw Valley, CA, 2003, pp. 1287–1290.

[93] N. Dokmeci and K. Najafi, "A High-Sensitivity Polyimide Capacitive Relative Humidity Sensor for Monitoring Anodically Bonded Hermetic Micropackages," *Journal of Microelectromechanical Systems*, vol. 10, no. 2, pp. 197–204, 2001.

[94] P. A. Stupar and A. A. Pisano, "Silicon, Parylene, and Silicon/Parylene Micro-Needles for Strength and Toughness," in *Transducers '01.* Munich, Germany: IEEE, 2001.

[95] W. Sim, D. Kim, K. Kim, K. Kwon, B. Kim, B. Choi, S. Yang, and J. Park, "Fabrication, Test, and Simulation of a Parylene Diaphragm," in *Transducers '01.* Munich, Germany: IEEE, 2001.

[96] J. Lahann, D. Klee, W. Pluester, and H. Hoecker, "Bioactive immobilization of r-hirudin on CVD-coated metallic implant devices," *Biomaterials*, vol. 22, no. 8, pp. 817–826, 2000.

[97] J. Lahann, H. Hocker, and R. Langer, "Synthesis of Amino-[2.2]paracyclophanes - Beneficial Monomers for Bioactive Coating of Medical Implant Materials," *Angewandte Chemie International Edition*, vol. 40, no. 4, pp. 726–728, 2001.

[98] J. Lahann, M. Balcells, H. Lu, T. Rodon, K. F. Jensen, and R. Langer, "Functionalized Parylene Coatings for Microfluidic Applications," in *Micro Total Analysis Systems (Micro-TAS) 2002*, Nara, Japan, 2002, pp. 443–445.

[99] ——, "Reactive Polymer Coatings: A First Step toward Surface Engineering of Microfluidic Devices," *Analytical Chemistry*, vol. 75, no. 9, pp. 2117–2123, 2003.

[100] C. Kimball and D. L. DeVoe, "Integrated Thin Film Temperature Sensors for Polycarbonate Microfluidics," in *Micro Total Analysis Systems 2002*, Nara, Japan, 2002, pp. 724–726.

[101] A. D. Stroock, M. Weck, D. T. Chiu, W. T. S. Huck, P. J. A. Kenis, R. Ismagilov, and G. M. Whitesides, "Patterning electro-osmotic flow with patterned surface charge," *Physical Review Letters*, vol. 85, no. 15, pp. 3314–3317, 2000.

[102] S. Qian and H. H. Bau, "A Chaotic Electroosmotic Stirrer," *Analytical Chemistry*, vol. 74, no. 15, pp. 3616–3625, 2002.

[103] S. Hong, L. G. Frechette, and V. Modi, "Numerica simulation of mixing in a micro-channel with non-uniform zeta potential surface," in *Micro Total Analysis Systems 2002*, Nara, Japan, 2002, pp. 94–97.

[104] D. Erickson and D. Li, "Microchannel Flow with Patchwise and Periodic Surface Heterogeneity," *Langmuir*, vol. 18, no. 23, pp. 8949–8959, 2002.

[105] P. H. Paul, M. G. Garguilo, and D. J. Rakestraw, "Imaging of Pressure- and Electrokinetically Driven Flows through Open Capillaries," *Analytical Chemistry*, vol. 70, no. 13, pp. 2459–2467, 1998.

[106] D. Sinton, D. Erickson, and D. Li, "Photo-injection based sample design and electroosmotic transport in microchannels." *Journal of Micromechanics and Microengineering*, vol. 12, pp. 898–904, 2002.

[107] D. Ross and L. E. Locascio, "Effect of Caged Fluorescent Dye on the Electroosmotic Mobility in Microchannels," *Analytical Chemistry*, vol. 75, no. 5, pp. 1218–2020, 2003.

[108] J. L. Pittman, C. S. Henry, and S. D. Gilman, "Experimental Studies of Electroosmotic Flow Dynamics in Microfabricated Devices during Current Monitoring Experiments," *Analytical Chemistry*, vol. 75, no. 3, pp. 361–370, 2003.

[109] W. Schutzner and E. Kenndler, "Electrophoresis in Synthetic Organic Polymer Capillaries: Variation of Electroosmotic Velocity and Zeta Potential with pH and Solvent Composition," *Analytical Chemistry*, vol. 64, pp. 1991–1995, 1992.

[110] R. Sjoback, J. Nygren, and M. Kubista, "Absorption and Fluorescence Properties of Fluorescein," *Spectrochimica Acta A*, vol. 51, no. 6, pp. 7–21, 1995.

[111] H. J. Crabtree, M. U. Kopp, and A. Manz, "Shah Convolution Fourier Transform Detection," *Analytical Chemistry*, vol. 71, no. 11, pp. 2130–2138, 1999.

[112] Y. C. Kwok, N. T. Jeffery, and A. Manz, "Velocity Measurement of Particles Flowing in a Microfluidic Chip Using Shah Convolution Fourier Transform Detection," *Analytical Chemistry*, vol. 73, no. 8, pp. 1748–1753, 2001.

[113] J. A. McReynolds, P. Edirisinghe, and S. A. Shippy, "Shah and Sine Convolution Fourier Transform Detection for Microchannel Electrophoresis with a Charge Coupled Device," *Analytical Chemistry*, vol. 74, no. 19, pp. 5063–5070, 2002.

[114] C. D. Meinhart, S. T. Wereley, and J. G. Santiago, "PIV measurements in a microchannel flow," *Experiments in Fluids*, vol. 27, pp. 414–419, 1999.

[115] J. G. Santiago, S. T. Wereley, C. D. Meinhart, J. D. Beebe, and R. J. Adrian, "A particle image velocimetry system for microfluidics," *Experiments in Fluids*, vol. 25, pp. 316–319, 1998.

[116] S. Devasenathipathy, J. G. Santiago, and K. Takehara, "Particle Tracking Techniques for Electrokinetic Microchannel Flows," *Analytical Chemistry*, vol. 74, no. 15, pp. 3704–3713, 2002.

[117] H. Kinoshita, M. Oshima, J. W. Hong, T. Fujii, T. Saga, and T. Kobayashi, "Micro PIV Measurement of Electroosmotic Flow," in *Micro Total Analysis Systems (Micro-TAS) 2002*, Nara, Japan, 2002, pp. 374–376.

[118] H. Klank, G. Goranovic, J. P. Kutter, H. Gjelstrup, J. Michelsen, and C. H. Westergaard, "PIV Measurements in a Microfluidic 3D-sheathing Structure with Three-Dimensional Flow Behaviour," *Journal of Micromechanics and Microengineering*, vol. 12, pp. 862–869, 2002.

[119] Y. Sato, K. Hishida, and M. Maeda, "Quantitative Measurments and Control of Electrokinetically Driven Flow in Microspace," in *Micro Total Analysis Systems (Micro-TAS) 2002*, Nara, Japan, 2003, pp. 512–514.

[120] V. Hohreiter, S. T. Wereley, M. G. Olsen, and J. N. Chung, "Cross-correlation Analysis for Temperature Measurement," *Measuremetn Science and Technology*, vol. 13, pp. 1072–1078, 2002.

[121] N. J. Sniadecki, C. S. Lee, M. Beamesderfer, and D. L. DeVoe, "Field Effect Flow Control in a Polymer Microchannel Network," in *Proc. IEEE conference on Solid-State Sensors and Actuators (Transducers '03)*. Boston, MA: IEEE, 2003, pp. 682–685.

[122] N. J. Sniadecki, C. S. Lee, P. Sivanesan, and D. L. DeVoe, "Induced Pressure Pumping in Polymer T-Channels via Field-Effect Flow Control," *Analytical Chemistry (submitted)*, 2003.

[123] F. Bianchi, R. Ferrigno, and H. H. Girault, "Finite Element Simulation of an Electroosmotic-Driven Flow Division at a T-Junction of Microscale Dimensions," *Analytical Chemistry*, vol. 72, no. 9, pp. 1987–1993, 2000.

[124] R. Qiao and N. R. Aluru, "A compact model for electroosmotic flows in microfluidic devices," *Journal of Micromechanics and Microengineering*, vol. 12, pp. 625–635, 2002.

[125] N. J. Sniadecki, R. Chang, C. S. Lee, M. Beamesderfer, and D. L. DeVoe, "Field Effect Flow Control in a Polymer T-Intersection Microfluidic Network," in *Micro Total Analysis Systems (Micro-TAS '03)*, Squaw Valley, CA, 2003, pp. 899–902.

[126] M. Wilm and M. Mann, "Electrospray and Taylor-Cone theory, Dole's beam of macromolecules at last?" *International Journal of Mass Spectrometry and Ion Processes*, vol. 136, pp. 167–180, 1994.

[127] ——, "Analytical Properties of the Nanoelectrospray Ion Source," *Analytical Chemistry*, vol. 68, no. 1, pp. 1–8, 1996.

[128] G. Neubauer and M. Mann, "Mapping of Phosphorylation Site of Gel-Isolated Proteins by Nanoelectrospray Tandem Mass Spectrometry: Potentials and Limitations," *Analytical Chemistry*, vol. 71, no. 1, pp. 235–242, 1999.

[129] T. Köcher, G. Allmaier, and M. Wilm, "Nanoelectrospray-based detection and sequencing of substoichiometric amounts of phosphopeptides in complex mixtures," *Journal of Mass Spectrometry*, vol. 38, pp. 131–137, 2003.

[130] P. Sivanesan, N. J. Sniadecki, C. S. Lee, and D. L. DeVoe, "Field-Effect Flow Control in 3-D Polymer Microfluidics," *To be published*, 2004.

[131] M. J. Mitchell, R. Qiao, and N. R. Aluru, "Meshless Analysis of Steady-State Electro-Osmotic Transport," *Journal of Microelectromechanical Systems*, vol. 9, no. 4, pp. 435–449, 2000.

[132] J. G. Santiago, "Electroosmotic Flows in Microchannels with Finite Inertial and Pressure Forces," *Analytical Chemistry*, vol. 73, no. 10, pp. 2353–2365, 2001.

[133] A. Ajdari, "Generation of transverse fluid currents and forces by an electric field: Electro-osmosis on charge-modulated and undulated surfaces," *Physical Review E*, vol. 53, no. 5, pp. 4996–5005, 1996.

[134] D. Long, H. A. Stone, and A. Ajdari, "Electroosmotic Flows Created by Surface Defects in Capillary Electrophoresis," *Journal of Colloid and Interface Science*, vol. 212, pp. 338–349, 1999.

[135] E. B. Cummings, S. K. Griffiths, R. H. Nilson, and P. H. Paul, "Conditions of Similitude between the Fluid Velocity and Electric Field in Electroosmotic Flow," *Analytical Chemistry*, vol. 72, no. 11, pp. 2526–2532, 2000.

[136] V. P. Andreev, S. G. Dubrovsky, and Y. V. Stepanov, "Mathematical Modeling of Capillary Electrophoresis in Rectangular Channels," *Journal of Microcolumn Separations*, vol. 9, pp. 443–450, 1997.

[137] F. Bianchi, F. Wagner, P. Hoffman, and H. Girault, "Electroosmotic Flow in Composite Microchannels and Implications in Microcapillary Electrophoresis Systems," *Analytical Chemistry*, vol. 73, no. 4, pp. 829–836, 2001.

[138] R. K. Shah and A. L. London, *Laminar Flow Forced Convection in Ducts*. New York: Academic, 1978.

[139] J. T. G. Overbeek, *Electrokinetic Phenomena*, ser. Colloid Science. New York: Elsevier, 1952, vol. 1.